

Graz University of Technology
Institute for Strength of Materials
Kopernikusgasse 24/I
8010 Graz



Patrick Wurm

On the Use of Stochastic Approximation
for Coupling the FEM and MD in
Quasi-static Isothermal Problems

Master's Thesis

to achieve the university degree of
Diplom-Ingenieur

submitted to
Graz University of Technology

Supervisor:
Dipl.-Ing. Dr.techn. Manfred Ulz

Graz, September 2015

Abstract

English Version

The aim of this thesis is to provide an improved information exchange in a two-scale model. On the macroscale of this model, the equations of continuum mechanics of solids are solved using a non-linear FE-formulation. The microscale, on which a canonical ensemble of statistical mechanics is simulated using molecular dynamics, is replacing a classic material formulation. However, the molecular dynamics simulation produces noise-corrupted output as due to reasons of computational efficiency no thermodynamic equilibrium is reached. This noise prevents the model from a classical convergence behavior and creates a setting that reminds heavily of iteration schemes in stochastic approximation. Different strategies to improve convergence behavior known from stochastic approximation will therefore be applied. Their use on numerical examples shall prove and compare their effectiveness.

Deutsche Version

Ziel dieser Arbeit ist die Verbesserung des Informationsaustausches in einem Zweiskalenmodell. Auf der Makroskala dieses Modells werden die Gleichungen der Festkörper-Kontinuumsmechanik mittels einer nichtlinearen FE-Formulierung gelöst. Die Mikroskala, auf der ein kanonisches Ensemble der statistischen Mechanik mittels Molekulardynamik simuliert wird, ersetzt hierbei eine klassische Materialformulierung. Die Molekulardynamik-Simulation liefert allerdings störungsbehaftete Größen, da aus Gründen der Recheneffizienz kein thermodynamisches Gleichgewicht erreicht wird. Diese Störungen verhindern ein klassisches Konvergenzverhalten und erzeugen eine Konfiguration die starke Ähnlichkeit zu Iterationsschemen der stochastischen Approximation aufweist. Daher werden verschiedene, aus der stochastischen Approximation bekannte, Methoden zur Konvergenzverbesserung auf ihre Eignung untersucht. Numerische Beispiele sollen ihre Wirksamkeit zeigen und miteinander vergleichen.

Affidavit

English Version

I declare that I have authored this thesis independently, that I have not used other than the declared sources/resources, and that I have explicitly indicated all material which has been quoted either literally or by content from the sources used. The text document uploaded to TUGRAZonline is identical to the present master's thesis.

Deutsche Version

Ich erkläre an Eides statt, dass ich die vorliegende Arbeit selbstständig verfasst, andere als die angegebenen Quellen/Hilfsmittel nicht benutzt, und die den benutzten Quellen wörtlich und inhaltlich entnommenen Stellen als solche kenntlich gemacht habe. Das in TUGRAZonline hochgeladene Textdokument ist mit der vorliegenden Masterarbeit identisch.

Datum / Date

Unterschrift / Signature

Preface

This thesis was written in the spring and summer of 2015 at the Institute for Strength of Materials, TU Graz, as a part of the master's programme 'Mechanical Engineering'. The computational results presented have been achieved for the most part using the Vienna Scientific Cluster (VSC3).

Acknowledgements

I would like to express my sincere gratitude to my supervisor Dr. Manfred Hannes Ulz for his continuous support and encouragement. I could not imagine a better mentor than him.

I also want to thank Prof. Christian Celigoj for providing me access to the necessary facilities and for the pleasant working atmosphere.

Last but not least I want to thank my family: my parents Melitta and Franz, my grandmother Emma and my brother Sebastian, for supporting me throughout my whole school and university career and my wonderful girlfriend Lisa for her understanding nature and for being always there for me.

Contents

Abstract	3
1 Introduction	8
2 Continuum Mechanics	9
2.1 Deformation Gradient Tensor	10
2.2 Strain Measures	11
2.2.1 Finite strain theory	11
2.2.2 Infinitesimal strain theory	12
2.3 Stress Measures	13
2.3.1 Cauchy stress tensor	13
2.4 Principle of Virtual Work	14
2.5 Transition to the Non-linear Finite Element Method	17
3 Finite Element Method	23
3.1 Isoparametric Concept	23
3.1.1 One-dimensional Lagrange elements	25
3.1.2 Two-dimensional Lagrange elements	26
3.1.3 Computation of derivatives	27
3.1.4 Integration over the reference volume	28
3.2 Linear/Non-linear Finite Element Analysis	29
3.2.1 Linear finite element formulation	29
3.2.2 Non-linear finite element formulation	32
3.2.3 Newton-Raphson method	33
4 Molecular Dynamics (MD)	35
4.1 Hamiltonian	35
4.2 Interatomic Potential	37
4.2.1 Periodic boundary conditions (PBC)	38
4.3 Equations of Motion (EOM)	39
4.4 Numerical Integrator: Gear's Predictor Corrector Algorithm	40
4.5 Extraction of Macroscopic Observables	42
5 Two-scale Model	45

CONTENTS

6	Stochastic Approximation	48
6.1	Averaging of the Iterates	49
6.2	Averaging of the Observatives	50
7	Application of SA to FEM/MD	51
7.1	Offline Averaging	52
7.2	Online Averaging	54
7.3	Online/Offline Averaging	54
8	Numerical Examples	56
8.1	Plate with circular Notch under uniaxial Tension	57
8.1.1	Comparison of the averaging behavior	58
8.1.2	Comparison of the stress distributions	61
8.2	Elastic infinite Half-Plane under Line Load	66
8.2.1	Comparison of the averaging behavior	68
8.2.2	Comparison of the stress distributions	70
	Conclusion	72
	Appendices	
A	EAM functions	77
B	Calculation of forces	79
C	Comparison of the convergence behavior towards zero	82

Chapter 1

Introduction

In the following chapters, a brief basis will be presented in a relevant extent to cover the problem characteristics. For further insight please consult the resources given at the beginning of each chapter.

Chapter 2 will cover the basics of continuum mechanics, which will prove beneficial in the remainder of this work. Basic strain and stress measures will be introduced in section 2.2 and 2.3, the principle of virtual work is discussed in section 2.4 and the transition to the finite element method is established in section 2.5. In chapter 3, a linear and non-linear finite element formulation will be deduced, in which isoparametric elements are used. Some of these elements will be shown exemplarily. Molecular dynamics will be discussed briefly in the subsequent chapter 4. Different statistical ensembles will be covered using a single Hamiltonian, and it will be shown how to extract macroscopic observables from the MD simulation. In the following chapter 5, the connection between the finite element method, which models the macroscale, and molecular dynamics, the method on the microscale, will be explained. The resulting equations for the two-scale model exhibit strong similarities to stochastic approximation (SA) methods. This allows us to adopt well-known strategies from SA, that show potential to improve convergence behavior. These relationships are described in chapter 7. A brief introduction to stochastic approximation will be given in chapter 6. In the final chapter 8, the advantages in using stochastic approximation methods will be revealed in the light of two numerical examples.

Chapter 2

Continuum Mechanics

The basis for the following sections 2.1 to 2.4 were the books of *Bonet and Wood (1997)* and *Bathe (1996)*, whereas most of the information of section 2.5 is referred to *Daxner and Rammerstorfer (2011)*.

Continuum mechanics deals with the deformation of bodies, modeled as a continuous mass, under external loads. To study some basic relations, consider a deformable body as shown in figure 2.1.

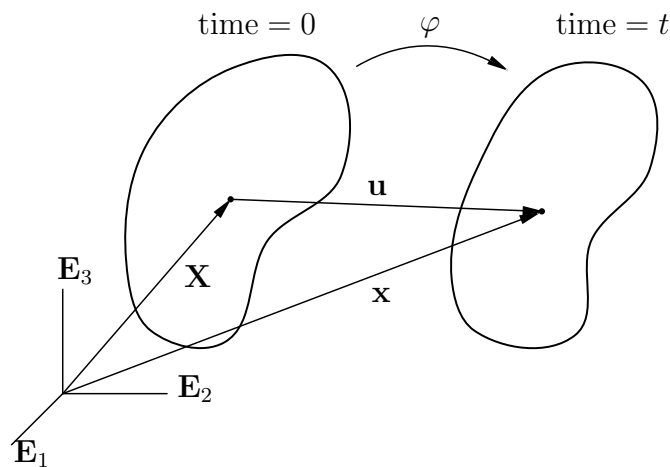


Figure 2.1: General deformable body in its referential (or material) and its current (or spatial) configuration. For simplicity, it is assumed that the the material and spatial configuration share a common Cartesian basis \mathbf{E}_i .

At time 0, the body is in its undeformed, referential or material configuration. The position of the continuum particles in this configuration is described by vectors \mathbf{X} . Due to external loading, the body will change its shape and position. If we consider an arbitrary time t during this deformation process, we can describe the continuum particles by vectors \mathbf{x} and call this the deformed, current or spatial configuration.¹

¹Generally, we will denote properties of the material configuration with capital letters, whereas properties of the spatial configuration are written in lower-case letters.

This allows us to write the displacement as

$$\mathbf{u} = \mathbf{x} - \mathbf{X}. \quad (2.1)$$

The motion of the body is described by a mapping

$$\mathbf{x} = \varphi(\mathbf{X}, \mathbf{t}). \quad (2.2)$$

While this mapping gives the spatial positions for given material points and time, the inverse mapping, as a counterpart, can be written as

$$\mathbf{X} = \varphi^{-1}(\mathbf{x}, \mathbf{t}). \quad (2.3)$$

2.1 Deformation Gradient Tensor

The deformation gradient tensor \mathbf{F} is a fundamental measure used to describe the local deformation at body points in continuum mechanics and is defined as

$$\mathbf{F} = \frac{\partial \mathbf{x}}{\partial \mathbf{X}}. \quad (2.4)$$

The deformation gradient tensor allows to calculate the corresponding spatial vector to an infinitesimal vector $d\mathbf{X}$ in the material configuration as

$$d\mathbf{x} = \mathbf{F}d\mathbf{X}. \quad (2.5)$$

Using the relation $\mathbf{x} = \mathbf{X} + \mathbf{u}$ for the spatial coordinates allows us to further write

$$\mathbf{F} = \frac{\partial \mathbf{x}}{\partial \mathbf{X}} = \frac{\partial(\mathbf{X} + \mathbf{u})}{\partial \mathbf{X}} = \frac{\partial \mathbf{X}}{\partial \mathbf{X}} + \frac{\partial \mathbf{u}}{\partial \mathbf{X}} = \mathbf{1} + \mathbf{G} \quad (2.6)$$

in terms of the displacement gradient

$$\mathbf{G} = \frac{\partial \mathbf{u}}{\partial \mathbf{X}} = \frac{\partial u_i}{\partial X_j}. \quad (2.7)$$

The deformation gradient also allows a mapping of volume and area elements between the two configurations. A small volume element in the spatial configuration with edges parallel to the Cartesian basis axes can be written as

$$dv = \det[d\mathbf{x}_1, d\mathbf{x}_2, d\mathbf{x}_3], \quad (2.8)$$

where $d\mathbf{x}_i = x_i \mathbf{E}_i$, $i = 1, 2, 3$ denote the three edge vectors. Using equation 2.5 and the properties of the determinant, this can be written as

$$dv = \det[\mathbf{F} d\mathbf{X}_1, \mathbf{F} d\mathbf{X}_2, \mathbf{F} d\mathbf{X}_3] \quad (2.9)$$

$$= \det \mathbf{F} \det[d\mathbf{X}_1, d\mathbf{X}_2, d\mathbf{X}_3] \quad (2.10)$$

$$= \det \mathbf{F} dV \quad (2.11)$$

²This thesis assumes a Cartesian basis and, therefore, does not distinguish between a covariant and contravariant basis. For further information the reader is referred to [Marsden and Hughes \(1983\)](#) and [Sokolnikoff \(1964\)](#).

or

$$dv = JdV \quad (2.12)$$

in terms of the Jacobian $J = \det \mathbf{F}$. The mapping of an area element can be expressed as

$$\mathbf{n} da = J\mathbf{F}^{-T}\mathbf{N} dA, \quad (2.13)$$

what is known as Nanson's formula. For a detailed derivation see [Bonet and Wood \(1997\)](#).

The deformation gradient \mathbf{F} is not suitable as a measure of strain, as it got some severe drawbacks regarding invariance in rigid body rotation and translation, independence of direction and is also not symmetric in general. In the next section, suitable strain measures will be presented, which do not lack these important properties.

2.2 Strain Measures

2.2.1 Finite strain theory

In finite strain theory, strains are assumed to be arbitrarily large, which means that the spatial configuration is allowed to differ significantly from the material configuration. Out of the variety of available strain measures, only two important ones will be mentioned here, namely the Green-Lagrange and the Euler-Almansi strain tensor.

If, for example, half the change in the inner product of two elemental vectors $d\mathbf{X}_1$ and $d\mathbf{X}_2$ is chosen to describe the deformation and equation 2.5 is used, we get

$$\frac{1}{2}(d\mathbf{x}_1 \cdot d\mathbf{x}_2 - d\mathbf{X}_1 \cdot d\mathbf{X}_2) = \frac{1}{2}(d\mathbf{x}_1^T d\mathbf{x}_2 - d\mathbf{X}_1^T d\mathbf{X}_2) \quad (2.14)$$

$$= \frac{1}{2}(d\mathbf{X}_1^T \mathbf{F}^T \mathbf{F} d\mathbf{X}_2 - d\mathbf{X}_1^T d\mathbf{X}_2) \quad (2.15)$$

$$= d\mathbf{X}_1^T \mathbf{E} d\mathbf{X}_2 \quad (2.16)$$

with \mathbf{E} being the Green-Lagrange strain tensor

$$\mathbf{E} = \frac{1}{2}(\mathbf{C} - \mathbf{1}) \quad (2.17)$$

which relates the change in the inner product to the material vectors $d\mathbf{X}_1$ and $d\mathbf{X}_2$. In the equation above, \mathbf{C} is the right Cauchy-Green deformation tensor

$$\mathbf{C} = \mathbf{F}^T \mathbf{F}. \quad (2.18)$$

Alternatively, the change in the inner product can also be written in terms of spatial vectors $d\mathbf{x}_1$ and $d\mathbf{x}_2$

$$\frac{1}{2}(d\mathbf{x}_1^T d\mathbf{x}_2 - d\mathbf{X}_1^T d\mathbf{X}_2) = d\mathbf{X}_1^T \mathbf{e} d\mathbf{X}_2, \quad (2.19)$$

where \mathbf{e} is the Euler-Almansi strain tensor

$$\mathbf{e} = \frac{1}{2}(\mathbf{1} - \mathbf{b}^{-1}). \quad (2.20)$$

In this relation, \mathbf{b} is the left Cauchy-Green deformation tensor

$$\mathbf{b} = \mathbf{F}\mathbf{F}^T. \quad (2.21)$$

2.2.2 Infinitesimal strain theory

Unlike finite strain theory where strains are allowed to be large, infinitesimal strain theory deals with strains and deformations that are much smaller than the characteristic dimensions of the body.

The components of the Green-Lagrange strain tensor can be written as

$$E_{ij} = \frac{1}{2} \left[\frac{\partial u_i}{\partial X_j} + \frac{\partial u_j}{\partial X_i} + \frac{\partial u_k}{\partial X_i} \frac{\partial u_k}{\partial X_j} \right]. \quad (2.22)$$

The assumption of infinitesimal strains allows us to linearize this expression, so that non-linear terms are neglected

$$E_{ij} = \frac{1}{2} \left[\frac{\partial u_i}{\partial X_j} + \frac{\partial u_j}{\partial X_i} \right]. \quad (2.23)$$

Applying this procedure analogous on the Green-Almansi strain tensor leads to

$$e_{ij} = \frac{1}{2} \left[\frac{\partial u_i}{\partial x_j} + \frac{\partial u_j}{\partial x_i} \right]. \quad (2.24)$$

Because the difference between material and spatial configuration is assumed to be infinitesimally small, these configurations approximately coincide and those two linearized strain tensors are approximately equal

$$E_{ij} \approx e_{ij} \approx \varepsilon_{ij} \quad (2.25)$$

and can therefore be replaced by the small strain tensor $\boldsymbol{\varepsilon}$ with its well-known components for normal strains

$$\varepsilon_{xx} = \frac{\partial u}{\partial X} \quad \varepsilon_{yy} = \frac{\partial v}{\partial Y} \quad \varepsilon_{zz} = \frac{\partial w}{\partial Z} \quad (2.26)$$

and

$$\varepsilon_{xy} = \frac{1}{2} \left(\frac{\partial u}{\partial Y} + \frac{\partial v}{\partial X} \right) \quad \varepsilon_{yz} = \frac{1}{2} \left(\frac{\partial v}{\partial Z} + \frac{\partial w}{\partial Y} \right) \quad \varepsilon_{zx} = \frac{1}{2} \left(\frac{\partial w}{\partial X} + \frac{\partial u}{\partial Z} \right) \quad (2.27)$$

for shear strains. In equations 2.26 and 2.27 the displacements u, v and w are in the x, y - and z -direction, respectively.

2.3 Stress Measures

In this section, stress will be introduced as force elements per unit elements in order to assess the effects of deformation. While in infinitesimal strain theory, forces are always related to the areas in the material configuration, forces in finite strain theory can be either per area in the material or per area in the spatial configuration.

2.3.1 Cauchy stress tensor

Consider a general deformable body in its current position. If the body is sliced in two, and we take a closer look at an area Δa with the normal vector \mathbf{n} on one of the two parts, we can see that the other part exerts the resulting force $\Delta \mathbf{p}$ onto this area element as shown in figure 2.2.

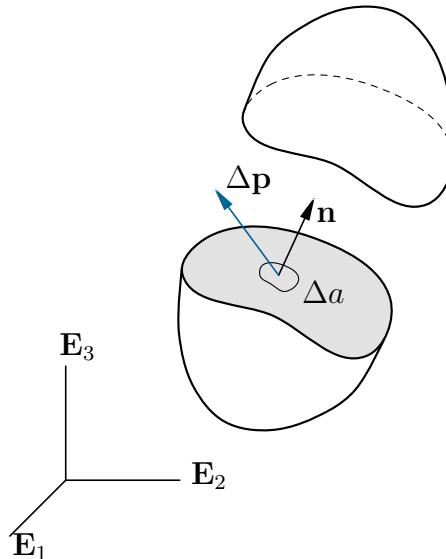


Figure 2.2: Resulting force $\Delta \mathbf{p}$ on an area element Δa .

The traction vector is then defined as

$$\mathbf{t}(\mathbf{n}) = \lim_{\Delta a \rightarrow 0} \frac{\Delta \mathbf{p}}{\Delta a}. \quad (2.28)$$

The normal vector \mathbf{n} is now related to the traction vector \mathbf{t} by a second order tensor, called the Cauchy stress tensor $\boldsymbol{\sigma}$,

$$\mathbf{t} = \boldsymbol{\sigma} \mathbf{n}. \quad (2.29)$$

The Cauchy stress tensor as a stress measure comes closest to the physical conception of stresses, therefore it is often denoted as true stress. The symmetrical property $\boldsymbol{\sigma} = \boldsymbol{\sigma}^T$ follows from the rotational equilibrium on the infinitesimal volume element. While the Cauchy stress tensor represents a purely spatial description,

as only forces and areas of the current configuration are involved, there are also other equivalent stress measures related to the material configuration, which will be discussed in the next section.

2.4 Principle of Virtual Work

In order to be able to apply the finite element method, a weak formulation of the characteristic differential equations is intended. One possibility to obtain such a formulation is the principle of virtual displacements.

If we limit ourselves to static problems, the equilibrium at the body in the deformed configuration is

$$\int_v (\sigma_{ij,j} + f_i^B) dv = 0, \quad (2.30)$$

where f_i^B are the volumetric body forces and $\sigma_{ij,j} = \text{div } \boldsymbol{\sigma}$ are the traction forces.

Consider a similar configuration as before, shown in figure 2.3, with a body in its initial configuration at time 0 and in its current deformed configuration at time t .

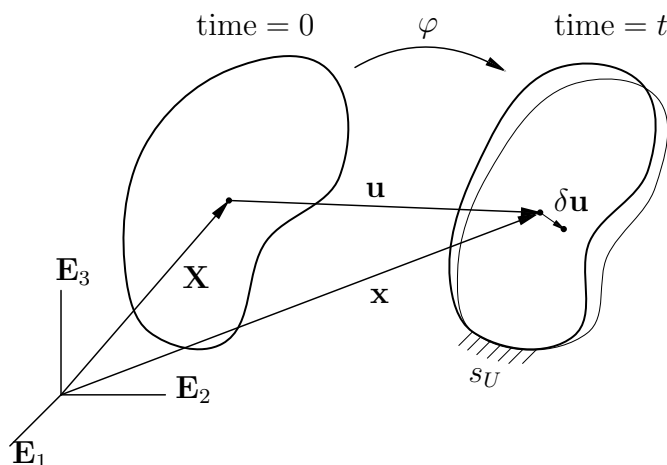


Figure 2.3: General deformable body in its material and spatial configuration with superposed arbitrary virtual displacements.

Introducing arbitrary virtual displacements δu_i , which are superposed to the existing deformation and fulfill the prescribed displacement boundary conditions $\delta u_i = 0$ on s_U ,³ leads to

$$\delta W = \int_v (\sigma_{ij,j} + f_i^B) \delta u_i dv = 0. \quad (2.31)$$

³The surface of the body $s = s_U \cup s_F$, where s_U is the part of the surface with prescribed displacement boundary conditions $u_i = \hat{u}_i$ and s_F is the part of the surface with natural force boundary conditions $\sigma_{ij}n_j = f_i^s$. Since virtual displacements are additional displacements, they must be zero at those parts of the surface, where displacements are prescribed.

2.4. PRINCIPLE OF VIRTUAL WORK

By using the relation $(\sigma_{ij}\delta u_i)_{,j} = \sigma_{ij,j}\delta u_i + \sigma_{ij}\delta u_{i,j}$ we can write this in an alternative form

$$\delta W = \int_v ((\sigma_{ij}\delta u_i)_{,j} - \sigma_{ij}\delta u_{i,j} + f_i^B \delta u_i) dv = 0. \quad (2.32)$$

Next, if the mathematical identity $\int_v (\sigma_{ij}\delta u_i)_{,j} dv = \int_s (\sigma_{ij}\delta u_i)n_j ds$ obtained from the divergence theorem is applied, we get

$$\delta W = \int_v (-\sigma_{ij}\delta u_{i,j} + f_i^B \delta u_i) dv + \int_{s_F} (\sigma_{ij}\delta u_i)n_j ds_F = 0, \quad (2.33)$$

or

$$\delta W = \underbrace{-\int_v \boldsymbol{\sigma} : \text{grad } \delta \mathbf{u} dv}_{\delta W_{int}} + \underbrace{\int_v \delta \mathbf{u} \cdot \mathbf{f}^B dv + \int_{s_F} \delta \mathbf{u} \cdot \mathbf{t}^S ds_F}_{\delta W_{ext}} = 0, \quad (2.34)$$

in symbolic notation, where \mathbf{t}^S are the surface loads and the virtual work is split into the internal and external virtual work. The pair $\boldsymbol{\sigma}$ and $\text{grad } \delta \mathbf{u}$ is said to be a work conjugate stress-strain pair with respect to the current volume, as it denotes the work per current volume. Equation 2.34 is also known as the spatial virtual work equation. The notation $\text{grad } \delta \mathbf{u}$ denotes the derivative of $\delta \mathbf{u}$ with respect to the spatial coordinates \mathbf{x} .

Remark 2.4.1. *Note that due to symmetry of $\boldsymbol{\sigma}$, $\text{grad } \delta \mathbf{u}$ can be replaced by its symmetrical part and we can write*

$$\begin{aligned} \boldsymbol{\sigma} : \text{grad } \delta \mathbf{u} &= \boldsymbol{\sigma} : \text{Sym}(\text{grad } \delta \mathbf{u}) \\ &= \boldsymbol{\sigma} : \frac{1}{2}(\text{grad } \delta \mathbf{u} + (\text{grad } \delta \mathbf{u})^T) \\ &= \boldsymbol{\sigma} : \delta \boldsymbol{\varepsilon}, \end{aligned}$$

where we have postulated small strains in the last equation, and $\delta \boldsymbol{\varepsilon}$ is the variation of the small strain tensor defined in section 2.2.2.

By using the chain rule, it can be easily shown that $\text{grad } \delta \mathbf{u} = \text{Grad } \delta \mathbf{u} \mathbf{F}^{-1}$, where $\text{Grad } \delta \mathbf{u}$ now stands for the derivative with respect to the material coordinates \mathbf{X} .

Since the displacements are $\mathbf{u} = \mathbf{x} - \mathbf{X}$, and therefore $\delta \mathbf{u} = \delta \mathbf{x}$, the internal virtual work can be further written as

$$\delta W_{int} = - \int_v \boldsymbol{\sigma} : \delta \mathbf{F} \mathbf{F}^{-1} dv. \quad (2.35)$$

By using the properties of the trace $\mathbf{A} : \mathbf{BC} = \text{tr}(\mathbf{A}(\mathbf{BC})^T) = \text{tr}(\mathbf{AC}^T \mathbf{B}^T) = \mathbf{AC}^T : \mathbf{B}$ and equation 2.12, this is further

$$\delta W_{int} = - \int_V J \boldsymbol{\sigma} \mathbf{F}^{-T} : \delta \mathbf{F} dV = - \int_V \mathbf{P} : \delta \mathbf{F} dV, \quad (2.36)$$

where \mathbf{P} , the first Piola-Kirchhoff stress tensor, is one of the possible stress measures mentioned in section 2.3.1. In contrast to the Cauchy stress tensor, the first Piola-Kirchhoff is unsymmetric and gives a mixed description since it relates the force in the spatial configuration to an oriented area vector in the material configuration. In \mathbf{P} and $\delta\mathbf{F}$ we can see another work conjugate pair, although this one is work conjugate with respect to the initial volume.

The internal work can further be written as

$$\begin{aligned}
 \delta W_{int} &= - \int_V \mathbf{P} : \delta\mathbf{F} \, dV \\
 &= - \int_V \text{tr}(\mathbf{P}\delta\mathbf{F}^T) \, dV \\
 &= - \int_V \text{tr}(\mathbf{P}\delta\mathbf{F}^T\mathbf{F}\mathbf{F}^{-1}) \, dV \\
 &= - \int_V \text{tr}(\delta\mathbf{F}^T\mathbf{F}\mathbf{F}^{-1}\mathbf{P}) \, dV \\
 &= - \int_V \text{tr}(\mathbf{P}^T\mathbf{F}^{-T}\delta\mathbf{F}^T\mathbf{F}) \, dV \\
 &= - \int_V \mathbf{F}^{-1}\mathbf{P} : \delta\mathbf{F}^T\mathbf{F} \, dV,
 \end{aligned} \tag{2.37}$$

where

$$\mathbf{S} = \mathbf{F}^{-1}\mathbf{P} = J\mathbf{F}^{-1}\boldsymbol{\sigma}\mathbf{F}^{-T} \tag{2.38}$$

is the second Piola-Kirchhoff stress tensor, which can be easily proven to be symmetric. Since \mathbf{S} relates forces in the undeformed configuration to areas in the same configuration, a purely material description is established. Due to the symmetrical property of \mathbf{S} , we can express $\delta\mathbf{F}^T\mathbf{F}$ in equation 2.37 by its symmetrical part. This gives

$$\delta W_{int} = - \int_V \mathbf{S} : \frac{1}{2}(\delta\mathbf{F}^T\mathbf{F} + \mathbf{F}^T\delta\mathbf{F}) \, dV \tag{2.39}$$

$$= - \int_V \mathbf{S} : \delta\mathbf{E} \, dV, \tag{2.40}$$

where \mathbf{S} and the variation of the Green-Lagrange strain tensor \mathbf{E} denote another work conjugate stress-strain pair. By considering equation 2.17 we find $\delta\mathbf{E} = 1/2\delta\mathbf{C}$. This definition can now be used to restate equation 2.34 as

$$\int_V \mathbf{S} : \delta\mathbf{E} \, dV = \delta W_{ext}. \tag{2.41}$$

This form of the virtual work equation can now be further rearranged in order to establish the link to a non-linear finite element formulation.

2.5 Transition to the Non-linear Finite Element Method

Let us now assume a configuration as shown in figure 2.4.

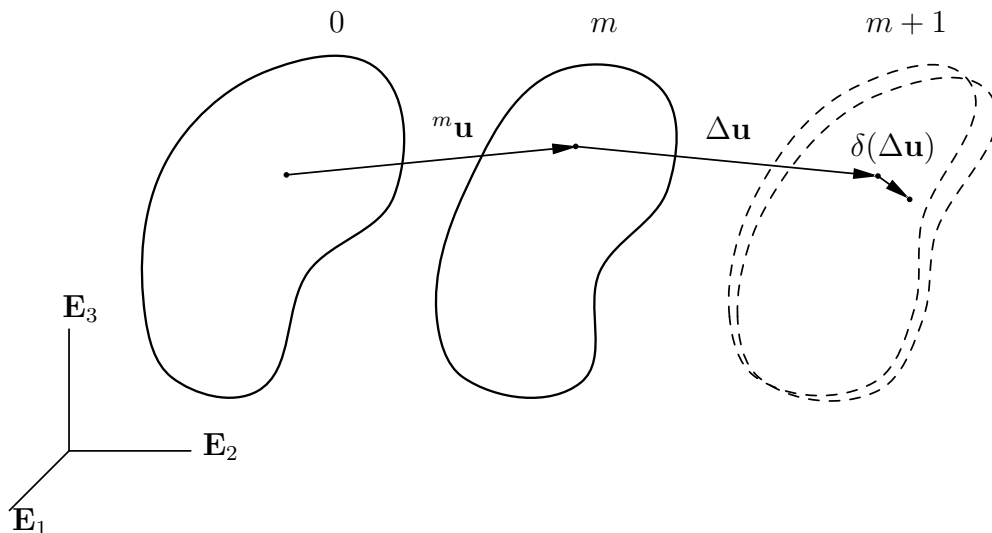


Figure 2.4: General deformable in its spatial configuration (0) and a known deformed configuration (m). The next configuration (m+1) is needed.

A general deformable body was originally located in position (0) and was then deformed to configuration (m), while it can be assumed that all quantities describing configuration (m) are well known and also that every state between the original configuration (0) and (m) is well known. Due to a change in load, the body will further deform to the unknown configuration (m+1). For (m+1), the virtual work equation is

$$\int_V {}^{m+1}\mathbf{S} : {}^{m+1}\delta\mathbf{E} dV = {}^{m+1}\delta W_{ext}. \quad (2.42)$$

In this equation, volume $V = {}^0V$ as well as the stresses and strains are related to the material configuration (0).⁴

The unknown configuration (m+1) can be expressed in terms of known quantities in configuration (m) and incremental values

$${}^{m+1}\mathbf{u} = {}^m\mathbf{u} + \Delta\mathbf{u} \quad {}^{m+1}\mathbf{E} = {}^m\mathbf{E} + \Delta\mathbf{E} \quad {}^{m+1}\mathbf{S} = {}^m\mathbf{S} + \Delta\mathbf{S}. \quad (2.43)$$

The Green-Lagrange strain tensor can be expressed in terms of the displacement gradient, defined in equation 2.7, as

$$\mathbf{E} = \frac{1}{2} (\mathbf{G} + \mathbf{G}^T + \mathbf{G}^T \mathbf{G}). \quad (2.44)$$

⁴Since all configurations between (0) and (m) are known, the description can be related to any of these. This means that different formulations are available. We relate all quantities to the material configuration (0) which is known as the total Lagrangian formulation.

The displacement gradient can now be expressed similarly to equation 2.43 as

$${}^{m+1}\mathbf{G} = {}^m\mathbf{G} + \Delta\mathbf{G}. \quad (2.45)$$

This gives the increment of the Green-Lagrange strain tensor

$$\begin{aligned} \Delta\mathbf{E} &= {}^{m+1}\mathbf{E} - {}^m\mathbf{E} \\ &= \frac{1}{2} \underbrace{(\Delta\mathbf{G} + \Delta\mathbf{G}^T + \Delta\mathbf{G}^T ({}^m\mathbf{G}) + ({}^m\mathbf{G})^T \Delta\mathbf{G})}_{\Delta\mathbf{E}^{lin}} + \frac{1}{2} \underbrace{\Delta\mathbf{G}^T \Delta\mathbf{G}}_{\Delta\mathbf{E}^{nl}} \end{aligned} \quad (2.46)$$

where $\Delta\mathbf{E}^{lin}$ is a linear function of the displacement gradient increments, whereas in $\Delta\mathbf{E}^{nl}$ quadratic terms of $\Delta\mathbf{G}$ occur.

The variation of the Green Lagrange strain tensor, which is part of equation 2.42, is further

$$\begin{aligned} {}^{m+1}\delta\mathbf{E} &= \delta({}^m\delta\mathbf{E} + \Delta\mathbf{E}) \\ &= \delta(\Delta\mathbf{E}) \\ &= \delta(\Delta\mathbf{E}^{lin} + \Delta\mathbf{E}^{nl}). \end{aligned} \quad (2.47)$$

The variation of these two terms shows that while the increment of the displacement gradient $\Delta\mathbf{G}$ only occurs as its variational form $\delta(\Delta\mathbf{G})$ in the linear part $\delta(\Delta\mathbf{E}^{lin})$, the non-linear part $\delta(\Delta\mathbf{E}^{nl})$ also involves $\Delta\mathbf{G}$ itself. As $\Delta\mathbf{G}$ consists of the derivatives of the sought displacement increments $\Delta\mathbf{u}$, while $\delta(\Delta\mathbf{G})$ consists of the derivatives of $\delta(\Delta\mathbf{u})$ (which can be chosen arbitrarily and can therefore be assumed as known quantities), the non-linear part \mathbf{E}^{nl} is unknown, while the linear part \mathbf{E}^{lin} is known.

Besides $\Delta\mathbf{E}$, the increment of the second Piola-Kirchhoff stress tensor $\Delta\mathbf{S}$ is also needed and can be approximated by linearization of a Taylor series expansion

$$\begin{aligned} \Delta\mathbf{S} &\approx \frac{\partial {}^m\mathbf{S}}{\partial {}^m\mathbf{E}} \Delta\mathbf{E} + \dots \\ \Delta\mathbf{S} &\approx {}^m\mathbb{C} \Delta\mathbf{E} = {}^m\mathbb{C} (\Delta\mathbf{E}^{lin} + \Delta\mathbf{E}^{nl}), \end{aligned} \quad (2.48)$$

where ${}^m\mathbb{C}$ denotes the stress-strain tensor (or elasticity tensor) in configuration (m).

Remark 2.5.1. *In the finite element method, the stresses ${}^m\mathbf{S}$ and the elasticity tensor ${}^m\mathbb{C}$ may be obtained from the material description. For example, for an hyperelastic material, those quantities can be gained through derivation of an elastic potential Ψ_e with respect to proper deformation measures. Elastic potentials Ψ_e are built using experimental data.*

In this work, a molecular dynamics simulation will take the place of the material description. The MD simulation gets a measure of deformation as its input and returns the material's response. Therefore we will not cover any 'classical' material descriptions in this work. For discussion see e.g. Bathe (1996).

Using the results of equation 2.43, 2.47 and 2.48 in equation 2.42 gives

$$\int_V [{}^m\mathbf{S} + {}^m\mathbb{C}(\Delta\mathbf{E}^{lin} + \Delta\mathbf{E}^{nl})] : \delta [\Delta\mathbf{E}^{lin} + \Delta\mathbf{E}^{nl}] dV = {}^{m+1}\delta W_{ext}. \quad (2.49)$$

This equation is now rearranged, so that known terms are found on the right-hand side, while unknown terms appear on the left-hand side⁵

$$\begin{aligned} \int_V [{}^m\mathbb{C}(\Delta\mathbf{E}^{lin} + \Delta\mathbf{E}^{nl})] : \delta [\Delta\mathbf{E}^{lin} + \Delta\mathbf{E}^{nl}] dV + \int_V {}^m\mathbf{S} : \delta\Delta\mathbf{E}^{nl} dV \\ = {}^{m+1}\delta W_{ext} - \int_V {}^m\mathbf{S} : \delta\Delta\mathbf{E}^{lin}. \end{aligned} \quad (2.50)$$

The first term on the left-hand is now linearized in the following way, so that the whole set of equations is only linearly dependent on the displacement increments $\Delta\mathbf{u}$

$$\int_V [{}^m\mathbb{C}\Delta\mathbf{E}^{lin}] : \delta [\Delta\mathbf{E}^{lin}] dV + \int_V {}^m\mathbf{S} : \delta\Delta\mathbf{E}^{nl} dV = {}^{m+1}\delta W_{ext} - \int_V {}^m\mathbf{S} : \delta\Delta\mathbf{E}^{lin} dV. \quad (2.51)$$

As all tensors in the equation above are symmetrical, it is convenient to use Voigt notation, in which the 6 independent values of the tensors \mathbf{E} and \mathbf{S} are arranged in the following way

$$\begin{aligned} \underline{\underline{\mathbf{E}}} &= \begin{bmatrix} E_{11} & E_{22} & E_{33} & 2E_{23} & 2E_{13} & 2E_{12} \end{bmatrix}^T \\ \underline{\underline{\mathbf{S}}} &= \begin{bmatrix} S_{11} & S_{22} & S_{33} & S_{23} & S_{13} & S_{12} \end{bmatrix}^T. \end{aligned} \quad (2.52)$$

The 21 independent values of the stress-strain tensor \mathbb{C} are arranged in a $[6 \times 6]$ matrix $\underline{\underline{\mathbb{C}}}$. This notation, together with the property of the tensor contraction $\mathbf{A} : \mathbf{B} = \mathbf{B} : \mathbf{A}$ allows to rewrite equation 2.51. The first term on the left-hand side is therefore

$$\int_V [{}^m\mathbb{C}\Delta\mathbf{E}^{lin}] : \delta [\Delta\mathbf{E}^{lin}] dV = \int_V \delta [\Delta\underline{\underline{\mathbf{E}}}^{lin}] \cdot [{}^m\underline{\underline{\mathbb{C}}}\Delta\underline{\underline{\mathbf{E}}}^{lin}] dV, \quad (2.53)$$

where the vector notation allowed to replace the tensor contraction with the scalar product (\cdot) . This notation also allows to express the increments of the Euler-Lagrange strain tensor as

$$\Delta\underline{\underline{\mathbf{E}}}^{lin} = \underline{\underline{\mathbf{D}}}_L \Delta\underline{\underline{\mathbf{u}}} \quad \delta[\Delta\underline{\underline{\mathbf{E}}}^{lin}] = \underline{\underline{\mathbf{D}}}_L \delta[\Delta\underline{\underline{\mathbf{u}}}], \quad (2.54)$$

⁵It must be noted that in case of deformation dependent loads, the variation of the external work δW_{ext} is not only dependent on the variation of the displacement $\delta\mathbf{u}$ but also on the displacement \mathbf{u} itself. Therefore, deformation dependent loads result in additional terms on the left-hand side of equation 2.50.

where $\Delta \underline{\mathbf{u}}$ is a $[3 \times 1]$ vector and $\underline{\mathbf{D}}_{\approx L}$ is the linear $[6 \times 3]$ differential operator matrix

$$\underline{\mathbf{D}}_{\approx L} = \begin{bmatrix} \partial_1 + {}^m u_{1,1} \partial_1 & & {}^m u_{2,1} \partial_1 & & {}^m u_{3,1} \partial_1 \\ & {}^m u_{1,2} \partial_2 & & \partial_2 + {}^m u_{2,2} \partial_2 & & {}^m u_{3,2} \partial_2 \\ & & {}^m u_{1,3} \partial_3 & & {}^m u_{2,3} \partial_3 & & \partial_3 + {}^m u_{3,3} \partial_3 \\ & {}^m u_{1,2} \partial_3 + {}^m u_{1,3} \partial_2 & & \partial_3 + {}^m u_{2,2} \partial_3 + {}^m u_{2,3} \partial_2 & & \partial_2 + {}^m u_{3,2} \partial_3 + {}^m u_{3,3} \partial_2 \\ \partial_3 + {}^m u_{1,1} \partial_3 + {}^m u_{1,3} \partial_1 & & & {}^m u_{2,1} \partial_3 + {}^m u_{2,3} \partial_1 & & \partial_1 + {}^m u_{3,1} \partial_3 + {}^m u_{3,3} \partial_1 \\ \partial_2 + {}^m u_{1,1} \partial_2 + {}^m u_{1,2} \partial_1 & & & \partial_1 + {}^m u_{2,1} \partial_2 + {}^m u_{2,2} \partial_1 & & & {}^m u_{3,1} \partial_2 + {}^m u_{3,2} \partial_1 \end{bmatrix}, \quad (2.55)$$

which is clearly dependent on the derivatives of the displacement field in configuration (m). The form of $\underline{\mathbf{D}}_{\approx L}$ follows directly from the definition of $\Delta \underline{\mathbf{E}}^{lin}$ in equation 2.46. The notation used can be understood as

$$\partial_i = \frac{\partial}{\partial X_i} \quad {}^m u_{i,j} = \frac{\partial {}^m u_i}{\partial X_j}. \quad (2.56)$$

Substituting equation 2.54 into equation 2.53 yields

$$\int_V \delta [\Delta \underline{\mathbf{E}}^{lin}] \cdot [{}^m \underline{\mathbf{C}}_{\approx L} \Delta \underline{\mathbf{E}}^{lin}] dV = \int_V \underline{\mathbf{D}}_{\approx L} \delta [\Delta \underline{\mathbf{u}}] \cdot [{}^m \underline{\mathbf{C}}_{\approx L} \underline{\mathbf{D}}_{\approx L} \Delta \underline{\mathbf{u}}] dV. \quad (2.57)$$

Making use of the relation $\mathbf{A} \mathbf{u} \cdot \mathbf{v} = \mathbf{u} \cdot \mathbf{A}^T \mathbf{v}$ yields

$$\int_V \underline{\mathbf{D}}_{\approx L} \delta [\Delta \underline{\mathbf{u}}] \cdot [{}^m \underline{\mathbf{C}}_{\approx L} \underline{\mathbf{D}}_{\approx L} \Delta \underline{\mathbf{u}}] dV = \int_V \delta [\Delta \underline{\mathbf{u}}] \cdot \underline{\mathbf{D}}_{\approx L}^T {}^m \underline{\mathbf{C}}_{\approx L} \underline{\mathbf{D}}_{\approx L} \Delta \underline{\mathbf{u}} dV. \quad (2.58)$$

This representation already reminds us heavily of the finite element formulation and should be the end result for now.

There are two other terms to be considered in equation 2.51 that will now be treated in a similar way. The second term on the left-hand side can be written as

$$\int_V {}^m \mathbf{S} : \delta \Delta \mathbf{E}^{nl} dV = \int_V {}^m \mathbf{S} : [\delta (\Delta \mathbf{G})^T \Delta \mathbf{G}] dV. \quad (2.59)$$

Using the relation $\mathbf{A} : \mathbf{BC} = \text{tr}(\mathbf{AC}^T \mathbf{B}^T) = \text{tr}(\mathbf{B}^T \mathbf{AC}^T) = \mathbf{B}^T \mathbf{A} : \mathbf{C}$ gives

$$\int_V {}^m \mathbf{S} : [\delta (\Delta \mathbf{G})^T \Delta \mathbf{G}] dV = \int_V [\delta (\Delta \mathbf{G})^m \mathbf{S}] : \Delta \mathbf{G} dV. \quad (2.60)$$

A similar notation to Voigt's notation, used in the last derivation is now intended. Due to the general non-symmetry of $\Delta \mathbf{G}$, $\Delta \underline{\mathbf{G}}$ is now a $[9 \times 1]$ vector. In order to be able to write $\mathbf{A} : \mathbf{B}$ as $\underline{\mathbf{A}}^T \underline{\mathbf{B}}$, this equation needs to be rewritten as

$$\int_V [\delta (\Delta \mathbf{G})^m \mathbf{S}] : \Delta \mathbf{G} dV = \int_V \delta (\Delta \underline{\mathbf{G}}^T)^m \underline{\mathbf{S}} \underline{\Delta \mathbf{G}} dV, \quad (2.61)$$

2.5. TRANSITION TO THE NON-LINEAR FEM

where ${}^m\mathbf{S}$ is now a $[9 \times 9]$ field with the following assignment

$${}^m\mathbf{S} = \begin{bmatrix} {}^m\mathbf{S} & \mathbf{0} & \mathbf{0} \\ \mathbf{0} & {}^m\mathbf{S} & \mathbf{0} \\ \mathbf{0} & \mathbf{0} & {}^m\mathbf{S} \end{bmatrix}. \quad (2.62)$$

In analogy to equation 2.54, the increment of the displacement gradient and its variation can be written as

$$\Delta\mathbf{G} = \mathbf{D}_{\approx NL} \Delta\mathbf{u} \quad \delta[\Delta\mathbf{G}] = \mathbf{D}_{\approx NL} \delta[\Delta\mathbf{u}], \quad (2.63)$$

where $\mathbf{D}_{\approx NL}$ is the $[9 \times 3]$ differential operator matrix

$$\begin{bmatrix} \partial_1 & 0 & 0 \\ \partial_2 & 0 & 0 \\ \partial_3 & 0 & 0 \\ 0 & \partial_1 & 0 \\ 0 & \partial_2 & 0 \\ 0 & \partial_3 & 0 \\ 0 & 0 & \partial_1 \\ 0 & 0 & \partial_2 \\ 0 & 0 & \partial_3 \end{bmatrix}. \quad (2.64)$$

This leads to

$$\int_V \delta(\Delta\mathbf{G}^T) {}^m\mathbf{S} \Delta\mathbf{G} \, dV = \int_V \delta[\Delta\mathbf{u}] \cdot \mathbf{D}_{\approx NL}^T {}^m\mathbf{S} \mathbf{D}_{\approx NL} \Delta\mathbf{u} \, dV. \quad (2.65)$$

The last term to be investigated in equation 2.51 is the second term on the right-hand side. With the considerations used before, this term can be rewritten without additional effort as

$$\begin{aligned} \int_V {}^m\mathbf{S} : \delta\Delta\mathbf{E}^{lin} \, dV &= \int_V {}^m\mathbf{S} \cdot \delta\Delta\mathbf{E}^{lin} \, dV \\ &= \int_V \delta\Delta\mathbf{E}^{lin} \cdot {}^m\mathbf{S} \, dV \\ &= \int_V \mathbf{D}_{\approx L} \delta[\Delta\mathbf{u}] \cdot {}^m\mathbf{S} \, dV \\ &= \int_V \delta[\Delta\mathbf{u}]^T \mathbf{D}_{\approx L}^T {}^m\mathbf{S} \, dV \\ &= \int_V \delta[\Delta\mathbf{u}]^T \mathbf{D}_{\approx L}^T {}^m\mathbf{S} \, dV \\ &= \int_V \delta[\Delta\mathbf{u}] \cdot \mathbf{D}_{\approx L}^T {}^m\mathbf{S} \, dV. \end{aligned} \quad (2.66)$$

Summarizing the last transformations, equation 2.51 can finally be written as

$$\int_V \delta[\Delta \underline{\mathbf{u}}] \cdot \underline{\underline{\mathbf{D}}}_L^{Tm} \underline{\underline{\mathbf{C}}} \underline{\underline{\mathbf{D}}}_L \Delta \underline{\mathbf{u}} \, dV + \int_V \delta[\Delta \underline{\mathbf{u}}] \cdot \underline{\underline{\mathbf{D}}}_{NL}^{Tm} \underline{\underline{\mathbf{S}}} \underline{\underline{\mathbf{D}}}_{NL} \Delta \underline{\mathbf{u}} \, dV =$$

$${}^{m+1}\delta W_{ext} - \int_V \delta[\Delta \underline{\mathbf{u}}] \cdot \underline{\underline{\mathbf{D}}}_L^{Tm} \underline{\underline{\mathbf{S}}} \, dV. \quad (2.67)$$

It has again to be noted that this expression implies deformation-independent external loads.

Chapter 3

Finite Element Method

The basis for the following sections were the books of Bathe (1996), Wriggers (2008) and Zienkiewicz and Taylor (2000).

The standard formulation of finite element method for solids is the displacement-based method, in which the nodal displacements are the solution field. In section 2.5, some important equations towards this formulation have been established, and will be completed in this chapter.

The main aspect of finite element analysis in general is subdividing a given body into finite elements, as shown in figure 3.1 for a two-dimensional domain. This subdivision process allows us to write the volume and surface integrals in equation 2.67 in terms of a sum over the amount of elements M in the element assemblage

$$\begin{aligned}\int_V (\dots) dV &= \sum^M \int_{V^{(e)}} (\dots) dV^{(e)} \\ \int_S (\dots) dS_F &= \sum^M \int_{S_F^{(e)}} (\dots) dS_F^{(e)},\end{aligned}\tag{3.1}$$

where the superscript (e) will from now on denote quantities of element e . We can see that the calculations are performed over the element volumes and surfaces only, therefore any convenient coordinate system can be used. Thus, it is practical to switch over to a natural coordinate system for each element, which is also shown in figure 3.1. Using a mapping to a natural coordinate system is one aspect of the isoparametric concept.

3.1 Isoparametric Concept

In general in finite element analysis, the main field variables are approximated by interpolation functions. In case of the displacement-based formulation, these main field variables are, naturally, the displacements itself. The interpolation in natural

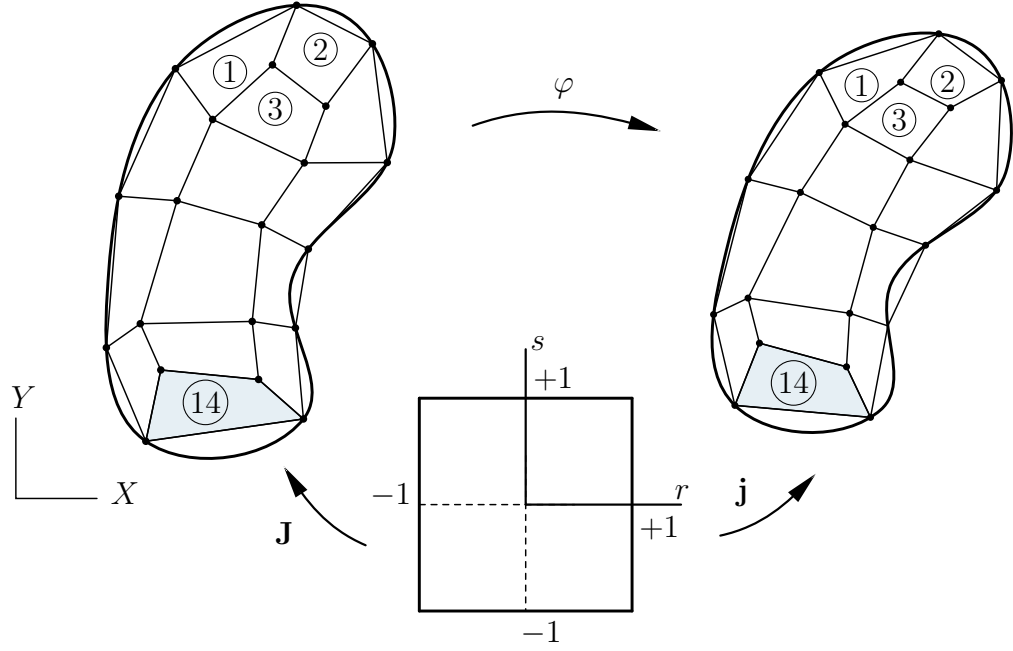


Figure 3.1: Left side: discretization of a two-dimensional body in the material configuration. Clearly, the surface of the outer element boundary only approximates the real body surface. Right side: discretized body in the spatial configuration. Middle: mapping of element 14 in natural coordinates.

coordinates for any element reads as

$$\mathbf{u} = \sum_{i=1}^n N_i(\mathbf{r}) \hat{\mathbf{u}}_i, \quad (3.2)$$

where n is the number of nodes of the element, \mathbf{r} are the natural coordinates, $N_i(\mathbf{r})$ is the shape function for node i and $\hat{\mathbf{u}}_i$ are the displacements for node i . This allows to write the displacements as

$$\mathbf{u} = \mathbf{H}(\mathbf{r}) \hat{\mathbf{u}} \quad (3.3)$$

using the displacement interpolation matrix \mathbf{H} .

Isoparametric means that the geometry is interpolated in the same way as the displacements. For the material and spatial coordinates we can therefore write

$$\mathbf{X} = \sum_{i=1}^n N_i(\mathbf{r}) \hat{\mathbf{X}}_i \quad \text{and} \quad \mathbf{x} = \sum_{i=1}^n N_i(\mathbf{r}) \hat{\mathbf{x}}_i \quad (3.4)$$

The mapping from the natural coordinates to material and spatial coordinates is done by the Jacobian matrices

$$\mathbf{J} = \frac{\partial \mathbf{X}}{\partial \mathbf{r}} \quad \text{and} \quad \mathbf{j} = \frac{\partial \mathbf{x}}{\partial \mathbf{r}}. \quad (3.5)$$

3.1. ISOPARAMETRIC CONCEPT

This allows us to calculate the deformation gradient as

$$\mathbf{F} = \mathbf{j} \mathbf{J}^{-1}. \quad (3.6)$$

Interpolation functions that work well with the isoparametric concept are Lagrangian polynomials

$$l_k^n(r) = \prod_{\substack{i=0 \\ i \neq k}}^n \frac{r - r_i}{r_k - r_i}, \quad (3.7)$$

where n describes the order of the polynomial. Therefore, $n = 1$ leads to linear functions, $n = 2$ to quadratic functions etc. The usage of these polynomials leads to the so-called Lagrangian elements. A few of those elements will now be introduced for one- and two-dimensional problems. The transition to the third dimension is naturally given. There are many other different types of elements available. For a comprehensive overview of available elements see e.g. [Wriggers \(2008\)](#) and [Zienkiewicz and Taylor \(2000\)](#).

3.1.1 One-dimensional Lagrange elements

In one dimensional problems described by a variable r , the shape function reads as

$$N_i(r) = l_k^n(r), \quad (3.8)$$

with the Lagrange polynomial given in equation 3.7.

For the linear one-dimensional Lagrange element shown in figure 3.2a, n is chosen to be 1 and the shape functions for the two nodes are

$$N_1^1(r) = \frac{1}{2}(1 - r) \quad N_2^1(r) = \frac{1}{2}(1 + r). \quad (3.9)$$

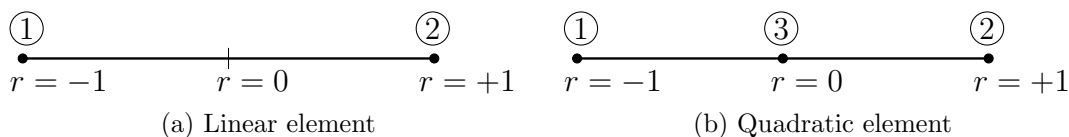


Figure 3.2: One-dimensional Lagrange elements

For the quadratic one-dimensional Lagrange element shown in figure 3.2b, n is chosen to be 2 and the shape functions for the three nodes are accordingly

$$N_1^2(r) = \frac{1}{2}r(r - 1) \quad N_2^2(r) = \frac{1}{2}r(r + 1) \quad N_3^2(r) = 1 - r^2. \quad (3.10)$$

One can already see that the shape function N_i has the value 1 at node i and 0 on all others. This property is also preserved in higher dimensions and higher polynomial order.

3.1.2 Two-dimensional Lagrange elements

Rectangular Lagrange elements The shape functions for these elements are obtained by multiplication of the Lagrangian polynomials in their two directions r and s . Thus, for the linear Lagrangian element shown in figure 3.3a it follows that

$$N_i(r, s) = N_{IJ} = l_I^1(r)l_J^1(s), \quad (3.11)$$

where node i is represented by a node number I in direction of r and an accordingly node number J in s -direction.

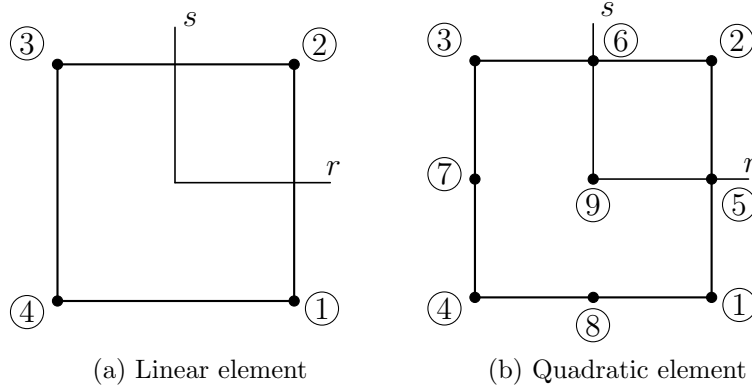


Figure 3.3: Two-dimensional rectangular Lagrange elements

And for the quadratic element in figure 3.3b, we can write

$$N_i(r, s) = N_{IJ} = l_I^2(r)l_J^2(s). \quad (3.12)$$

This procedure can be pursued to gain cubic and higher order rectangular Lagrange elements using

$$N_i(r, s) = N_{IJ} = l_I^n(r)l_J^n(s). \quad (3.13)$$

Note that we assumed the same amount of nodes n in direction of r and s here, as this is the standard case.

Triangular Lagrange elements For these elements, the approach is to write the shape functions as a multiplication of three Lagrange polynomials

$$N_i(L_1, L_2, L_3) = l_I^I(L_1)l_J^J(L_2)l_K^K(L_3), \quad (3.14)$$

where L_i are the area coordinates of the triangle. In natural coordinates, these area coordinates correspond to

$$L_1 = r \quad L_2 = s \quad L_3 = 1 - r - s. \quad (3.15)$$

The meaning of the indices I, J and K will become clear in the light of figure 3.5. For the linear triangular element shown in figure 3.4a, this simply yields

$$N_1 = L_1 = r \quad N_2 = L_2 = s \quad N_3 = L_3 = 1 - r - s, \quad (3.16)$$

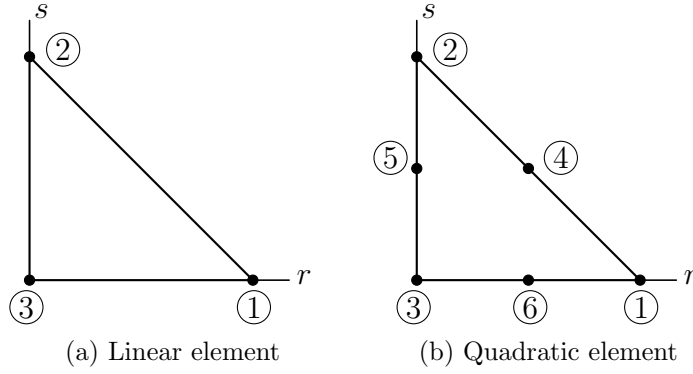


Figure 3.4: Two-dimensional triangular Lagrange elements

and for the quadratic element, shown in figure 3.4b, this gives

$$N_1 = L_1(2L_1 - 1), \quad N_2 = \dots \quad (3.17)$$

for corner nodes, and

$$N_4 = 4L_1L_2, \quad N_5 = \dots \quad (3.18)$$

for mid-side nodes.

3.1.3 Computation of derivatives

In order to compute the strains, derivatives of the displacements in the form

$$\frac{\partial \mathbf{u}}{\partial \mathbf{X}} = \sum_{i=1}^n \frac{\partial N_i(\mathbf{r})}{\partial \mathbf{X}} \hat{\mathbf{u}}_i \quad (3.19)$$

are needed. Since the shape functions depend on the natural coordinates, the chain rule has to be applied

$$\frac{\partial \mathbf{u}}{\partial \mathbf{X}} = \left(\sum_{i=1}^n \frac{\partial N_i(\mathbf{r})}{\partial \mathbf{r}} \hat{\mathbf{u}}_i \right) \frac{\partial \mathbf{r}}{\partial \mathbf{X}}, \quad (3.20)$$

where $\partial \mathbf{r} / \partial \mathbf{X}$ is the inverse of the Jacobian operator matrix defined in equation 3.5.

For example, the component-wise derivatives for the two-dimensional rectangular Lagrange element are

$$\frac{\partial N_i(\mathbf{r})}{\partial r} = \frac{\partial l_I^n(r)}{\partial r} l_J^n(s) \quad \text{and} \quad \frac{\partial N_i(\mathbf{r})}{\partial s} = l_I^n(r) \frac{\partial l_J^n(s)}{\partial s}. \quad (3.21)$$

And for the two-dimensional triangular Lagrange elements, the derivatives are

$$\frac{\partial N_i(\mathbf{r})}{\partial r} = \frac{\partial l_I^I(r)}{\partial r} l_J^J(s) l_K^K(1-r-s) + l_I^I(r) l_J^J(s) \frac{\partial l_K^K(1-r-s)}{\partial r} \quad (3.22)$$

and

$$\frac{\partial N_i(\mathbf{r})}{\partial s} = l_I^I(r) \frac{\partial l_J^J(s)}{\partial s} l_K^K(1-r-s) + l_I^I(r) l_J^J(s) \frac{\partial l_K^K(1-r-s)}{\partial s}. \quad (3.23)$$

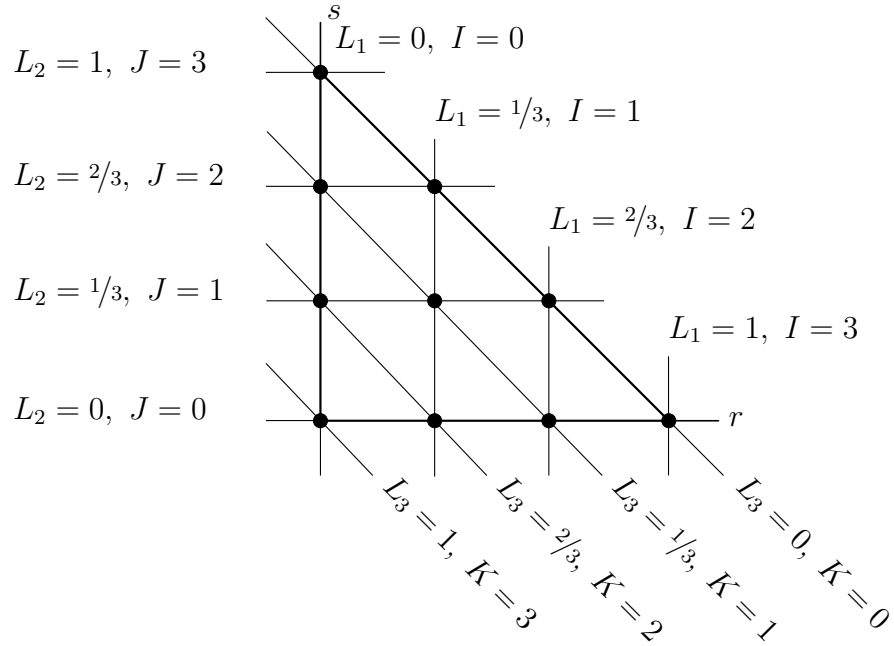


Figure 3.5: Indices I, J, K for the cubic triangular Lagrange element. Note that for every node, $I + J + K = M = 3$, whereas $M = 1$ for the linear element and $M = 2$ for the quadratic element.

3.1.4 Integration over the reference volume

By using a mapping to natural coordinates, the volume integrals of an element e can be written as

$$\int_{V^{(e)}} f(\mathbf{X}) dV^{(e)} = \int_{-1}^{+1} \int_{-1}^{+1} \int_{-1}^{+1} f(r, s, t) \det \mathbf{J} dr ds dt. \quad (3.24)$$

Due to rational terms, these integrals are usually evaluated numerically. An efficient method is using the Gauss quadrature

$$\int_{-1}^{+1} \int_{-1}^{+1} \int_{-1}^{+1} f(r, s, t) \det \mathbf{J} dr ds dt \approx \sum_{p=1}^{n_p} f(r_p, s_p, t_p) \det \mathbf{J}(r_p, s_p, t_p) W_p, \quad (3.25)$$

where n_p is the number of evaluation points (or Gauss points) with coordinates r_p, s_p and t_p . The function $f(\mathbf{r})$ and the Jacobian operator matrix are evaluated at the Gauss points and multiplied with weighting factors W_p . The number of Gauss points is related to the order of the polynomials in the integrand. For an overview of coordinates \mathbf{r}_p and corresponding weighting factors for different element types see [Wriggers \(2008\)](#).

3.2 Linear/Non-linear Finite Element Analysis

The two main subgroups of finite element analysis of solid materials are the linear and non-linear analysis. In the last section a basis for the non-linear formulation was established, without any discussion of its meaning.

The non-linear effects, that necessitate a non-linear analysis, originate from

- geometric (or kinematic) non-linearity due to large strains and rotations,
- material non-linearity, where the material stress response is a non-linear function of the applied strains and can also be path-dependent,
- non-linear boundary conditions (contact problems),
- or equilibrium bifurcation.

In contrast to this, linear analysis can only be applied if none of those non-linearities are present. Considering the first point, this means that only small strains and rotations exist, so that the infinite strain measures may be applied and the deformed configuration differs only little from the material configuration. In the light of material response, this means that the stresses are strictly linearly dependent on the strains. Also there are no non-linear boundary conditions or bifurcations of equilibrium. There are of course cases where some of the mentioned non-linearities are present, while others are not, such as in ‘material non-linearity only’, where the strains and rotations are small, but the material behavior is non-linear.

One can already assume that the non-linear finite element formulation is more general and the linear finite element formulation can be derived through some simplifications. Before we finish the non-linear formulation, these simplifications will now be shown first, as this discussion will be useful in the subsequent non-linear formulation.

3.2.1 Linear finite element formulation

In this section, the spatial virtual work equation will be adapted to fit linear finite element analysis.

In the light of remark 2.4.1, equation 2.34 will be stated here again, as it will be the basis for the following procedure

$$\delta W = \underbrace{- \int_v \boldsymbol{\sigma} : \delta \boldsymbol{\varepsilon} dv}_{\delta W_{int}} + \underbrace{\int_v \delta \mathbf{u} \cdot \mathbf{f}^B dv + \int_{s_F} \delta \mathbf{u} \cdot \mathbf{t}^S ds_F}_{\delta W_{ext}} = 0.$$

For small deformations and rotations, the spatial configuration differs only little from the material configuration, so it can be assumed that $dv = dV$, $ds_F = dS_F$

and, therefore, there can also be no deformation-dependent load. Due to the symmetry of $\boldsymbol{\sigma}$ and $\delta\boldsymbol{\varepsilon}$ we can again use Voigt notation and write

$$\int_V \delta \underline{\underline{\boldsymbol{\varepsilon}}}^T \underline{\underline{\boldsymbol{\sigma}}} dV = \int_V \delta \underline{\underline{\mathbf{u}}}^T \underline{\underline{\mathbf{f}}}^B dV + \int_{S_F} \delta \underline{\underline{\mathbf{u}}}^T \underline{\underline{\mathbf{t}}}^S dS_F. \quad (3.26)$$

As we also assume linear-elastic material behavior, the Cauchy stresses can be written as $\underline{\underline{\boldsymbol{\sigma}}} = \underline{\underline{\mathbf{C}}}\underline{\underline{\boldsymbol{\varepsilon}}}$. The strains can be written as

$$\underline{\underline{\boldsymbol{\varepsilon}}} = \underline{\underline{\mathbf{D}}}\underline{\underline{\mathbf{u}}}, \quad (3.27)$$

where $\underline{\underline{\mathbf{D}}}$ is the differential operator matrix

$$\underline{\underline{\mathbf{D}}} = \begin{bmatrix} \frac{\partial}{\partial x} & 0 & 0 \\ 0 & \frac{\partial}{\partial y} & 0 \\ 0 & 0 & \frac{\partial}{\partial z} \\ \frac{\partial}{\partial y} & \frac{\partial}{\partial x} & 0 \\ 0 & \frac{\partial}{\partial z} & \frac{\partial}{\partial y} \\ \frac{\partial}{\partial z} & 0 & \frac{\partial}{\partial x} \end{bmatrix} \quad (3.28)$$

in case of an x, y, z coordinate system.

When using isoparametric elements as shown in section 3.1, the displacements are interpolated using the interpolation matrix $\underline{\underline{\mathbf{H}}}^{(m)}(r, s, t)$. As $\underline{\underline{\mathbf{H}}}^{(m)}$ is dependent on natural coordinates rather than global coordinates, the elements of the differential operator matrix $\underline{\underline{\mathbf{D}}}$ need to be written as

$$\begin{bmatrix} \frac{\partial}{\partial x} \\ \frac{\partial}{\partial y} \\ \frac{\partial}{\partial z} \end{bmatrix} = \underbrace{\begin{bmatrix} \frac{\partial r}{\partial x} & \frac{\partial s}{\partial x} & \frac{\partial t}{\partial x} \\ \frac{\partial r}{\partial y} & \frac{\partial s}{\partial y} & \frac{\partial t}{\partial y} \\ \frac{\partial r}{\partial z} & \frac{\partial s}{\partial z} & \frac{\partial t}{\partial z} \end{bmatrix}}_{\mathbf{J}^{-1}} \begin{bmatrix} \frac{\partial}{\partial r} \\ \frac{\partial}{\partial s} \\ \frac{\partial}{\partial t} \end{bmatrix}. \quad (3.29)$$

This gives

$$\underline{\underline{\boldsymbol{\varepsilon}}}^{(e)} = \underline{\underline{\mathbf{B}}}^{(e)}(r, s, t)\hat{\underline{\underline{\mathbf{u}}}}, \quad (3.30)$$

where the strain-displacement matrix $\underline{\underline{\mathbf{B}}}^{(e)}(r, s, t)$ was gained by using the (modified) differential operator matrix on the interpolation matrix

$$\underline{\underline{\mathbf{B}}}^{(e)}(r, s, t) = \underline{\underline{\mathbf{D}}}\underline{\underline{\mathbf{H}}}^{(e)}(r, s, t). \quad (3.31)$$

The values of $\underline{\underline{\mathbf{B}}}^{(e)}$ are derivatives of the shape functions with respect to the natural coordinates. These derivatives were already presented for some Lagrangian element types in section 3.1.3.

The same procedure applied on the virtual strain gives

$$\delta \underline{\underline{\boldsymbol{\varepsilon}}}^{(e)} = \underline{\underline{\mathbf{B}}}^{(e)}(r, s, t)\delta\hat{\underline{\underline{\mathbf{u}}}}. \quad (3.32)$$

Using the above, and defining the nodal displacement vector $\hat{\mathbf{u}}$ as well as the virtual nodal displacements $\delta\hat{\mathbf{u}}$ to have n entries, where n are the total degrees of freedom, the left side of equation 3.26 is

$$\delta\hat{\mathbf{u}}^T \underbrace{\sum_{i=1}^M \int_{V_r^{(e)}} \underbrace{\mathbf{B}^{(e)T} \mathbf{C}^{(e)} \mathbf{B}^{(e)}}_{\mathbf{K}^{(e)}} \det(\mathbf{J}) dV_r^{(e)}}_{\mathbf{K}} \hat{\mathbf{u}}, \quad (3.33)$$

where the volume integration is approximated by the sum of element integrations over the volume $V_r^{(e)}$ in natural coordinates, which are usually evaluated in a numeric way, e.g. as shown in section 3.1.4. The virtual and real nodal displacements are independent of volume and have therefore been pulled out of the integrand. $\mathbf{K}^{(e)}$ is the element stiffness matrix, and \mathbf{K} is the stiffness matrix of the element assemblage. The summation in equation 3.33 must be understood as an assembling operation. For further information please see e.g. Bathe (1996) or Zienkiewicz and Taylor (2000).

For the right side of equation 3.26, an analogous procedure leads to

$$\delta\hat{\mathbf{u}}^T \underbrace{\sum_{i=1}^M \int_{V_r^{(e)}} \underbrace{\mathbf{H}^{(e)T} \mathbf{f}^B}_{\mathbf{F}_{ext}^{B(e)}} \det(\mathbf{J}) dV_r^{(e)}}_{\mathbf{F}_{ext}^B} \quad (3.34)$$

and

$$\delta\hat{\mathbf{u}}^T \underbrace{\sum_{i=1}^M \int_{S_{rF}^{(e)}} \underbrace{\mathbf{H}_S^{(e)T} \mathbf{t}^S}_{\mathbf{F}_{ext}^{S(e)}} \det(\mathbf{J}_S) dS_{rF}^{(e)}}_{\mathbf{F}_{ext}^S}, \quad (3.35)$$

where the Jacobian matrix \mathbf{J}_S is a mapping of the surface area in the natural coordinates to a surface area in global coordinates, and the surface interpolation matrices $\mathbf{H}_S^{(e)T}$ are obtained by proper adaption of the elements of the interpolation matrices $\mathbf{H}^{(e)T}$.

Inserting the results of equations 3.33, 3.34 and 3.35 into equation 3.26 and applying the principle of virtual displacements n times, where

$$\delta\hat{\mathbf{u}}_1^T = [1 \ 0 \ 0 \ \dots], \quad \delta\hat{\mathbf{u}}_2^T = [0 \ 1 \ 0 \ \dots], \quad \dots, \quad \delta\hat{\mathbf{u}}_n^T = [\dots \ 0 \ 0 \ 1]$$

leads to the well-known set of equations

$$\boxed{\mathbf{K} \hat{\mathbf{u}} = \underbrace{\mathbf{F}_{ext}^B + \mathbf{F}_{ext}^S}_{\mathbf{F}_{ext}}}. \quad (3.36)$$

After incorporation of the boundary conditions, this set of equations allows us to compute the unknown nodal displacements $\hat{\mathbf{u}}$. For the sake of brevity, we will not show how the boundary conditions can be included into equation 3.36. For discussion of this topic see e.g. Bathe (1996).

3.2.2 Non-linear finite element formulation

In the last step in section 2.5, we gained equation 2.67

$$\int_V \delta[\Delta \mathbf{u}] \cdot \mathbf{D}_{\approx L}^T m \mathbf{C}_{\approx L} \Delta \mathbf{u} \, dV + \int_V \delta[\Delta \mathbf{u}] \cdot \mathbf{D}_{\approx NL}^T m \mathbf{S}_{\approx NL} \Delta \mathbf{u} \, dV = {}^{m+1}\delta W_{ext} - \int_V \delta[\Delta \mathbf{u}] \cdot \mathbf{D}_{\approx L}^T m \mathbf{S} \, dV,$$

where deformation-independent loads were postulated. For simplicity reasons, deformation-dependent loads will also not be part of this section. For discussion of this topic see again e.g. Bathe (1996).

With the knowledge gained in the last section, the first term on the left-hand side of this equation can be rewritten as

$$\delta \Delta \hat{\mathbf{u}}^T \underbrace{\sum_{i=1}^M \int_{V_r^{(e)}} \mathbf{B}_{\approx L}^{(e)T} m \mathbf{C}_{\approx L}^{(e)} \mathbf{B}_{\approx L}^{(e)} \det(\mathbf{J}) \, dV_r^{(e)}}_{m \mathbf{K}_{\approx L}} \Delta \hat{\mathbf{u}}, \quad (3.37)$$

where $m \mathbf{K}_{\approx L}$ is the linear strain incremental stiffness matrix.

Accordingly, the second term on the left-hand side is

$$\delta \Delta \hat{\mathbf{u}}^T \underbrace{\sum_{i=1}^M \int_{V_r^{(e)}} \mathbf{B}_{\approx NL}^{(e)T} m \mathbf{S}_{\approx NL}^{(e)} \mathbf{B}_{\approx NL}^{(e)} \det(\mathbf{J}) \, dV_r^{(e)}}_{m \mathbf{K}_{\approx NL}} \Delta \hat{\mathbf{u}}, \quad (3.38)$$

where $m \mathbf{K}_{\approx NL}$ is the non-linear strain incremental stiffness matrix.

In the computation of the linear and non-linear strain-displacement matrices $\mathbf{B}_{\approx L}^{(e)}$ and $\mathbf{B}_{\approx NL}^{(e)}$ the influence of the natural coordinate mapping must be included properly, as already mentioned in section 3.2.1.

The first term on the right-hand side, that represents the external virtual work, ${}^{m+1}\delta W_{ext}$ can be adopted directly from equation 3.34 and 3.35. The second term on the right-hand side can be represented as

$$\delta \Delta \hat{\mathbf{u}}^T \underbrace{\sum_{i=1}^M \int_{V_r^{(e)}} \mathbf{B}_{\approx L}^{(e)T} m \mathbf{S}^{(e)} \det(\mathbf{J}) \, dV_r^{(e)}}_{m \mathbf{F}_{\approx int}}, \quad (3.39)$$

where ${}^m\mathbf{F}_{int}$ is the internal force vector. The element volume integrations in all of these terms are again usually evaluated numerically as briefly shown in section 3.1.4.

The results of equation 3.37, 3.38, 3.34, 3.35 and 3.39 together with the usage of the principle of virtual displacements mentioned in section 3.2.1 leads to the non-linear finite element formulation

$$\boxed{\underbrace{\left({}^m\mathbf{K}_{\approx L} + {}^m\mathbf{K}_{\approx NL} \right)}_{{}^m\mathbf{K}_{\approx}} \Delta \hat{\mathbf{u}} = {}^{m+1}\mathbf{F}_{\approx ext} - {}^m\mathbf{F}_{\approx int}}. \quad (3.40)$$

After the boundary conditions are included, the increments of the nodal displacements $\Delta \hat{\mathbf{u}}$ can be calculated iteratively e.g. using the Newton-Raphson method briefly discussed in the next section.

3.2.3 Newton-Raphson method

A standard iterative solver for non-linear finite element analysis, the Newton-Raphson (NR) method, is now introduced. The steps of this process will now be illustrated.

1. The system is in equilibrium in configuration (m), which means that the internal forces ${}^m\mathbf{F}_{int}$ and external forces ${}^m\mathbf{F}_{ext}$ are in balance.
2. The load is increased to ${}^{m+1}\mathbf{F}_{ext}$. This introduces imbalance to the system. A new equilibrium configuration ($m + 1$) is intended.
3. Initialization of the Newton-Raphson procedure.

$$\begin{aligned} \mathbf{u}^{(0)} &= {}^m\mathbf{u} \\ \mathbf{F}_{int}^{(0)} &= {}^m\mathbf{F}_{ext} \end{aligned}$$

4. Solve

$$\mathbf{K}_{\approx}^{(i)} \Delta \mathbf{u} = {}^{m+1}\mathbf{F}_{ext} - \mathbf{F}_{int}^{(i)}$$

for $\Delta \mathbf{u}$, calculate the displacements

$$\mathbf{u}^{(i+1)} = \mathbf{u}^{(i)} + \Delta \mathbf{u}$$

and use $\mathbf{u}^{(i+1)}$ to calculate the strains and stresses. Use the results to calculate the internal force vector ${}^{m+1}\mathbf{F}_{int}$

5. The unbalanced force vector which can be obtained as

$${}^{m+1}\mathbf{R} = {}^{m+1}\mathbf{F}_{ext} - {}^{m+1}\mathbf{F}_{int}, \quad (3.41)$$

can then be used to determine the accuracy of the calculated displacements $\mathbf{u}^{(i+1)}$ through a variety of available convergence criteria.

6. Now there are three possible outcomes:
- (a) If the convergence criteria is not met, steps 4 and 5 have to be repeated.
 - (b) If the iterations exceed a maximum iteration amount i_{max} , the system is divergent. Which in most cases is caused by oversized load increments.
 - (c) If the results are satisfying, i.e. the convergence criteria is met, a state of equilibrium has been found. If another load increment has to be applied, return to step 2. If not, continue with postprocessing steps.

Chapter 4

Molecular Dynamics (MD)

The basis for the following sections was the work of [Ulz \(2015\)](#) and the books of [Tadmor and Miller \(2011\)](#) and [Weiner \(2002\)](#).

In molecular dynamics, atoms are simulated as classical Newtonian particles. The motion of these atoms is traced by integration of the equations of motion.

Since molecular dynamics originates from statistical mechanics, simulations corresponding to certain macroscopic constraints are described using statistical ensembles. To help understanding the ensemble concept, let us first have a look at the simplest atomic system, which is the NVE system. Here, a cell of N atoms is constrained to occupy a fixed volume V , while the energy of the whole system E is kept constant. The system is fully characterized at all times t by the atoms' generalized positions \mathbf{q} and generalized momenta \mathbf{p} . The set of these generalized positions and momenta is called the microstate of the system. A set of given macroscopic constraints, such as N, V and E in this case, can be reflected by a large amount of microstates. The collection of all microstates consistent with certain macroscopic constraints is called ensemble.

In contrast to keeping the energy E constant, one is often more interested in systems with constant temperature T . This leads to NVT systems, which are part of the NVT ensemble. In order to keep T constant in a MD simulation, the system is connected to a heatbath which supplies/withdraws energy to/from the atoms. This connection may be established by different thermostats, such as the Nosé thermostat ([Nosé \(1984\)](#)), used in this work.

4.1 Hamiltonian

In the last chapters, we applied strains and loads on an arbitrary deformable body as we were interested in its response. Our main focus here is similar, we need a model that allows us to extract the stress response and the elastic constants from a loaded MD cell. Figure 4.1 shows adequate mappings for this purpose ([Andersen \(1980\)](#); [Parrinello and Rahman \(1981\)](#); [Podio-Guidugli \(2010\)](#)).

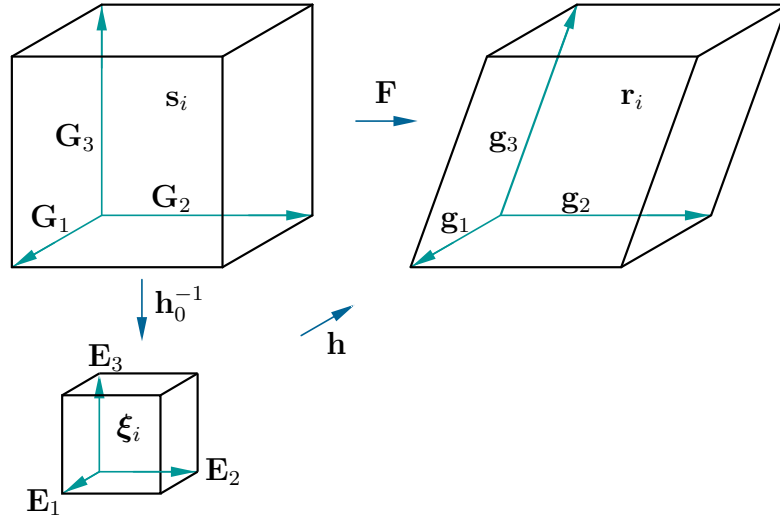


Figure 4.1: Mappings between referential (initial) and current (deformed) MD cell with coordinates \mathbf{s}_i and \mathbf{r}_i , respectively. The referential MD cell may be mapped onto a unit cube with coordinates $\boldsymbol{\xi}_i$ as employed in Parrinello and Rahman (1981). Figure taken from Ulz (2015).

The three linearly independent edge vectors \mathbf{G}_k of the undeformed MD cell transform to \mathbf{g}_k due to deformation. Here, the quantity \mathbf{F} is consistent with the deformation gradient shown in section 2.1 and is therefore referred as the cell deformation gradient. It allows a mapping of the edge vectors and atomic positions

$$\mathbf{g}_k = \mathbf{F}\mathbf{G}_k, \quad \text{and} \quad \mathbf{r}_i = \mathbf{F}\mathbf{s}_i. \quad (4.1)$$

Although the proceedings are similar, there is one important difference to the previous chapters. While the undeformed configuration in chapter 2 and 3 was fixed, in the sense that they did not change their shape and the continuum particles did not change their position, the referential configuration will now still preserve its shape but the positions \mathbf{s}_i will change accordingly with \mathbf{r}_i .

A different mapping was introduced by Parrinello and Rahman (1981), which is also shown in figure 4.1. Here, the referential configuration is mapped onto a unit cube, which is connected to the current configuration by the quantity $\mathbf{h} = [\mathbf{g}_1 \ \mathbf{g}_2 \ \mathbf{g}_3]$.

The following approach of an extended N -particle Hamiltonian was proposed by Ray and Rahman (1985) and is written in terms of continuum mechanics (Podio-Guidugli (2010), Ulz (2013))

$$\begin{aligned} \mathcal{H} &= \mathcal{K}_{\text{atoms}} + \mathcal{V}_{\text{atoms}} + \mathcal{K}_{\text{cell}} + \mathcal{V}_{\text{cell}} + \mathcal{K}_{\text{heatbath}} + \mathcal{V}_{\text{heatbath}} \\ &= \mathbf{C}^{-1} : \frac{1}{2} \sum_{i=1}^N \frac{1}{m_i f^2} \mathbf{p}_i \otimes \mathbf{p}_i + \sum_{i=1}^N E_i \\ &+ \mathbf{P}^T \mathbf{P} : \frac{1}{2} \mathbf{J}^{-1} + \Omega_0 \mathbf{S}^{\text{ext}} : \mathbf{E} + P^2 \frac{1}{2M} + (3N + 1)k_B T_\infty \ln(f). \end{aligned} \quad (4.2)$$

It consists of kinetic terms \mathcal{K}_i and potential terms \mathcal{V}_i . In this form, equation 4.2 is the Hamiltonian for the isostress-isothermal ($N\sigma T$) ensemble. However, slight modifications, which will be discussed later, allow us to obtain the Hamiltonian for the isostress-isenthalpic ($N\sigma H$) ensemble (Andersen (1980); Parrinello and Rahman (1981)), the canonical (NFT) ensemble (Nosé (1984); Hoover (1985); Hünenberger (2005)) or the microcanonical (NFE) ensemble. In equation 4.2, \mathbf{s}_i and \mathbf{p}_i denote the atoms' scaled coordinates and conjugate momenta, respectively. The coordinates and momenta of the MD cell are \mathbf{F} and \mathbf{P} , respectively. The thermostat is introduced by the extra degree of freedom f and the conjugate momentum P .¹ While the atoms' masses are denoted with m_i , there is also a 'thermal mass' M of the heatbath, which affects the thermal equilibration rate. In addition to that, the quantity $\mathbf{J} = \sum_{i=1}^N m_i \mathbf{s}_i \otimes \mathbf{s}_i$ is the referential inertia tensor. The volume in the referential configuration is given by Ω_0 and the externally applied stress is given by \mathbf{S}^{ext} , which is of the same character as the second Piola-Kirchhoff stress in continuum mechanics. The associated quantity \mathbf{E} corresponds to the Green-Lagrange strains and $\mathbf{C}^{-1} = \mathbf{F}^{-1}\mathbf{F}^{-T}$ is the inverse of the right Cauchy-Green deformation tensor. Equation 4.2 further contains the Boltzmann constant k_B and the temperature of the heatbath T_∞ .

4.2 Interatomic Potential

The interatomic potential E_i , contained in the atoms' potential energy term $\mathcal{V}_{\text{atoms}}$, is a central subject of molecular dynamics as it describes the atoms' attraction and repulsion. There are many potentials that approximate these interactions. In this work, the embedded atom model (EAM) (Daw and Baskes (1984)) has been used, since it has shown to be very effective especially for metal systems.

Using EAM, the potential energy of atom i can be written as

$$E_i = F_i \left(\underbrace{\sum_{\substack{j=1 \\ j \neq i}}^N \pi_j(r_{ij})}_{\rho_i} \right) + \frac{1}{2} \sum_{\substack{j=1 \\ j \neq i}}^N \phi_{ij}(r_{ij}) \quad (4.3)$$

where ϕ_{ij} is a pair-wise potential, π_j is the contribution of the electron charge density of atom j to the location of atom i and F_i is the embedding function that represents the energy required to place atom i into the electron cloud and r_{ij} is the distance between atom i and j .

Wadley et al. (2001) proposed a form of the functions ρ , ϕ and F which are used in this work. For improved readability, these functions are shown in appendix A.

¹In contrast to the NVE ensemble mentioned before, where the microstates are given by its Hamiltonian in form of $\mathcal{H}_{NVE} = \mathcal{H}(\mathbf{q}, \mathbf{p})$, the microstates of the $N\sigma T$ ensemble are now defined by additional variables $\mathcal{H}_{N\sigma T} = \mathcal{H}(\mathbf{s}, \mathbf{p}, \mathbf{F}, \mathbf{P}, f, P)$.

In section 4.3, we will show the equations of motion for an atom i . To solve those equations, one first needs to calculate the forces resulting from interaction of atom i with all other atoms $j = 1, \dots, N; i \neq j$ in the system. Again, to facilitate readability, the calculation of the interatomic forces is shown in appendix B.

In order to approximate these interactions properly for all atoms in the MD system, the simulation cell is embedded into bulk material using periodic boundary conditions.

4.2.1 Periodic boundary conditions (PBC)

Periodic boundary conditions are an effective method to simulate bulk material. But why is this necessary?

Due to computational reasons only small portions of material can be simulated. If only one MD cell is investigated, it is easily possible to involve $N = 10^4$ to 10^6 atoms. We will later see though, that we are interested in parallel calculation of hundreds of MD cells. As this would yield unreasonable computational cost, we will only include a few hundred atoms per MD cell. However, when using such a small amount of atoms, a large share is located on the surface of the cell or in close distance to it. Thus treating these surface elements in an inappropriate way will vastly affect the simulation outcome. Although these surface effects are less present in large simulations, using PBC is the standard procedure in molecular dynamics in small and large simulations.

In order to simulate bulk material, replicas of the considered MD cell are attached in each direction to the cell. This is shown in figure 4.2a for a 2-dimensional domain.

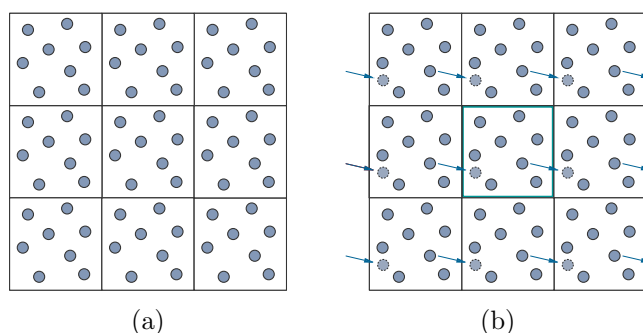


Figure 4.2: Periodic boundary conditions applied to a 2-dimensional simulation. (a) Replication of the original cell. (b) Conservation of the quantity of atoms in the original cell. Figure taken from Wurm (2013).

The atoms in the replicas behave exactly the same way as the original atoms do. When an atom leaves the cell, a replica cell automatically supplies it with a copy of that atom, hence the amount of atoms in the cell is preserved. This is one central property of PBC and is sketched in figure 4.2b. Furthermore, as it is shown in appendix B, the distance between two atoms plays an important

4.3. EQUATIONS OF MOTION (EOM)

role in the calculation of interatomic forces. This leads us to the minimum image convention which states that if we want to compute the interaction of atom j on atom i , only the closest version of atom j will be considered, whether it is in the original cell or in one of the replicas.

4.3 Equations of Motion (EOM)

Hamilton's equations of motion can be found by comparing the total differential of the Hamiltonian in its standard form with its form in terms of the Legendre transformation (see e.g. [Goldstein et al. \(2002\)](#)) as

$$\dot{\mathbf{q}}_i = \frac{\partial \mathcal{H}}{\partial \mathbf{p}_i}, \quad \dot{\mathbf{p}}_i = -\frac{\partial \mathcal{H}}{\partial \mathbf{q}_i}. \quad (4.4)$$

In terms of the Hamiltonian given in equation 4.2 this gives

$$\dot{\mathbf{s}}_i = \frac{\partial \mathcal{H}}{\partial \mathbf{p}_i} = \frac{1}{m_i f^2} \mathbf{C}^{-1} \mathbf{p}_i, \quad \dot{\mathbf{p}}_i = -\frac{\partial \mathcal{H}}{\partial \mathbf{s}_i} = -\mathbf{C} \sum_{j \neq i}^N \frac{\chi_{ij}}{r_{ij}} \mathbf{s}_{ij}, \quad (4.5)$$

$$\dot{\mathbf{F}} = \frac{\partial \mathcal{H}}{\partial \mathbf{P}} = \mathbf{P} \mathbf{J}^{-1}, \quad \dot{\mathbf{P}} = -\frac{\partial \mathcal{H}}{\partial \mathbf{F}} = -\Omega_0 \mathbf{F} (\mathbf{S}^{\text{ext}} + \mathbf{S}^{\text{int}}), \quad (4.6)$$

$$\dot{f} = \frac{\partial \mathcal{H}}{\partial P} = \frac{1}{M} P, \quad \dot{P} = -\frac{\partial \mathcal{H}}{\partial f} = \frac{1}{f} (2K - (3N + 1)k_B T_\infty). \quad (4.7)$$

We will refrain from showing how to obtain these $6N + 20$ equations here as it is quite space-consuming. For an extensive derivation see [Wurm \(2013, Appendix\)](#). The quantity

$$\chi_{ij}(r_{ij}) = \frac{\partial F_j(\rho_j)}{\partial \rho_j} \frac{\partial \pi_i(r_{ji})}{\partial r_{ji}} + \frac{\partial F_i(\rho_i)}{\partial \rho_i} \frac{\partial \pi_j(r_{ij})}{\partial r_{ij}} + \frac{\partial \phi_{ij}(r_{ij})}{\partial r_{ij}}$$

is derived in appendix B. The instantaneous microscopic stress tensor \mathbf{S}^{int} , which will be further discussed in section 4.5, is found during derivation of the EOM as

$$\mathbf{S}^{\text{int}} = \frac{1}{\Omega_0} \left[-\mathbf{C}^{-1} \left(\sum_{i=1}^N \frac{1}{m_i f^2} \mathbf{p}_i \otimes \mathbf{p}_i \right) \mathbf{C}^{-1} + \frac{1}{2} \sum_{i=1}^N \sum_{j \neq i}^N \frac{\chi_{ij}}{r_{ij}} \mathbf{s}_{ij} \otimes \mathbf{s}_{ij} \right]. \quad (4.8)$$

and K is the kinetic energy found as

$$K = \frac{1}{2} \sum_{i=1}^N m_i f^2 \dot{\mathbf{s}}_i^T \mathbf{C} \dot{\mathbf{s}}_i. \quad (4.9)$$

Hamilton's EOM (equation 4.5 to 4.7) can be condensed to have the form of

Lagrange's EOM

$$\ddot{\mathbf{s}}_i m_i f^2 = -m_i \left(f^2 \mathbf{C}^{-1} \dot{\mathbf{C}} + 2f\dot{f} \right) \dot{\mathbf{s}}_i - \sum_{j \neq i}^N \frac{\chi_{ij}}{r_{ij}} \mathbf{s}_{ij}, \quad (4.10)$$

$$\ddot{\mathbf{F}}\mathbf{J} = -\Omega_0 \mathbf{F} (\mathbf{S}^{\text{ext}} + \mathbf{S}^{\text{int}}), \quad (4.11)$$

$$\ddot{f}M = \frac{1}{f} (2K - (3N + 1)k_B T_\infty), \quad (4.12)$$

which are $3N + 10$ second order partial differential equations.

This is a good point to talk about the modifications mentioned before, which allow us to realize different ensembles using the Hamiltonian given in equation 4.2 and the corresponding equations of motion. As previously mentioned, equation 4.2 and the obtained EOM are valid for the $N\sigma T$ ensemble. In order to get the EOM for other ensembles, such as the NFT ensemble used in this thesis, different constraints are used as shown in table 4.1.

$N\sigma H$	$f = 1, \dot{f} = \ddot{f} = 0$
NFT	$\mathbf{F} = \text{const.}, \dot{\mathbf{F}} = \ddot{\mathbf{F}} = \mathbf{0}, \mathbf{S}^{\text{ext}} = \mathbf{0}$
NFE	$\mathbf{F} = \text{const.}, \dot{\mathbf{F}} = \ddot{\mathbf{F}} = \mathbf{0}, \mathbf{S}^{\text{ext}} = \mathbf{0},$ $f = 1, \dot{f} = \ddot{f} = 0$

Table 4.1: Possible ensembles.

4.4 Numerical Integrator: Gear's Predictor Corrector Algorithm

The Lagrangian EOM given in equation 4.10 to 4.12 are integrated numerically for each time step.² The integrator used in this work, a high-order integrator which belongs to the family of predictor-corrector methods, is 'Gear's predictor-corrector' algorithm (Gear (1966); Gear (1971)). As their name implies, predictor-corrector methods consist of two steps. In the first step, the desired variables are predicted and in the second step, the corrected variables are calculated. Gear's method is available in different orders. In this work, a 6th-order scheme is used and will now be briefly presented.

The 6th-order scheme uses a 5th-order Taylor series to approximate a variable

²Special attention must be paid when choosing the time integrator for MD simulations as there are several requirements to be met. For further information please see e.g. Tadmor and Miller (2011).

4.4. NUMERICAL INTEGRATOR

\mathbf{a} and it's derivatives³, which allows the predictor step to be written as

$$\begin{aligned}
 \mathbf{a}_0(t + \Delta t) &= \mathbf{a}_0(t) + \Delta t \frac{d\mathbf{a}(t)}{dt} + \frac{(\Delta t)^2}{2!} \frac{d^2\mathbf{a}(t)}{dt^2} + \\
 &\quad \frac{(\Delta t)^3}{3!} \frac{d^3\mathbf{a}(t)}{dt^3} + \frac{(\Delta t)^4}{4!} \frac{d^4\mathbf{a}(t)}{dt^4} + \frac{(\Delta t)^5}{5!} \frac{d^5\mathbf{a}(t)}{dt^5} \\
 \mathbf{a}_0(t + \Delta t) &= \mathbf{a}_0(t) + \mathbf{a}_1(t) + \mathbf{a}_2(t) + \mathbf{a}_3(t) + \mathbf{a}_4(t) + \mathbf{a}_5(t) \\
 \mathbf{a}_1(t + \Delta t) &= \mathbf{a}_1(t) + 2\mathbf{a}_2(t) + 3\mathbf{a}_3(t) + 4\mathbf{a}_4(t) + 5\mathbf{a}_5(t) \\
 \mathbf{a}_2(t + \Delta t) &= \mathbf{a}_2(t) + 3\mathbf{a}_3(t) + 6\mathbf{a}_4(t) + 10\mathbf{a}_5(t) \\
 \mathbf{a}_3(t + \Delta t) &= \mathbf{a}_3(t) + 4\mathbf{a}_4(t) + 10\mathbf{a}_5(t) \\
 \mathbf{a}_4(t + \Delta t) &= \mathbf{a}_4(t) + 5\mathbf{a}_5(t) \\
 \mathbf{a}_5(t + \Delta t) &= \mathbf{a}_5(t),
 \end{aligned}$$

where we have used the abbreviation

$$\mathbf{a}_n(t) = \frac{(\Delta t)^n}{n!} \frac{d^n \mathbf{a}(t)}{dt^n} \quad (4.13)$$

for $n = 1, 2, 3, 4, 5$.

This can also be written in the more compact form

$$\begin{bmatrix} \mathbf{a}_0^P(t + \Delta t) \\ \mathbf{a}_1^P(t + \Delta t) \\ \mathbf{a}_2^P(t + \Delta t) \\ \mathbf{a}_3^P(t + \Delta t) \\ \mathbf{a}_4^P(t + \Delta t) \\ \mathbf{a}_5^P(t + \Delta t) \end{bmatrix} = \begin{bmatrix} 1 & 1 & 1 & 1 & 1 & 1 \\ 0 & 1 & 2 & 3 & 4 & 5 \\ 0 & 0 & 1 & 3 & 6 & 10 \\ 0 & 0 & 0 & 1 & 4 & 10 \\ 0 & 0 & 0 & 0 & 1 & 5 \\ 0 & 0 & 0 & 0 & 0 & 1 \end{bmatrix} \begin{bmatrix} \mathbf{a}_0(t) \\ \mathbf{a}_1(t) \\ \mathbf{a}_2(t) \\ \mathbf{a}_3(t) \\ \mathbf{a}_4(t) \\ \mathbf{a}_5(t) \end{bmatrix}. \quad (4.14)$$

The corrected values are calculated by

$$\begin{bmatrix} \mathbf{a}_0^C(t + \Delta t) \\ \mathbf{a}_1^C(t + \Delta t) \\ \mathbf{a}_2^C(t + \Delta t) \\ \mathbf{a}_3^C(t + \Delta t) \\ \mathbf{a}_4^C(t + \Delta t) \\ \mathbf{a}_5^C(t + \Delta t) \end{bmatrix} = \begin{bmatrix} \mathbf{a}_0^P(t + \Delta t) \\ \mathbf{a}_1^P(t + \Delta t) \\ \mathbf{a}_2^P(t + \Delta t) \\ \mathbf{a}_3^P(t + \Delta t) \\ \mathbf{a}_4^P(t + \Delta t) \\ \mathbf{a}_5^P(t + \Delta t) \end{bmatrix} + \begin{bmatrix} c_0 \\ c_1 \\ c_2 \\ c_3 \\ c_4 \\ c_5 \end{bmatrix} \Delta \mathbf{a}_2, \quad (4.15)$$

where c_i are the Gear corrector coefficients (also Gear's 'magic numbers') shown in table 4.2 and $\Delta \mathbf{a}_2 = \mathbf{a}_2^C - \mathbf{a}_2^P$ is obtained by substituting \mathbf{a}_0^P and \mathbf{a}_1^P into the equations of motion 4.10 to 4.12.

³The quantity \mathbf{a} can be understood as \mathbf{s} , \mathbf{F} or f . While this notation is correct in the first two cases, the quantity \mathbf{a} should be understood as a scalar a in the third case.

c_0 ⁴	c_1	c_2	c_3	c_4	c_5
$3/16$ or $3/20$	$251/360$	1	$11/18$	$1/6$	$1/60$

Table 4.2: Gear’s magic numbers of the 6th-order scheme for integrating second order differential equations.

4.5 Extraction of Macroscopic Observables

In statistical mechanics, macroscopic observables such as the volume, temperature, density and many more, are calculated using an ensemble average of a phase function $A(\Gamma)$

$$\langle A(t) \rangle = \int_{\Gamma} A(\Gamma) f(\Gamma, t) d\Gamma, \quad (4.16)$$

where Γ is the phase space, which consists of all accessible microstates of the ensemble. The phase space distribution function $f(\Gamma, t)$ gives the probability density per unit phase space, i.e. the probability of finding a system in the region $\Gamma + d\Gamma$ at time t . The distribution function needs to fulfill the normalization condition $\int_{\Gamma} f(\Gamma, t) d\Gamma = 1$.

The ergodic hypothesis implies that for stationary systems, which are represented by a phase space distribution function that does not change in time, the ensemble average can be replaced by a time average

$$\bar{A} = \frac{1}{\Delta t} \int_0^{\Delta t} A(\Gamma(\tau)) d\tau \quad (4.17)$$

over a sufficiently long time frame Δt . This is what in fact justifies the usage of molecular dynamics in statistical mechanics, where quantities are estimated by following a single system over a large amount of timesteps.

As already mentioned in section 4.1, the macroscopic observables of interest to us are the stress response and the elastic constants. These quantities are determined by time-averaging using their microscopic equivalents. These microscopic quantities are obtained through derivatives of thermodynamic potentials with respect to proper deformation measures.

For canonical systems, the corresponding potential is the Helmholtz free energy (Weiner (2002)) defined as

$$\Psi = -k_B T \ln Z = -k_B T \ln \left(\int_{\Gamma} e^{-\frac{\mathcal{H}}{k_B T}} d\Gamma \right), \quad (4.18)$$

⁴It is recommended to use $c_0 = 3/16$ for $\mathbf{a} = \mathbf{s}$ because the first derivative $\dot{\mathbf{s}}$ appears on the right-hand side of equation 4.10. For $\mathbf{a} = \mathbf{F}$ and $\mathbf{a} = f$, $c_0 = 3/20$ should be used. See Allen and Tildesley (2009, Appendix E).

4.5. EXTRACTION OF MACROSCOPIC OBSERVABLES

where Z is the partition function, T is the temperature of the heatbath and \mathcal{H} is the Hamiltonian of equation 4.2 adapted for the NFT ensemble.

A microscopic stress measure, corresponding to the second Piola-Kirchhoff stresses, is obtained by derivation of the Helmholtz free energy with respect to $1/2 \mathbf{C}$

$$\Omega_0 \mathbf{S}^{\text{int}} = 2 \frac{\partial \Psi}{\partial \mathbf{C}} = -2 \frac{k_B T}{Z} \frac{\partial Z}{\partial \mathbf{C}} = 2 \frac{k_B T}{k_B T} \frac{\int_{\Gamma} \frac{\partial \mathcal{H}}{\partial \mathbf{C}} e^{-\frac{\mathcal{H}}{k_B T}}}{\int_{\Gamma} e^{-\frac{\mathcal{H}}{k_B T}}} = 2 \left\langle \frac{\partial \mathcal{H}}{\partial \mathbf{C}} \right\rangle, \quad (4.19)$$

whereas the ensemble average may be replaced by a time average

$$\left\langle \frac{\partial \mathcal{H}}{\partial \mathbf{C}} \right\rangle = \overline{\frac{\partial \mathcal{H}}{\partial \mathbf{C}}}. \quad (4.20)$$

An expression for \mathbf{S}^{int} can already be found in equation 4.8.

The isothermal elastic constants are found by the second derivative of the Helmholtz free energy with respect to $1/2 \mathbf{C}$

$$\begin{aligned} \Omega_0 \mathbb{C} &= 4 \frac{\partial \Psi}{\partial \mathbf{C} \partial \mathbf{C}} \\ &= 2 \frac{\partial}{\partial \mathbf{C}} \left(-2 k_B T Z^{-1} \frac{\partial Z}{\partial \mathbf{C}} \right) \\ &= 2 \left(2 k_B T Z^{-2} \frac{\partial Z}{\partial \mathbf{C}} \frac{\partial Z}{\partial \mathbf{C}} - 2 k_B T Z^{-1} \frac{\partial^2 Z}{\partial \mathbf{C}^2} \right). \end{aligned} \quad (4.21)$$

The first derivative of the partition function Z with respect to \mathbf{C} is already evaluated in equation 4.19. Using this relation, the second derivative is found as

$$\begin{aligned} \frac{\partial^2 Z}{\partial \mathbf{C}^2} &= \frac{\partial}{\partial \mathbf{C}} \left(\frac{\partial Z}{\partial \mathbf{C}} \right) \\ &= \frac{1}{k_B T} \frac{\partial}{\partial \mathbf{C}} \left(- \int_{\Gamma} \frac{\partial \mathcal{H}}{\partial \mathbf{C}} e^{-\frac{\mathcal{H}}{k_B T}} d\Gamma \right) \\ &= - \frac{1}{k_B T} \int_{\Gamma} \left(\frac{\partial^2 \mathcal{H}}{\partial \mathbf{C}^2} e^{-\frac{\mathcal{H}}{k_B T}} - \frac{\partial \mathcal{H}}{\partial \mathbf{C}} \frac{1}{k_B T} e^{-\frac{\mathcal{H}}{k_B T}} \frac{\partial \mathcal{H}}{\partial \mathbf{C}} \right) d\Gamma \\ &= - \frac{Z}{k_B T} \left\langle \frac{\partial^2 \mathcal{H}}{\partial \mathbf{C}^2} \right\rangle + \frac{Z}{k_B^2 T^2} \left\langle \frac{\partial \mathcal{H}}{\partial \mathbf{C}} \frac{\partial \mathcal{H}}{\partial \mathbf{C}} \right\rangle. \end{aligned} \quad (4.22)$$

Inserting these results into equation 4.21 yields

$$\begin{aligned} \Omega_0 \mathbb{C} &= 4 \left(\frac{1}{k_B T} \left\langle \frac{\partial \mathcal{H}}{\partial \mathbf{C}} \right\rangle \left\langle \frac{\partial \mathcal{H}}{\partial \mathbf{C}} \right\rangle + \left\langle \frac{\partial^2 \mathcal{H}}{\partial \mathbf{C}^2} \right\rangle - \frac{1}{k_B T} \left\langle \frac{\partial \mathcal{H}}{\partial \mathbf{C}} \frac{\partial \mathcal{H}}{\partial \mathbf{C}} \right\rangle \right) \\ &= 4 \left[\left\langle \frac{\partial^2 \mathcal{H}}{\partial \mathbf{C}^2} \right\rangle - \frac{1}{k_B T} \left(\left\langle \frac{\partial \mathcal{H}}{\partial \mathbf{C}} \frac{\partial \mathcal{H}}{\partial \mathbf{C}} \right\rangle - \left\langle \frac{\partial \mathcal{H}}{\partial \mathbf{C}} \right\rangle \left\langle \frac{\partial \mathcal{H}}{\partial \mathbf{C}} \right\rangle \right) \right]. \end{aligned} \quad (4.23)$$

It is important to note that computation of the last two terms in equation 4.23 needs averaging over a large amount of micro-timesteps to reach a satisfying accuracy. We will see in chapter 5 that we are interested in keeping the amount of timesteps on the microscale as small as possible, in order to ensure reasonable computational cost. Therefore these terms will be neglected, i.e.

$$\Omega_0 \mathbb{C} \approx 4 \left\langle \frac{\partial^2 \mathcal{H}}{\partial \mathbf{C}^2} \right\rangle. \quad (4.24)$$

Depending on the used material and the temperature level this simplification affects the calculation in a different magnitude. Fortunately, for the materials and temperatures used in this thesis, these terms only contribute 3 – 5% to the elasticity tensor \mathbb{C} (Çağın and Pettitt (1989)). Due to thermal fluctuations, the obtained values for the elasticity tensor \mathbb{C} and the stresses \mathbf{S}^{int} can be seen as noise-corrupted measures of the ‘correct’ quantities. Even if we assume this noise could be canceled out, the method would have an inherent error of 3 – 5% in \mathbb{C} based on the assumptions presented above. In this situation, the Newton-Raphson algorithm would still converge relatively fast, although losing its quadratic convergence behavior. However, the noise cannot be canceled and negates a classic convergence behavior.

This problem corresponds to the challenging task of finding roots of noise-corrupted functions which is addressed in stochastic approximation (SA). The basics of SA are described in chapter 6.

This discussion already gave insight into some of the characteristics of the two-scale model subject of this work. This model will be further described in the next chapter.

⁵As the calculation of this derivative is rather space-consuming, it will not be part of this work, nor will the result. Please see the appendix of Ulz (2015) for further information.

Chapter 5

Two-scale Model

The scope of this thesis is to improve the information exchange of a two-scale model which consists of a macro- and a microscale. As a result, a hierarchical¹ model suitable for isothermal problems, which fits in the heterogeneous multiscale method (HMM) framework (E et al. (2007)), is obtained. The basics of the macroscale, on which the equations of continuum mechanics are solved using a displacement-based, non-linear finite element formulation, were presented in chapter 2 and 3. The Newton-Raphson method presented in section 3.2.3 is used as the macroscopic solver. The purpose of the microscale was already revealed in remark 2.5.1, where we mentioned that the microscale replaces the macroscopic material description and gives the stress response and constitutive behavior using molecular dynamics simulation.

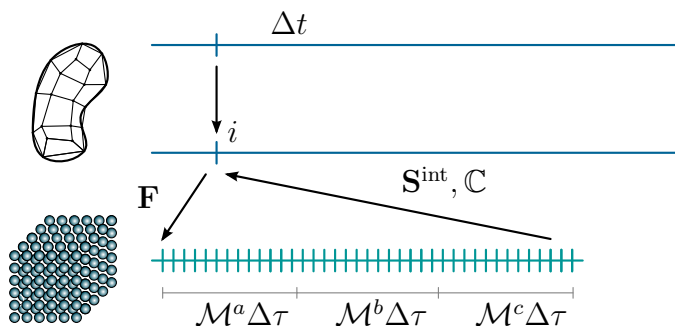


Figure 5.1: Information exchange between macro- and microscale.

The connection between macro- and microscale is sketched in figure 5.1 and can be described as follows. Every time a new displacement field is obtained on the macroscale, the deformation gradient is subsequently computed in every integration point using equation 3.6. A single MD cell is assigned to each of these integration points as sketched in figure 5.2 (PBC are used to simulate bulk material).

Each MD cell is constrained by its associated deformation gradient and the

¹For further information see Tadmor and Miller (2011, Chapter 11)

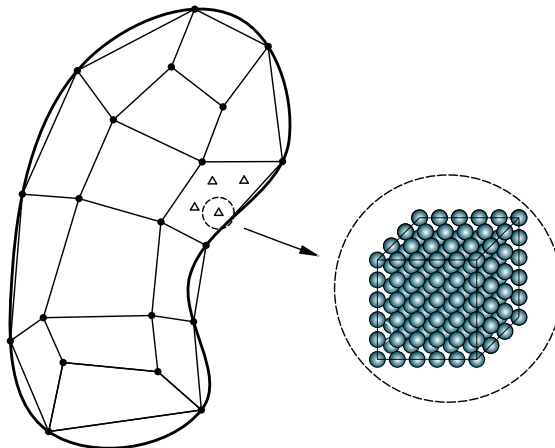


Figure 5.2: An MD cell is located at each integration point of the macroscopic body.

constant temperature T_∞ .² Therefore the *NFT* ensemble is chosen. After initialization, the MD cell is traced for a total of $\mathcal{M} = \mathcal{M}^a + \mathcal{M}^b + \mathcal{M}^c$ timesteps, which consist of three phases. The first phase uses \mathcal{M}^a timesteps to gradually load the cell with the deformation gradient \mathbf{F} . After completion, the cell is traced for $\mathcal{M}^b + \mathcal{M}^c$ timesteps under the full load of \mathbf{F} . Phases *b* and *c* are therefore similar except that the data for time averaging is only collected in phase *c*. After the averaged values of the stresses and elastic constants are calculated from the collected data, the macroscopic solver uses these quantities to compute a new displacement field and the procedure starts over.³

In section 3.2.3 it was mentioned that the Newton-Raphson method is carried out until some convergence criteria is met. In our case though, thermal fluctuations of the atoms on the microscale prevent classical convergence behavior. This means that in every macroscopic timestep, a predefined number of iterations i_{max} is performed.

It is reasonable to assume that each of these NR iterations, $i = 1, 2, 3, \dots, i_{max}$, is performed using the same number of microscopic timesteps \mathcal{M} , where \mathcal{M} is chosen to be large enough so that equilibrium is established on the microscale in every iteration (see figure 5.3).

This would indeed be desirable but is highly impracticable due to the fact that most macroscopic bodies are discretized using hundreds or thousands of elements and therefore yield at least as much integration points with their corresponding MD cells. The parallel computation of that many MD cells, to a degree where equilibrium is guaranteed in every NR iteration, yields tremendous computational

²The MD simulation gives the stresses and the elastic tensor. It is important to make a distinction between adiabatic and isothermal elastic constants. While the former are associated with rapid loading, the latter are associated with slow or quasi-static loading. Therefore we are interested in maintaining a constant temperature in the system.

³In this work, we split the total amount of microscopic timesteps per NR iteration \mathcal{M} into three uniformly distributed phases $\mathcal{M}^a = \mathcal{M}^b = \mathcal{M}^c = \mathcal{M}/3$.

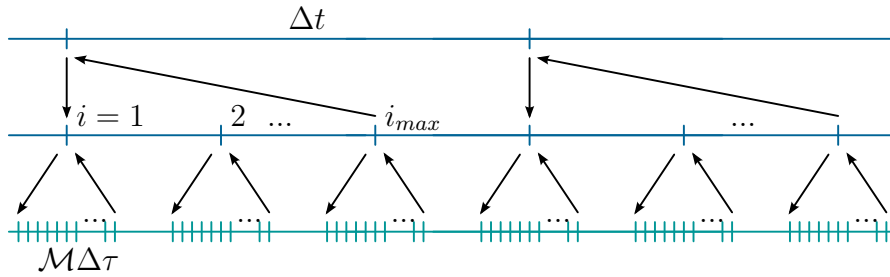


Figure 5.3: Macroscopic and microscopic time lines of the described two-scale model with time t on the macroscale and time τ on the microscale. Every Newton-Raphson iteration uses the same amount of microscopic timesteps \mathcal{M} . Figure taken from [Ulz \(2015\)](#).

cost. This computational cost can be lessened in two ways: either the amount of elements and integration points is lowered, and of course, one should always be interested in rendering the amount of elements to a minimum, or the number of timesteps on the microscale is reduced. The latter was performed in the work of [Ulz \(2015\)](#). It was shown that using only a small amount of microsteps in the first iterations and only letting the microscale reach equilibrium in the very last iteration does not mean any loss in accuracy but yields considerable computational savings. The associated scheme is shown in figure 5.4.

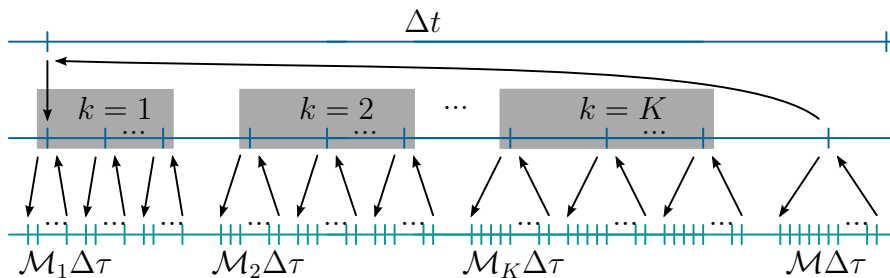


Figure 5.4: Macroscopic and microscopic time lines of the described two-scale model. As proposed in the work of [Ulz \(2015\)](#), the number of microscopic timesteps is chosen to be small in the first iterations and is increased to \mathcal{M} in the final iteration i_{max} . Figure taken from [Ulz \(2015\)](#).

While the basic idea is adopted in this work, the amount of microscopic timesteps per NR iteration is adapted to meet certain assumptions used in the stochastic approximation (SA) method. This is further discussed in chapter 7, where the equations of macro- and microscale are combined. These resulting equations exhibit strong similarities to stochastic approximation schemes. Therefore, a brief introduction to SA will be given in the next chapter.

Chapter 6

Stochastic Approximation

The basis for the following sections were the books of [Spall \(2003\)](#) and [Kushner and Yin \(2003\)](#).

Stochastic approximation addresses the problem of finding roots or extrema of noisy functions. In contrast to recursive methods used in classical numerical analysis (e.g. the Newton-Raphson method), the function itself, $\mathbf{g}(\boldsymbol{\theta})$, is not known, but noisy measurements are available at any desired value of $\boldsymbol{\theta}$ ([Kushner and Yin, 2003](#)).

Stochastic approximation methods are used in different areas in science and economics. A lot of focus is laid on machine learning algorithms ([Benaim, 1993](#); [Cheng and Titterton, 1994](#); [López-Rubio and Luque-Baena, 2011](#)). But there are also fields of application in classical engineering, e.g. in the optimization of shape designs ([El Alem et al., 2011](#); [Seyedpoor et al., 2011](#)), for estimating the thermal conductivity in boreholes ([Wen-Long et al., 2012](#)) or damping approximation ([Sultan, 2010](#)).

Two prototypical algorithms are presented in the literature. The Robbins-Monro algorithm for root finding problems, and the Kiefer-Wolfowitz algorithm for extremum problems. [Robbins and Monro \(1951\)](#) proposed the recursive scheme

$$\boldsymbol{\theta}_{n+1} = \boldsymbol{\theta}_n + \varepsilon_n \mathbf{Y}_n, \quad (6.1)$$

where $\{\varepsilon_n > 0\}$ is an appropriate gain sequence which eventually goes to zero and $\mathbf{Y}_n = \mathbf{Y}(\boldsymbol{\theta}_n)$ is a noisy measurement of $\mathbf{g}(\boldsymbol{\theta}_n)$. As ε_n goes to zero, the rate of change in $\boldsymbol{\theta}$ slows down accordingly.

While in this form, the scheme aims for finding a root $\boldsymbol{\theta}^*$ to the function $\mathbf{g}(\boldsymbol{\theta}) = \mathbf{0}$ using its measurements \mathbf{Y} , an alternative form for finding a root $\boldsymbol{\theta}^*$ of a function $\mathbf{g}(\boldsymbol{\theta}) - \boldsymbol{\alpha} = \mathbf{0}$ can easily be found as

$$\boldsymbol{\theta}_{n+1} = \boldsymbol{\theta}_n + \varepsilon_n (\boldsymbol{\alpha} - \mathbf{Y}_n). \quad (6.2)$$

In any form, the measurement \mathbf{Y}_n can be written as

$$\mathbf{Y}_n = \mathbf{g}(\boldsymbol{\theta}_n) + \mathbf{e}_k(\boldsymbol{\theta}_n), \quad (6.3)$$

if the noise term \mathbf{e}_k is dependent on $\boldsymbol{\theta}_n$. Slight variations of Eq. 6.3 are possible, e.g. if the noise is also correlated to $\{\boldsymbol{\theta}_i, i \leq n\}$. Next to correlated noise, there are also many applications where one observes measurements of the form

$$\mathbf{Y}_n = \mathbf{g}(\boldsymbol{\theta}_n) + \delta\mathbf{M}_n \quad (6.4)$$

where $\delta\mathbf{M}_n$ represents a martingale difference noise with the property $E[\delta\mathbf{M}_n | \mathbf{Y}_i, \delta M_i, i < n] = 0$. One must be aware, that $\{\varepsilon_n\}$ is required to meet additional conditions and its choice has a great influence on the efficiency of the scheme. For further information see e.g. Kushner and Yin (2003); Spall (2003).

In case of an extremum problem, for example the search of a minimum $\boldsymbol{\theta}^*$ of $L(\boldsymbol{\theta})$, the corresponding set of equations reads as:

$$\mathbf{g}(\boldsymbol{\theta}) = \frac{\partial L}{\partial \boldsymbol{\theta}} = \mathbf{0}. \quad (6.5)$$

Of course, this requires proper conditions to ensure that a root of Eq. 6.5 is a minimum. If direct measurements of the noisy derivatives $\mathbf{g}(\boldsymbol{\theta})$ are available, the associated solving algorithms are so called stochastic gradient methods. However, if only noisy measurements of $L(\boldsymbol{\theta})$ are available, the gradients can only be estimated, e.g. via finite differences using the noisy measurements Y . This method is the so called Kiefer-Wolfowitz algorithm (Kiefer and Wolfowitz, 1952):

$$\boldsymbol{\theta}_{n+1} = \boldsymbol{\theta}_n - \varepsilon_n \widehat{\mathbf{g}}_n(\boldsymbol{\theta}_n), \quad (6.6)$$

where $\{\varepsilon_n\}$ is required to meet the same conditions as before, and $\widehat{\mathbf{g}}_n(\boldsymbol{\theta}_n)$ is the finite difference estimate at the iterate $\boldsymbol{\theta}_n$ which is usually either approximated one-sided or two-sided. The two-sided approximation reads as:

$$\widehat{\mathbf{g}}_n(\boldsymbol{\theta}_n) = \begin{bmatrix} \frac{Y(\boldsymbol{\theta}_n + c_n \boldsymbol{\xi}_1) - Y(\boldsymbol{\theta}_n - c_n \boldsymbol{\xi}_1)}{2c_n} \\ \dots \\ \frac{Y(\boldsymbol{\theta}_n + c_n \boldsymbol{\xi}_p) - Y(\boldsymbol{\theta}_n - c_n \boldsymbol{\xi}_p)}{2c_n} \end{bmatrix}. \quad (6.7)$$

In this scheme, $\{c_n\}$ denotes another gain sequence with similar conditions as $\{\varepsilon_n\}$ and additionally $\sum_{n=0}^{\infty} \varepsilon_n^2 / c_n^2 < \infty$. The quantity $\boldsymbol{\xi}_i$ is a vector which has the value one at its i -th place and zero in all other places.

6.1 Averaging of the Iterates

Depending on the selected values for ε_n , the sample average

$$\boldsymbol{\Theta}_n = \frac{1}{N_n} \sum_{i=n-N_n+1}^n \boldsymbol{\theta}_i \quad (6.8)$$

can be a better estimate of the desired solution $\boldsymbol{\theta}^*$ than $\boldsymbol{\theta}_n$ is. We would like to refer to this procedure as ‘offline averaging’, since it does not influence the actual stochastic approximation algorithm, but rather replaces its final estimate by an average of previous estimates. In this expression, N_n determines the window of averaging. Therefore, if an average over all samples is desired, one has to chose $N_n = n$.

It is commonly known that if ε_n approaches zero slower than $1/n$, averaging of the iterates will improve the convergence behavior. This was originally found by [Polyak and Juditsky \(1992\)](#), proof of this can be found in [Kushner and Yang \(1993\)](#). One possible choice of ε_n that fulfills this criterion is

$$\varepsilon_n = \frac{a}{a+n} \quad a > 1. \quad (6.9)$$

For further information see e.g. [Kushner and Yin \(2003\)](#); [Spall \(2003\)](#).

6.2 Averaging of the Observatives

Another way to improve the convergence behavior under certain conditions is to use averaged values of the iterates and observatives of the form

$$\tilde{\boldsymbol{\theta}}_n = \frac{1}{n} \sum_{i=1}^n \boldsymbol{\theta}_i \quad \tilde{\mathbf{Y}}_n = \frac{1}{n} \sum_{i=1}^n \mathbf{Y}_i. \quad (6.10)$$

As this influences the stochastic approximation algorithm, which now reads as

$$\boldsymbol{\theta}_{n+1} = \tilde{\boldsymbol{\theta}}_n + \varepsilon_n \tilde{\mathbf{Y}}_n, \quad (6.11)$$

we would like to refer to this procedure as ‘online averaging’.

Chapter 7

Application of SA to FEM/MD

Let us assume a minor change to the iteration scheme shown in figure 5.4. We want to adapt the iteration scheme so that there are no more groups $k = 1, 2, 3, \dots, K$ which consist of iterations with equal amount of timesteps, but rather increase the amount of microsteps gradually from iteration to iteration as shown in figure 7.1.

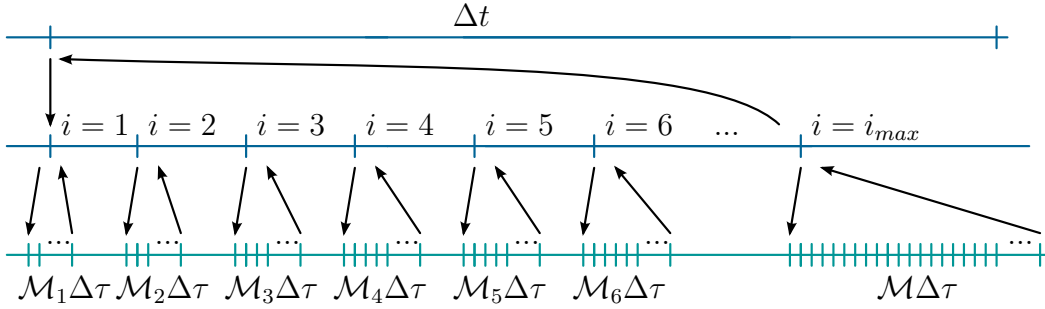


Figure 7.1: Macroscopic and microscopic time lines of the described two-scale model. The amount of microscopic timesteps per NR iteration is increased gradually. Figure adapted from [Ulz \(2015\)](#).

This two-scale model may be described using the equations

$$\underline{\mathbf{u}}^{(i+1)} = \underline{\mathbf{u}}^{(i)} + \left[\underline{\mathbf{K}}^{(i)}(\mathbf{S}^{\text{int}}, \mathbb{C}) \right]^{-1} \left[\underline{\mathbf{F}}_{ext} - \underline{\mathbf{F}}_{int}^{(i)}(\mathbf{S}^{\text{int}}) \right], \quad (7.1)$$

where

$$\begin{aligned} \underline{\mathbf{K}}^{(i)}(\mathbf{S}^{\text{int}}, \mathbb{C}) &= \sum_{i=1}^M \int_{V_r^{(e)}} \underline{\mathbf{B}}_L^{(e)T} \left(\frac{1}{\mathcal{M}_i^c} \sum_{j=1}^{\mathcal{M}_i^c} \underline{\mathbb{C}}_j \right)^{(e)} \underline{\mathbf{B}}_L^{(e)} \det(\mathbf{J}) dV_r^{(e)} \\ &+ \sum_{i=1}^M \int_{V_r^{(e)}} \underline{\mathbf{B}}_{NL}^{(e)T} \left(\frac{1}{\mathcal{M}_i^c} \sum_{j=1}^{\mathcal{M}_i^c} \underline{\mathbf{S}}_j^{\text{int}} \right)^{(e)} \underline{\mathbf{B}}_{NL}^{(e)} \det(\mathbf{J}) dV_r^{(e)} \end{aligned} \quad (7.2)$$

and

$$\mathbf{F}_{int}^{(i)}(\mathbf{S}^{int}) = \sum_{i=1}^M \int_{V_r^{(e)}} \mathbf{B}_{\approx L}^{(e)T} \left(\frac{1}{\mathcal{M}_i^c} \sum_{j=1}^{\mathcal{M}_i^c} \mathbf{S}_j^{int} \right)^{(e)} \det(\mathbf{J}) dV_r^{(e)}. \quad (7.3)$$

In these equations, the element volume integrals are evaluated numerically as described in section 3.1.4 and the summation over the finite elements i can be understood as an assembling process as mentioned in section 3.2.1.

The equations in 7.1 show similarities to stochastic approximation schemes of the form

$$\boldsymbol{\theta}_{n+1} = \boldsymbol{\theta}_n + \varepsilon_n(\boldsymbol{\alpha} - \mathbf{Y}_n) \quad (7.4)$$

described in chapter 6. The displacements $\mathbf{u}^{(i+1)}$ correspond to $\boldsymbol{\theta}_{n+1}$ and the previous displacement field $\mathbf{u}^{(i)}$ corresponds to $\boldsymbol{\theta}_n$.

Furthermore, in stochastic approximation we are interested in finding the values of $\boldsymbol{\theta} = \boldsymbol{\theta}^*$ which give a root of the function $\boldsymbol{\alpha} - \mathbf{g}(\boldsymbol{\theta}) = \mathbf{0}$, where $E[\mathbf{Y}_n] = \mathbf{g}(\boldsymbol{\theta})$. The same applies here, where we are interested in finding a displacement field $\mathbf{u} = \mathbf{u}^*$ which fulfills $\mathbf{F}_{ext} - \mathbf{F}_{int} = \mathbf{0}$, but only noise-corrupted values of \mathbf{S}^{int} and \mathbf{C} are available. As previously mentioned, this noise originates from the thermal fluctuations of the atoms on the microscale. The time averaging of the form $\frac{1}{\mathcal{M}_i^c} \sum_{j=1}^{\mathcal{M}_i^c} (\bullet)$ with increasing microscopic timestep amounts corresponds to the decreasing sequence $\{\varepsilon_n\}$.

In chapter 6,

$$\varepsilon_n = \frac{a}{a+n} \quad a > 1 \quad (7.5)$$

was suggested as a possible choice for this sequence, which is also suitable for offline averaging. If we choose $a = 1.1$, the microscopic timestep amounts follow the relation

$$\mathcal{M}_i = \frac{1.1+i}{1.1}. \quad (7.6)$$

This yields very small timestep amounts which lead to improper results on the microscale. Therefore, we simply introduce a factor A in the form

$$\mathcal{M}_i = \frac{1.1+i}{1.1} A. \quad (7.7)$$

which ensures reasonable results. This factor does not violate the criterion which led to equation 7.5 in section 6.1. Proof of this is straightforward and can be found in appendix C.

The similarities described above justify the use of the SA averaging concepts discussed in section 6.1 and 6.2.

7.1 Offline Averaging

At first we take a look at offline averaging. Referring to Spall (2003), two different search paths in a two-dimensional space are shown in figure 7.2.

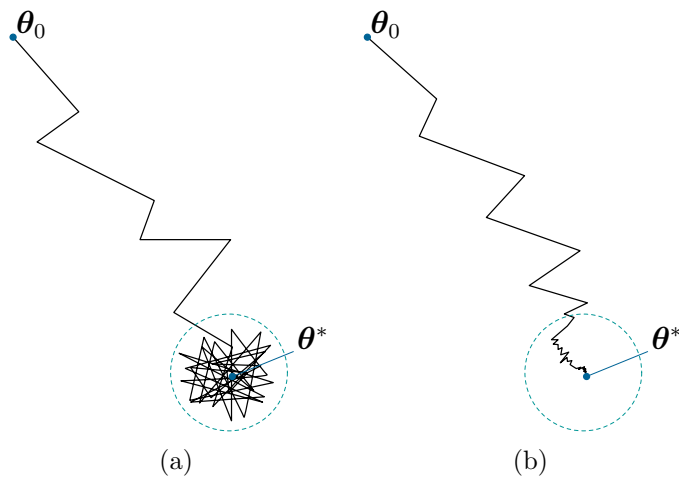


Figure 7.2: Two different scenarios of search paths in a two-dimensional SA problem. Offline averaging is expected to improve the result of the left scenario, but certainly will not improve the outcome of the right scenario. Figures taken from Spall (2003).

The two-dimensional search path can be thought of as the movement of a nodal point in a two-dimensional problem. If the nodal point shows similar behavior to figure 7.2a, i.e. it fluctuates in a small area in which we can expect the root θ^* rather than strictly approaching this point as shown in 7.2b, offline averaging will potentially improve the iteration result. In fact, we will see in chapter 8 that thermal fluctuations really cause the nodal points to behave in a similar manner as shown in figure 7.2a. This means that if offline averaging is applied, we expect to get a better estimate of the desired displacement field \underline{u}^* .

Because we are particularly interested in the stress distribution¹, an improved displacement field is only half the battle. It was shown in chapter 5, that the stresses are computed on the microscale using the deformation gradients obtained from the current displacement field. Due to the character of the microscale, the hereby obtained stresses in an arbitrarily chosen point of the body can be written as²

$$\mathbf{S} = \tilde{\mathbf{S}} + \Delta\mathbf{S}, \quad (7.8)$$

where $\tilde{\mathbf{S}}$ is the correct stress response for an arbitrary displacement field and $\Delta\mathbf{S}$ is the error which originates from the thermal fluctuation of the atoms. Even if we assume to have found the desired displacement field \underline{u}^* , the stress response obtained is

$$\mathbf{S} = \mathbf{S}^* + \Delta\mathbf{S}, \quad (7.9)$$

¹Due to their physical meaning, we are interested in obtaining the Cauchy stresses $\boldsymbol{\sigma}$. In the used FE formulation only the second Piola-Kirchhoff stresses \mathbf{S} are present. We can simply calculate the Cauchy stresses as $\boldsymbol{\sigma} = J^{-1}\mathbf{F}\mathbf{S}\mathbf{F}^T$ using equation 2.38.

² $\Delta\mathbf{S}$ should not be confused with the increment of the second Piola-Kirchhoff stresses used in section 2.5.

where \mathbf{S}^* are the correct stresses for the desired displacement field.

This means, even if offline averaging yields a displacement field arbitrarily close to the desired displacement field, the stress distribution is still containing errors and we need to adopt further measures in order to obtain an improved stress distribution. One possible measure is to reduce the magnitude of $\Delta\mathbf{S}$. This can either be done by averaging over a large amount of timesteps or by increasing the amount of atoms in the simulation. Both solutions are impracticable due to increased computational cost. Another possible way to improve the stress distribution is to introduce offline averaging of the stresses. The idea is the same as in case of the displacements, the influence of the thermal fluctuations is reduced through averaging. This does also not cause any additional computational cost.

In summary, it can be stated that one possibility which shows potential to improve the displacement field as well as the stress distribution, is represented by a combination of offline averaging of the displacements and the stresses.

7.2 Online Averaging

Next to the offline averaging, online averaging was discussed in section 6.2 as a second method to potentially improve the results of SA schemes. While offline averaging did not influence the iteration process, online averaging interferes with the SA scheme as the displacements as well as the stress response and constitutive behavior are constantly averaged. The iteration scheme of equation 7.1

$$\underline{\mathbf{u}}^{(i+1)} = \underline{\mathbf{u}}^{(i)} + \left[\underline{\mathbf{K}}^{(i)}(\mathbf{S}^{\text{int}}, \mathbb{C}) \right]^{-1} \left[\underline{\mathbf{F}}_{\text{ext}} - \underline{\mathbf{F}}_{\text{int}}^{(i)}(\mathbf{S}^{\text{int}}) \right], \quad (7.1)$$

is changed to

$$\underline{\mathbf{u}}^{(i+1)} = \underline{\tilde{\mathbf{u}}}^{(i)} + \left[\underline{\mathbf{K}}^{(i)}(\tilde{\mathbf{S}}^{\text{int}}, \tilde{\mathbb{C}}) \right]^{-1} \left[\underline{\mathbf{F}}_{\text{ext}} - \underline{\mathbf{F}}_{\text{int}}^{(i)}(\tilde{\mathbf{S}}^{\text{int}}) \right], \quad (7.10)$$

using averages of the quantities in previous NR iterations k

$$\underline{\tilde{\mathbf{u}}}^{(i)} = \frac{1}{i} \sum_{k=1}^i \underline{\tilde{\mathbf{u}}}^{(k)} \quad \tilde{\mathbf{S}}^{\text{int}} = \frac{1}{i} \sum_{k=1}^i \tilde{\mathbf{S}}^{\text{int},(k)} \quad \tilde{\mathbb{C}} = \frac{1}{i} \sum_{k=1}^i \tilde{\mathbb{C}}^{(k)}. \quad (7.11)$$

Because the stresses are already averaged during the iteration process, an additional offline averaging, as introduced in the end of the previous section, is not applied.

7.3 Online/Offline Averaging

Another method used in this work represents a combination of the previous methods. The displacement field will be subject to online averaging, whereas the stresses

7.3. ONLINE/OFFLINE AVERAGING

and the constitutional behavior are not averaged during the iteration process. The iteration scheme for this method reads as

$$\tilde{\mathbf{u}}^{(i+1)} = \tilde{\mathbf{u}}^{(i)} + \tilde{\mathbf{K}}^{(i)}(\mathbf{S}^{\text{int}}, \mathbb{C})^{-1} \left[\tilde{\mathbf{F}}_{\text{ext}} - \tilde{\mathbf{F}}_{\text{int}}^{(i)}(\mathbf{S}^{\text{int}}) \right]. \quad (7.12)$$

Again, even if this method yields an accurate displacement field, additional offline averaging of the stresses needs to be applied as discussed in section [7.1](#).

Chapter 8

Numerical Examples

In this chapter, the three strategies presented at the end of the last chapter will be compared by applying them on two numerical examples. We will get insight in the averaging behavior by looking at how the displacements and stresses evolve over the NR iterations and we will further compare the resulting stress distributions. It was already mentioned that additional offline averaging of the stresses may further improve the results of the strategies presented in section 7.1 and 7.3. To verify this assumption, we will therefore also compare the results with and without additional offline stress averaging.

Table 8.1 shows the three different comparison scenarios. To facilitate readability, we introduce the parenthesized abbreviations.¹

1	Offline averaging of the displacements (<i>off:u</i>)	vs.	Offline averaging of the displacements + additional offline averaging of the stresses (<i>off:uS</i>)
2	Offline averaging of the displacements (<i>off:u</i>)	vs.	Online averaging (<i>on:uSC</i>)
3	Online averaging of the displacements (<i>on:u</i>)	vs.	Online averaging of the displacements + additional offline averaging of the stresses (<i>on:u;off:S</i>)

Table 8.1: Compared methods.

It was mentioned in the discussion of the two-scale model in chapter 5, that the amount of microscopic timesteps in the very last NR iteration should be chosen

¹It is important to note that both online averaging methods (*on:u* and *on:uSC*) are first applied after the third NR iterate. This is because the macroscopic observables of MD simulations generally show large deflections in the first few iterations, which we want to exclude from the online averaging procedure.

large enough to ensure equilibrium on the microscale. It is important to note that we will refrain from this approach due to high computational cost.

In the first example, a plate with a circular notch under uniaxial tension is investigated, whereas the second example is concerned with an elastic half-plane under line load. While the material used in the first example is a copper single crystal, the second one uses a tungsten single crystal.² In both examples, the temperature is 300K and the lattice planes are parallel to the boundary planes in the undeformed configuration of the two macroscopic regions. The geometry is discretized using a FEM mesh with linear triangular elements as presented in section 3.1.2. For these elements, only one integration point per element is needed to achieve reasonable results.³

8.1 Plate with circular Notch under uniaxial Tension

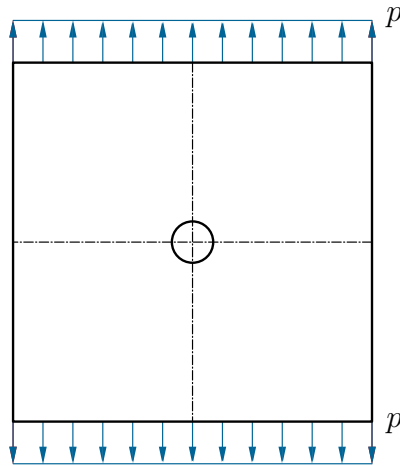


Figure 8.1: Plate with circular notch under uniaxial tension.

A plate with dimensions 723x723x1nm and a central circular notch of radius 21.69nm is considered as shown in figure 8.1. The plate is loaded with $p = 0.667\text{GPa}$. Due to the symmetrical properties of the problem, only a quarter will be investigated to avoid unnecessary computational cost. A quarter of the system is sketched in figure 8.2a. The boundary conditions are chosen accordingly. As the stress gradients in close distance to the notch are assumed to be much higher than on the outer edges, the element sizing is adapted appropriately, resulting in a total amount of 546 elements (see figure 8.2b). The load is applied

²We use a different material in the second example to overcome certain disadvantages arising from the stress distribution of this example. This will be further discussed in section 8.2.

³For the required order of numerical integration for different elements see e.g. [Zienkiewicz and Taylor \(2000\)](#).

in a single macroscopic timestep, in which 70 Newton-Raphson iterations are performed. Furthermore, the timesteps on the microscale are increased according to equation 6.9 as

$$\mathcal{M}_i = \frac{a + i}{a} 50 \quad (8.1)$$

with $a = 1.1$.

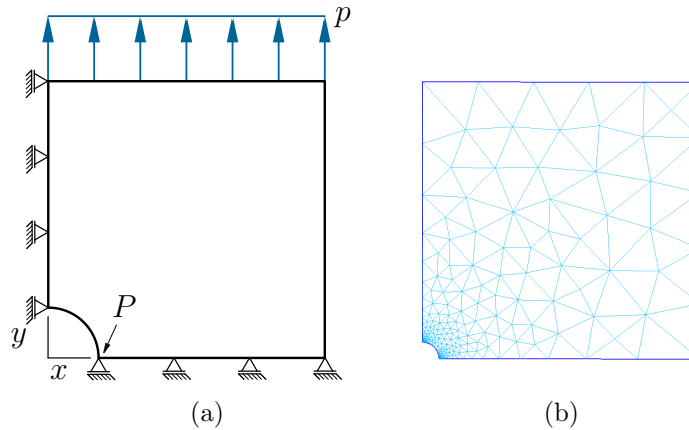


Figure 8.2: Modeled system, boundary conditions and FEM mesh.

8.1.1 Comparison of the averaging behavior

In order to gain insight in the averaging behavior of the proposed strategies, we take a look at the displacements and stresses at a characteristic point in the macroscopic domain.⁴ We chose point P for this purpose (see figure 8.2a).

In section 7.1 we mentioned that offline averaging is expected to improve the final estimate of the displacement field if the nodal points' motion over the iterates shows similar behavior to figure 7.2a. In this figure, a two-dimensional search path was shown. Because P only holds one degree of freedom, it is unsuitable for comparison. We will therefore select another characteristic point Q , located at $(x = 1.0169\text{nm}; y = 25.95\text{nm})$ in the undeformed configuration, which will move along a two-dimensional path.

Displacement field

At first we take a look at the evolution of the displacement of point P in x -direction over the NR iterates. The displacement fields for $off:u$ and $off:uS$ as well as for $on:u$ and $on:u;off:S$ coincide⁵, which only leaves three different curves as shown in figure 8.3.

⁴A point is characteristic if it reflects the behavior of most other points and hence allows to draw conclusions which apply to the majority of all points.

⁵This is because offline averaging of the stress distribution does not influence the displacement field.

8.1. PLATE WITH CIRCULAR NOTCH UNDER UNIAXIAL TENSION

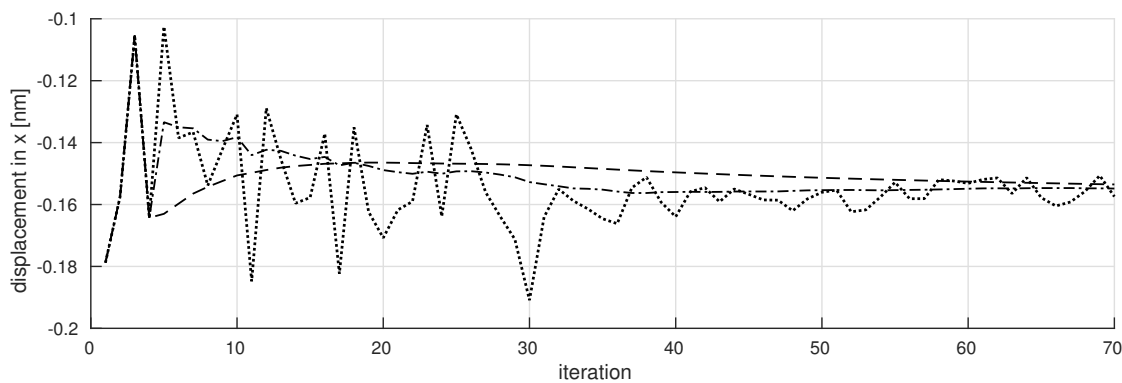


Figure 8.3: Displacement of point P over the iterates. The dotted, dashed and dot-dashed lines show the results for $off:u/off:uS$, $on:uSC$ and $on:u/on:u;off:S$, respectively.

The displacements obtained by $off:u$ exhibit much smaller fluctuations after 35 iterations, and $on:u$ seems to directly adopt this behavior resulting in a relatively horizontal line. Naturally, both online averaging schemes produce smoother curves, although in this example, the displacements seem to converge faster using $on:u$ rather than $on:uSC$.

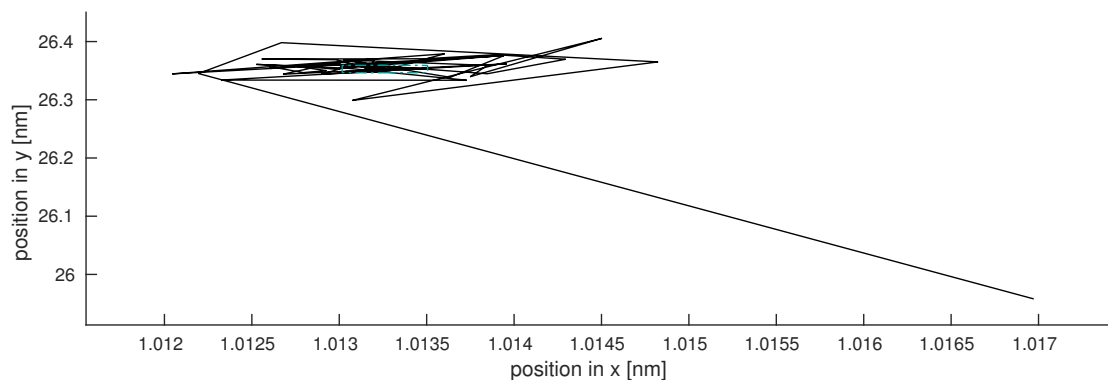


Figure 8.4: Position of point Q over the iterates. An enlarged view of the area that contains the last 20 iterations is shown in figure 8.5.

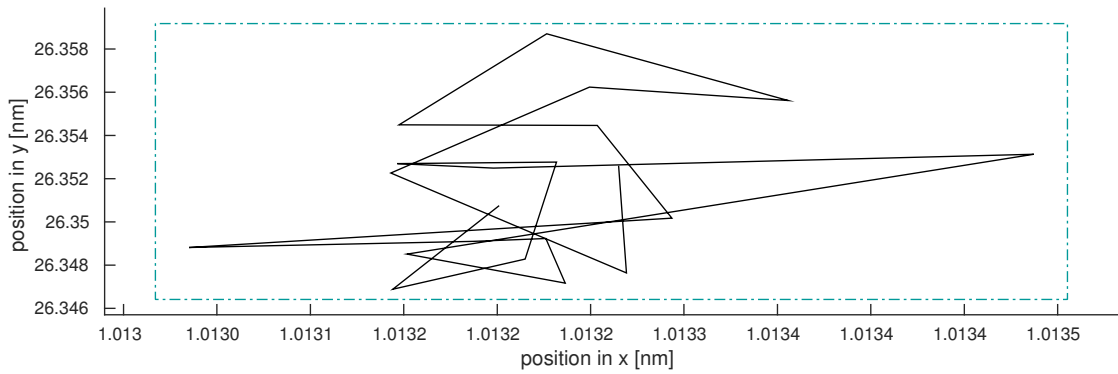


Figure 8.5: Position of point Q over the last 20 iterates. To facilitate orientation please consider the x - and y -scale in relation to figure 8.4. The area is clearly limited to a small domain.

In figure 8.4 and 8.5, the two-dimensional search path of a characteristic point Q is shown. The comparison with figure 7.2a shows that the assumptions made in section 7.1 apply and therefore offline averaging is expected to improve the displacement field.

Stress field

Next, we investigate the iterative behavior of the normal stress σ_{xx} at point P as shown in figure 8.6. It is important to note that in contrast to the displacements, where the displacement fields of $off:u$ and $off:uS$ as well as those of $on:u$ and $on:u;off:S$ coincided, their stress distributions only coincide until the next-to-last iteration. In the last iteration, offline stress averaging replaces the final estimate of the stress values with the averaged values as shown in figure 8.7.

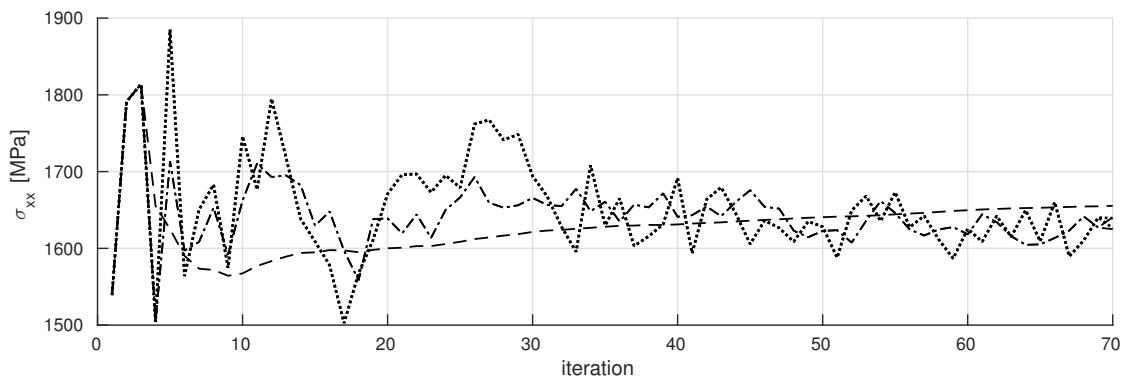


Figure 8.6: Normal stress σ_{xx} at point P over the iterates. The dotted, dashed and dot-dashed lines show the results for $off:u/off:uS$, $on:uSC$ and $on:u/on:u;off:S$ respectively.

The stress value obtained through $on:uSC$ shows increasing behavior over the iterates and the final estimate is obtained to be too high.

8.1. PLATE WITH CIRCULAR NOTCH UNDER UNIAXIAL TENSION

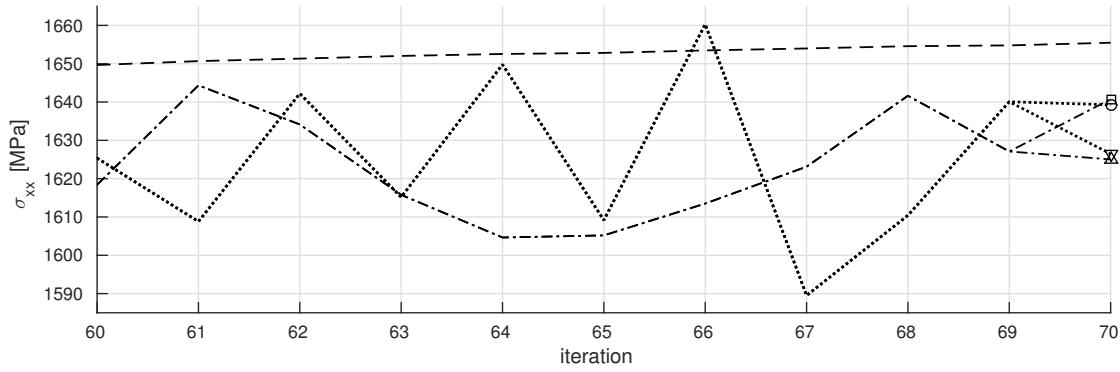


Figure 8.7: Normal stress σ_{xx} at point P over the last 10 iterates. The final stress estimate for the different strategies is marked using the following symbols:

○: *off:u* ▽: *off:uS* □: *on:u* △: *on:u;off:S*.

8.1.2 Comparison of the stress distributions

While the preceding discussion provided an insight in the behavior of the proposed averaging schemes, we will now compare the final estimates of the stress distributions for the cases 1, 2 and 3 which were presented in table 8.1. Therefore, the normalized normal stresses σ_{xx}/p and σ_{yy}/p along the x- and y-axis are plotted in figure 8.8 to figure 8.11. The analytical solution taken from Lekhnitskii (1968) (elastic constants for this solution taken from Lazarus (1949) for copper) is given by a solid line in all of these figures.

The stress distributions show good overall agreement to the analytical solution, which implies that the used two-scale model combined with the proposed averaging schemes is appropriate for this example. Furthermore, the additional offline stress averaging used in *off:uS* and *on:u;off:S* improves the results compared to their non-stress-averaging counterparts.

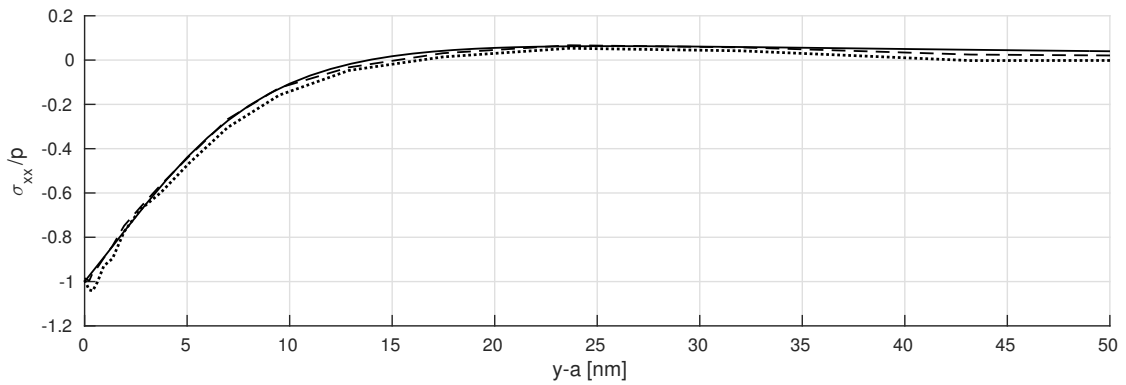
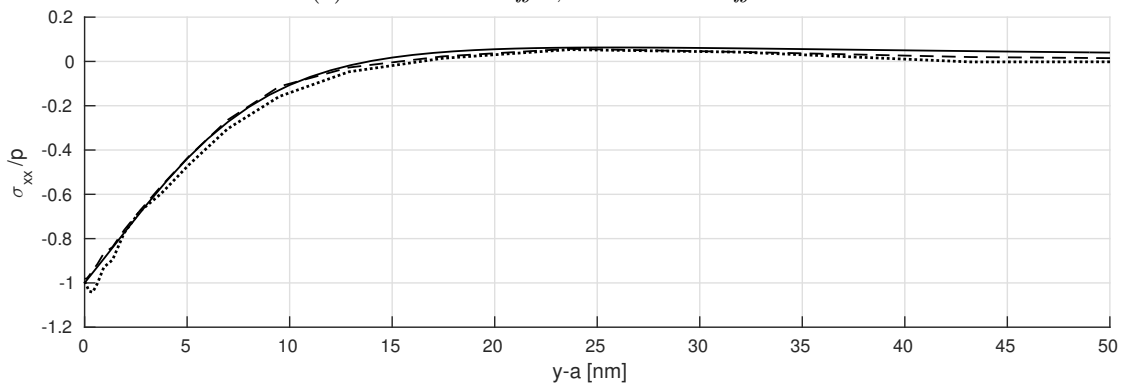
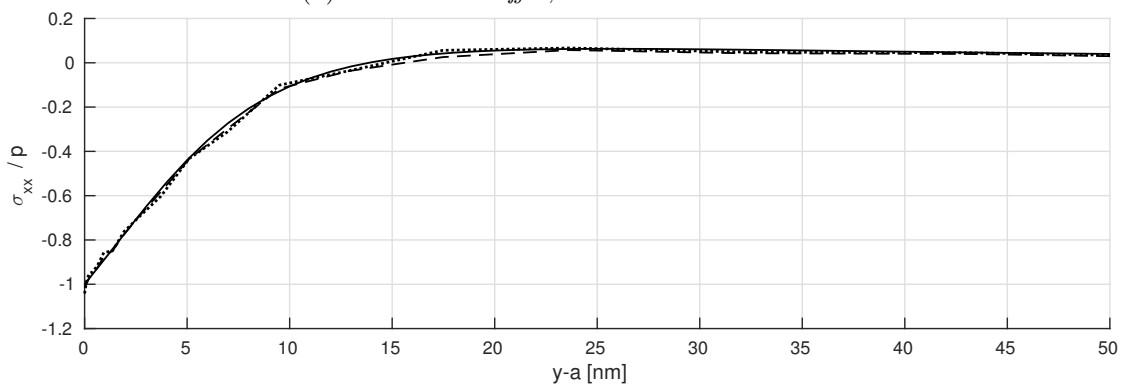
(a) Dotted line: *off:u*, dashed line: *off:uS*.(b) Dotted line: *off:u*, dashed line: *on:uSC*.(c) Dotted line: *on:u*, dashed line: *on:u;off:S*.

Figure 8.8: Normalized normal stress σ_{xx} along the y -axis. The curves in (a),(b) and (c) correspond to the cases 1,2 and 3, presented in table 8.1, respectively. The analytical solution is given according to [Lekhnitskii \(1968\)](#) as a solid line.

8.1. PLATE WITH CIRCULAR NOTCH UNDER UNIAXIAL TENSION

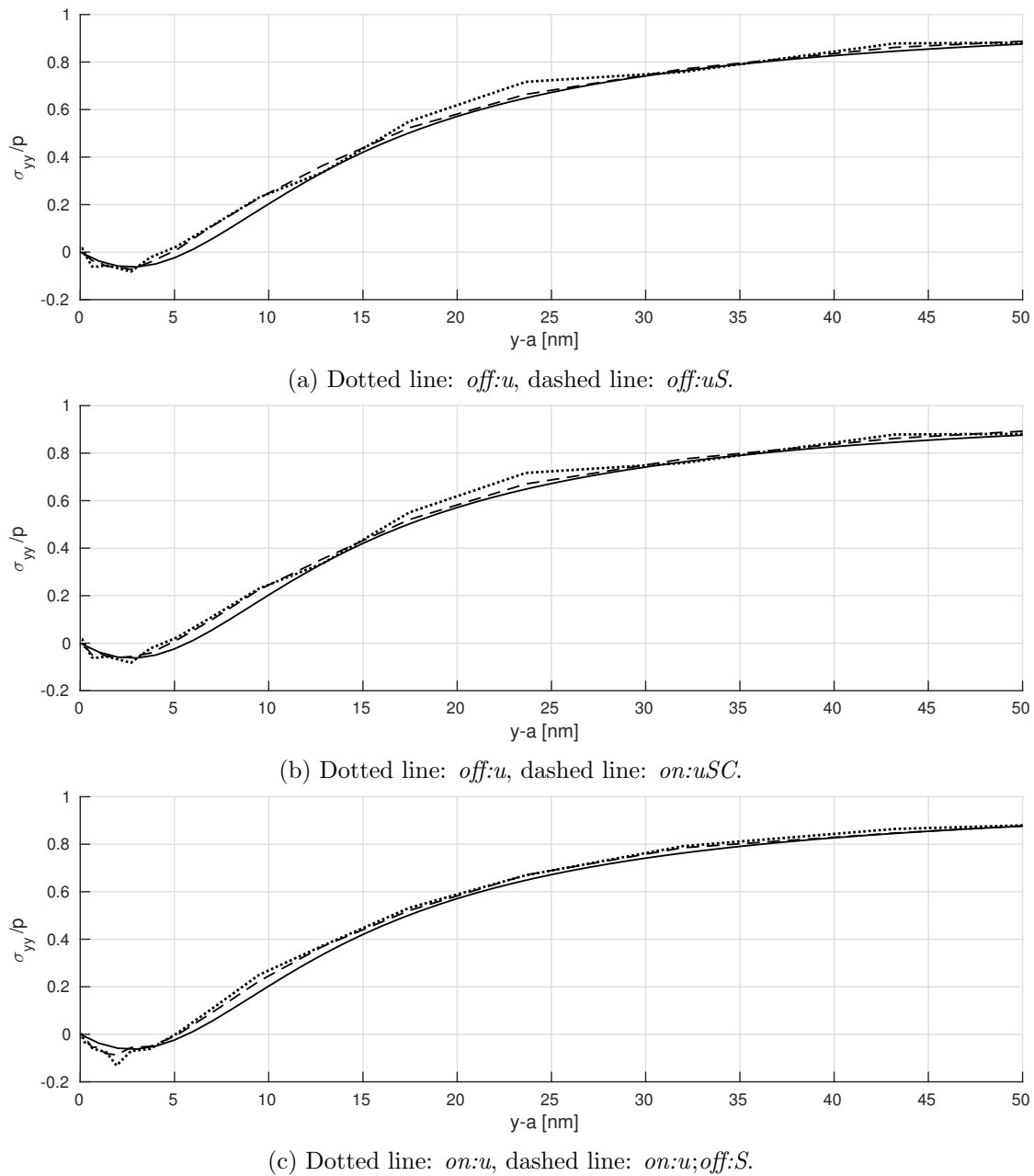
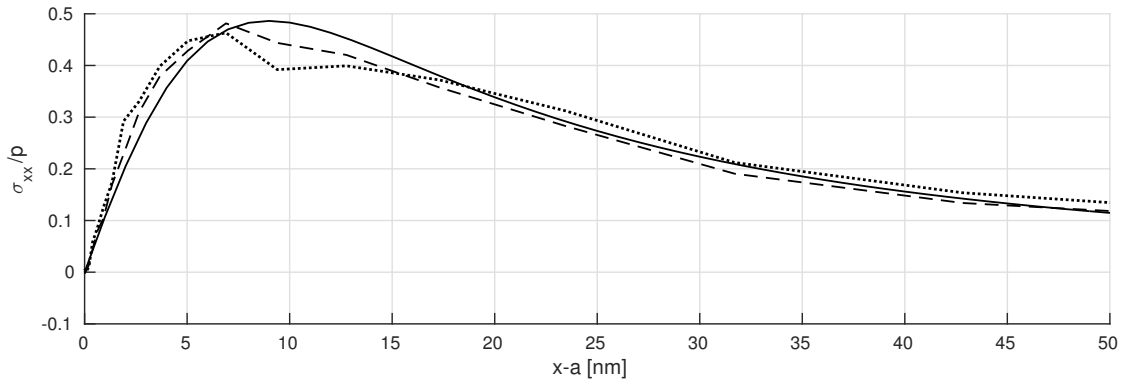
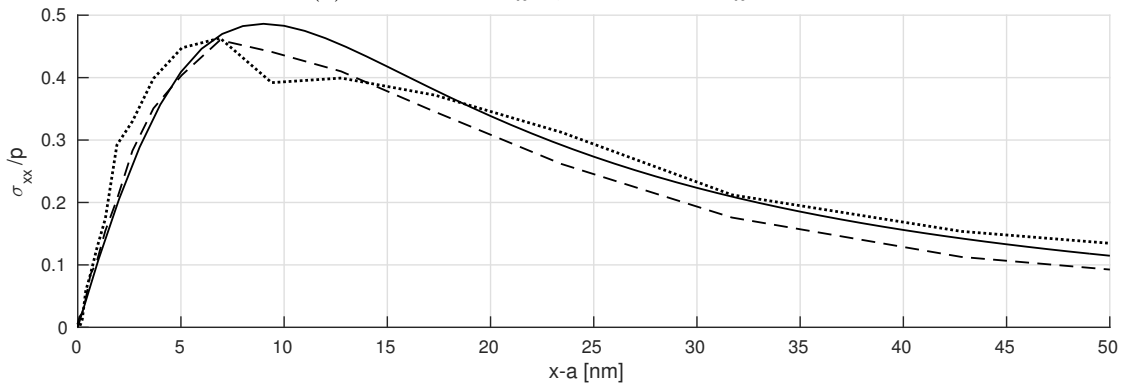


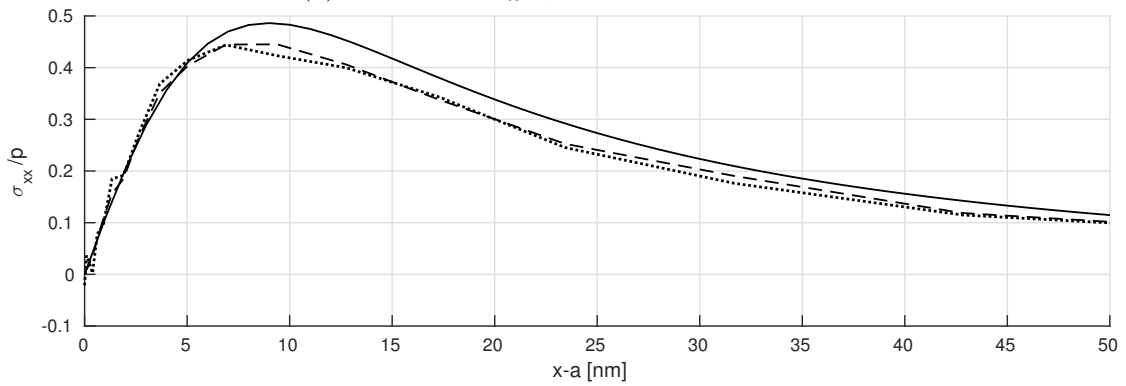
Figure 8.9: Normalized normal stress σ_{yy} along the y -axis. The curves in (a),(b) and (c) correspond to the cases 1,2 and 3, presented in table 8.1, respectively. The analytical solution is given according to Lekhnitskii (1968) as a solid line.



(a) Dotted line: *off:u*, dashed line: *off:uS*.



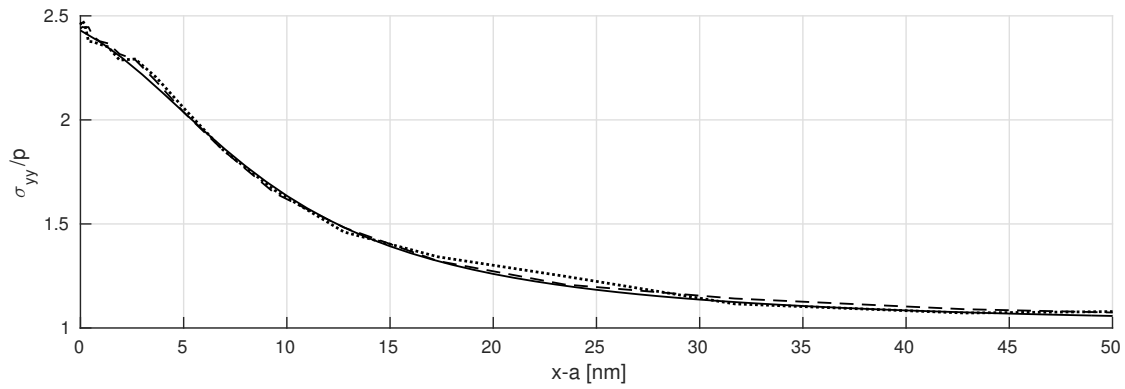
(b) Dotted line: *off:u*, dashed line: *on:uSC*.



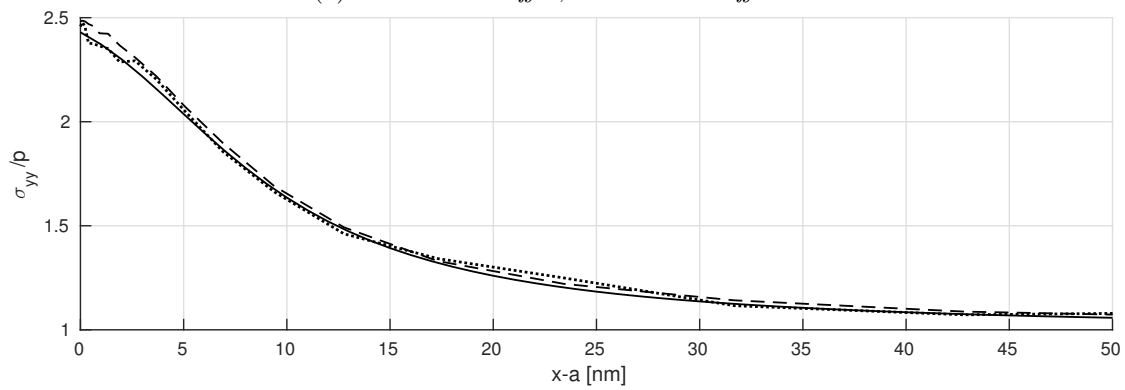
(c) Dotted line: *on:u*, dashed line: *on:u;off:S*.

Figure 8.10: Normalized normal stress σ_{xx} along the x-axis. The curves in (a),(b) and (c) correspond to the cases 1,2 and 3, presented in table 8.1, respectively. The analytical solution is given according to Lekhnitskii (1968) as a solid line. The significant discrepancy between the numerical and analytical solutions is due to discretization faults.

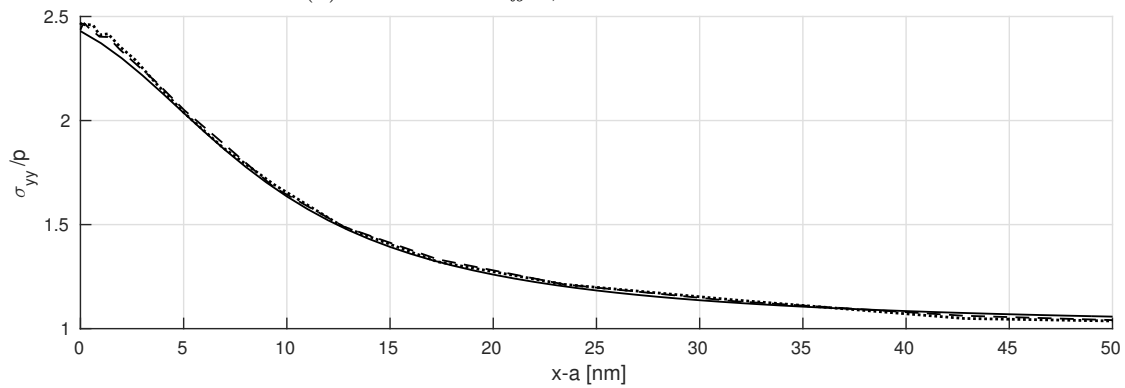
8.1. PLATE WITH CIRCULAR NOTCH UNDER UNIAXIAL TENSION



(a) Dotted line: *off:u*, dashed line: *off:uS*.



(b) Dotted line: *off:u*, dashed line: *on:uSC*.



(c) Dotted line: *on:u*, dashed line: *on:u;off:S*.

Figure 8.11: Normalized normal stress σ_{yy} along the x -axis. The curves in (a),(b) and (c) correspond to the cases 1,2 and 3, presented in table 8.1, respectively. The analytical solution is given according to [Lekhnitskii \(1968\)](#) as a solid line.

8.2 Elastic infinite Half-Plane under Line Load

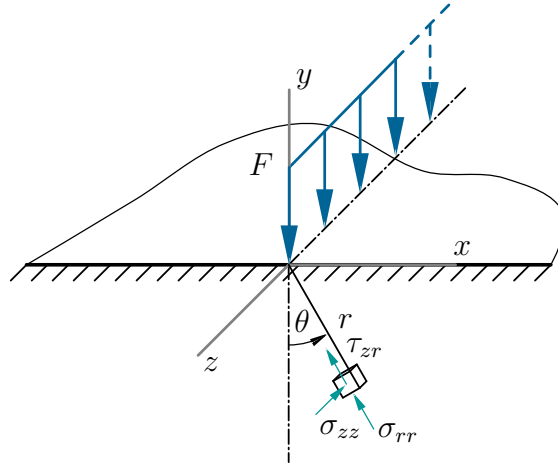


Figure 8.12: Elastic infinite half-plane under line load. Figure and stress definition taken from [Lekhnitskii \(1968\)](#).

The second numerical example is shown in figure 8.12. Uniformly distributed normal forces F are applied to the surface of an elastic infinite half-plane in a straight line. Similar to the previous example, the symmetrical properties of the problem are used to simplify the system as shown in figure 8.13a.

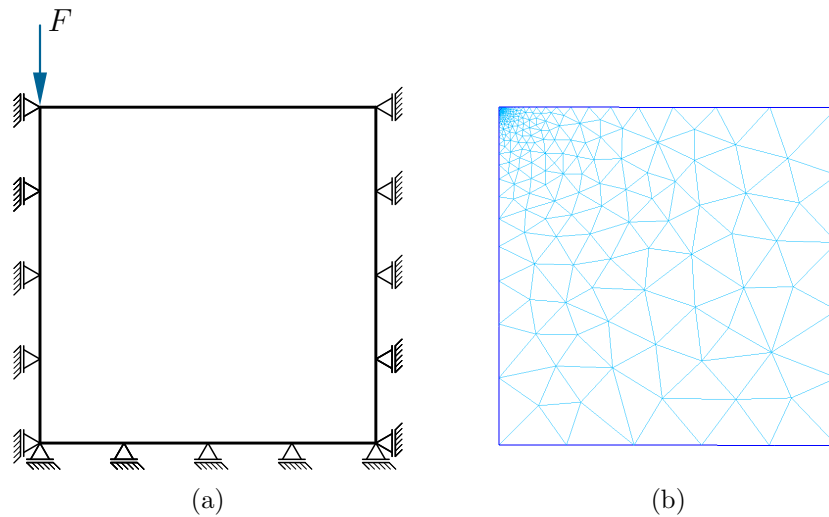


Figure 8.13: Simplified system and FEM mesh. The edge length has been chosen to be 361.5nm following the first example (section 8.1) and was verified to be large enough to deliver appropriate results.

Although the elastic half-plane spans over an infinite area, if one chooses the edge length properly with regard to the elastic properties and the applied load, the problem can also be solved correctly using a finite plate.

8.2. ELASTIC INFINITE HALF-PLANE UNDER LINE LOAD

The analytical solution taken from [Lekhnitskii \(1968\)](#) (elastic constants for tungsten taken from [Featherston and Neighbours \(1963\)](#)) shows a singularity for the normal stress σ_{rr} at the point of origin of the normal force F as shown in figure 8.14.

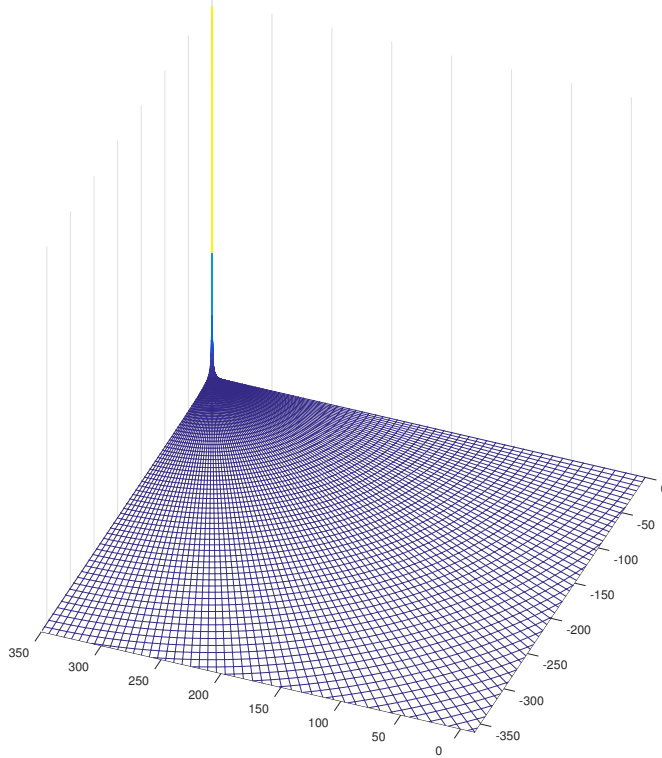


Figure 8.14: Distribution of the normal stress σ_{rr} for the elastic half-plane under line-load.

As this is associated with very high stress gradients in that specific area, a fine mesh has been chosen in close neighborhood around the upper left corner point as shown in figure 8.13b. The total amount of elements used is 536.

Due to the high stress gradients, the stress level goes down quickly to low magnitudes in close distance to the upper left corner. It was shown in equation 4.8, that the microscopic stresses are calculated using the atoms' fluctuations. These fluctuations consist of a thermal part and a potential part due to the atomic movement according to the deformation of the MD cell. Low stress levels come with low strain levels, hence also small deformation of the MD cells. If only small deformations of the cell are present, the thermal fluctuations surmount and the simulation produces incorrect results.

To overcome this problem, we could simply increase the loading, which would result in higher stress. However, for the same material, an increased stress results in increased strain, which may cause the macroscopic solver to diverge.

Another approach is to simply use a different material with larger elastic constants. This means that the load can be increased, resulting in a higher stress

level, while maintaining an appropriate level of strain. This is the main reason we chose tungsten in this example, as mentioned at the beginning of this chapter.

Similar to the first example, the load F is applied in one single macroscopic timestep which consists of 70 NR iterations. The timesteps on the microscale are also increased in the same manner, by the relation given in equation 8.1.

8.2.1 Comparison of the averaging behavior

Similar to the first example, we will compare the averaging behavior using one characteristic point in the macroscopic domain. We chose a point P located at $(x = 0\text{nm}; y = -7.328\text{nm})$. Additionally, in order to compare the search paths, we select another point Q located at $(x = 0.256\text{nm}; y = -0.06\text{nm})$.

Displacement field

The displacement of point P in y -direction over the NR iterates is plotted in figure 8.15.

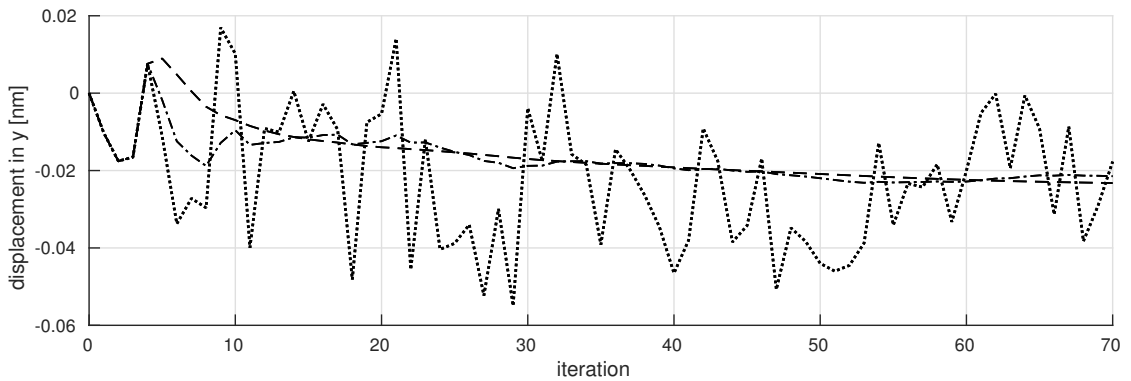


Figure 8.15: Displacement of point P over the iterates. The dotted, dashed and dot-dashed lines show the results for $off:u/off:uS$, $on:uSC$ and $on:u/on:u;off:S$ respectively.

It was already mentioned in the first example that the resulting displacement fields for $off:u$ and $off:uS$ as well as for $on:u$ and $on:u;off:S$ coincide. This time, the displacements obtained by using the online averaging schemes show similar behavior to each other and especially $on:uSC$ seems to yield better results compared to the first example.

8.2. ELASTIC INFINITE HALF-PLANE UNDER LINE LOAD

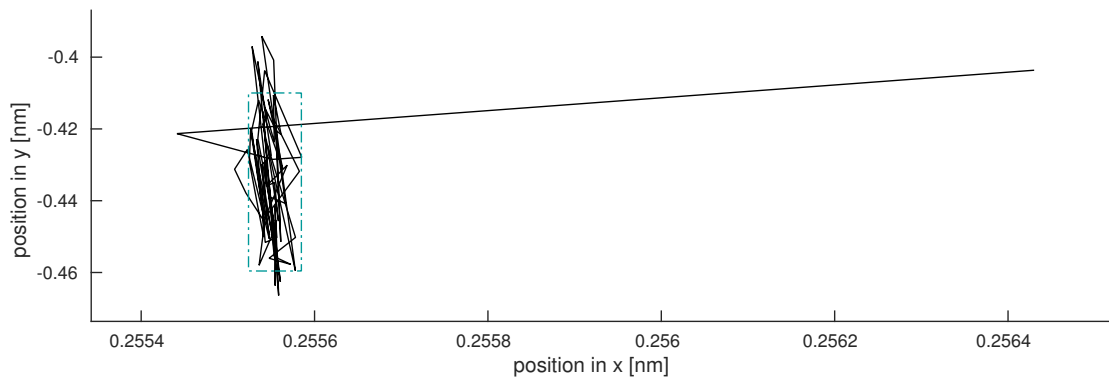


Figure 8.16: Position of point Q over the iterates. The rectangle area contains the position of Q over the last 20 iterates. An enlarged view of this area is shown in figure 8.17.

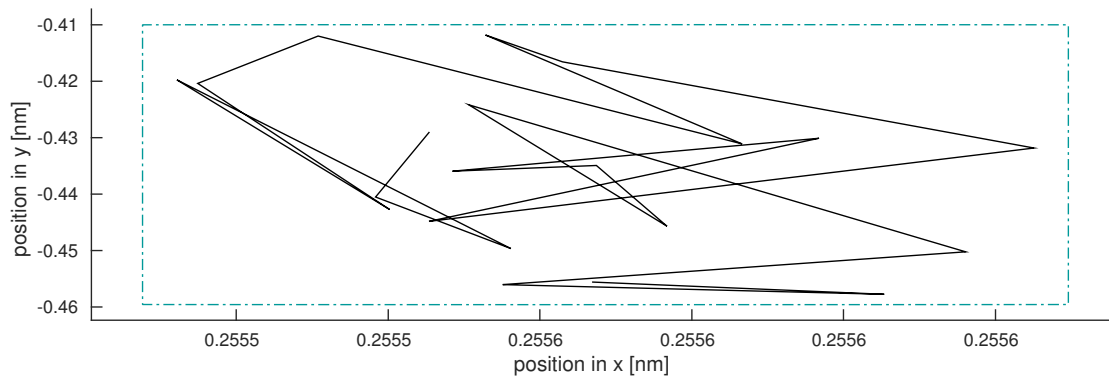


Figure 8.17: Position of point Q over the last 20 iterates.

The search path of point Q is shown in figure 8.16 and 8.17. Again, the behavior is similar to figure 7.2a and the assumptions made in section 7.1 apply.

Stress field

The iterative behavior of the normal stress σ_{rr} of point P is shown in figure 8.18. The result of offline stress averaging is shown in figure 8.19.

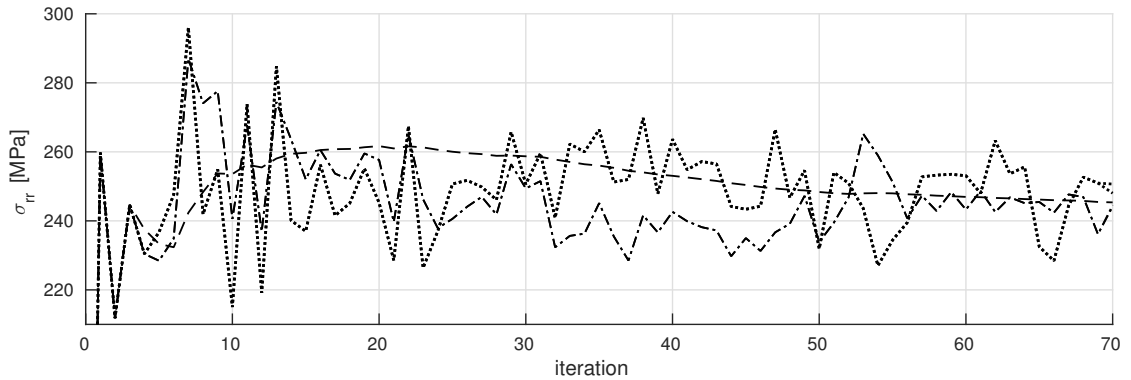


Figure 8.18: Normal stress σ_{rr} at point P over the iterates. The dotted, dashed and dot-dashed lines show the results for *off:u/off:uS*, *on:uSC* and *on:u/on:u;off:S* respectively.

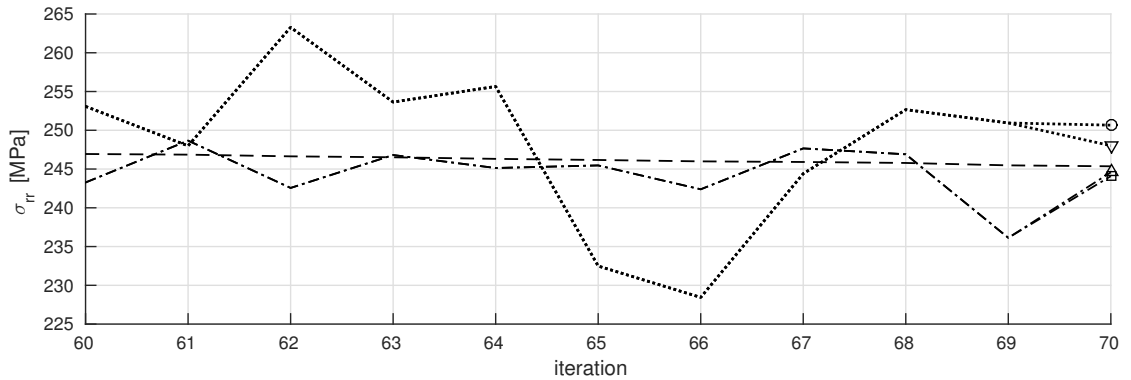


Figure 8.19: Normal stress σ_{rr} at point P over the last 10 iterates. The final stress estimate for the different strategies is marked using the following symbols:

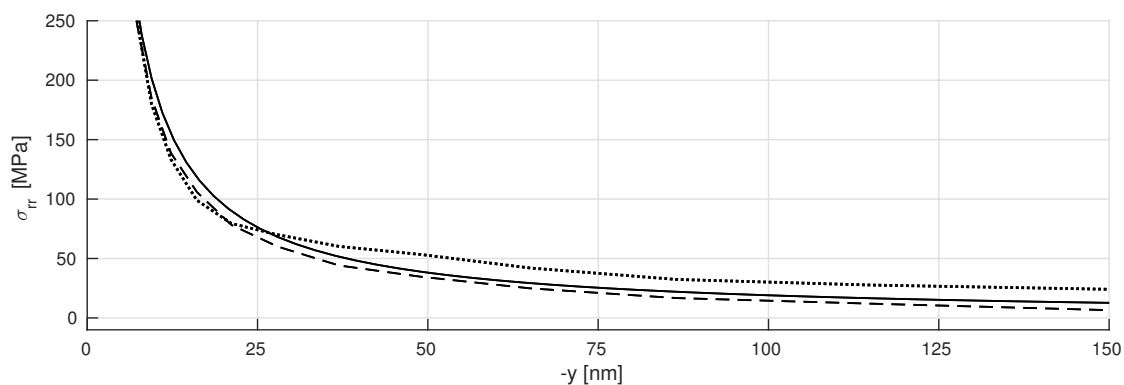
○: *off:u* ▽: *off:uS* □: *on:u* △: *on:u;off:S*.

It seems notable that compared to the first example, using *on:uSC* here results in a much better stress value.

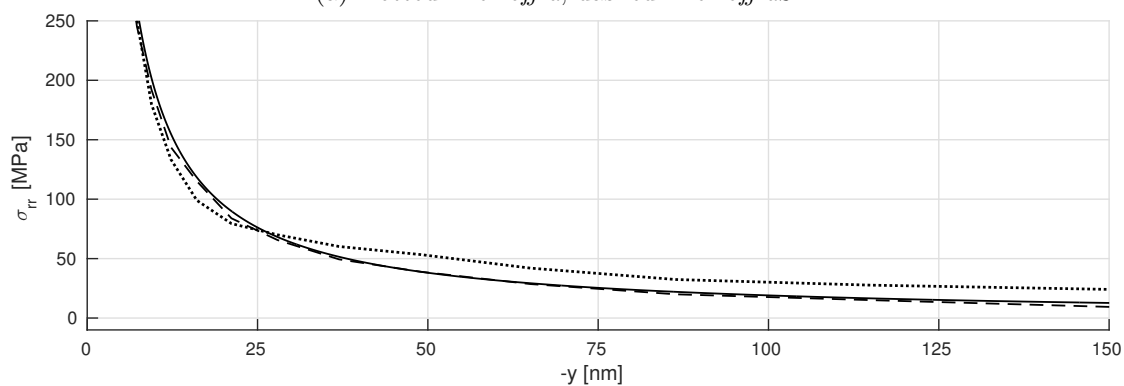
8.2.2 Comparison of the stress distributions

The final estimates of the stress σ_{rr} along the negative y -axis according to the cases 1,2 and 3 presented in table 8.1 are shown in figure 8.20. Similar to the first example, the stress distribution is in good agreement with the analytical solution. While *on:uSC* produced the worst results of all three different strategies in the first example, its resulting stress distribution is superior to the other two strategies in this example.

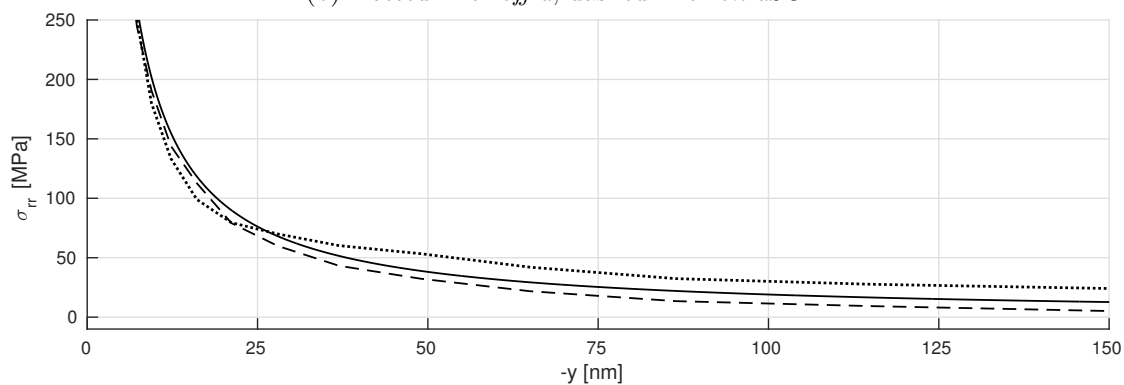
8.2. ELASTIC INFINITE HALF-PLANE UNDER LINE LOAD



(a) Dotted line: *off:u*, dashed line: *off:uS*.



(b) Dotted line: *off:u*, dashed line: *on:uSC*.



(c) Dotted line: *on:u*, dashed line: *on:u;off:S*.

Figure 8.20: Normal stress σ_{yy} along the negative y -axis. The curves in (a),(b) and (c) correspond to the cases 1,2 and 3, presented in table 8.1, respectively. The analytical solution is given according to [Lekhnitskii \(1968\)](#) as a solid line.

Conclusion

The two-scale model used in this work combines continuum mechanics on the macroscale with statistical mechanics on the microscale. In continuum mechanics, no thermal effects are present due to the large size of the described objects. In contrast to this, thermal effects hold a central role in statistical mechanics. Here, macroscopic observables are calculated as averages on the microscale. The averaging procedure can be seen as a measurement process with the macroscopic observables as the corresponding measured value. If the microscale reaches thermodynamic equilibrium, we speak of equilibrium statistical mechanics. The equilibrium ensures that every measurement yields the same measured value \tilde{A} . However, in practical applications, equilibrium on the microscale is not reached due to immense computational cost. This means that measurements yield noise-corrupted values $A = \tilde{A} + \Delta A$ at variance with measured values in equilibrium.

Our main interest is the computation of the displacement field and stress distribution on the macroscale. Here, the displacement field is calculated from the measurements using continuum mechanics. The stress distribution, on the other hand, is directly obtained as a measured value from the microscale. The atomistic model used on the microscale does not reach thermodynamic equilibrium and therefore only gives noise-corrupted stresses $\mathbf{S} = \tilde{\mathbf{S}} + \Delta\mathbf{S}$ and elastic constants $\mathbb{C} = \tilde{\mathbb{C}} + \Delta\mathbb{C}$. The noise originates from the small amounts of atoms in the MD cell and microscopic timesteps. Both constraints are due to reasons of computational efficiency. An approach to diminish the influence of the noise $\Delta\mathbf{S}$ and $\Delta\mathbb{C}$ on the calculations of the macroscale is offline or online averaging (*off:u* or *on:u*). It was shown that both these strategies result in a potentially improved displacement field.

It was mentioned above that the stress distribution, which is our second main focus, is directly obtained as a measured value from the microscale. The macroscopic constraints for this measurement are given by the current displacement field and a constant temperature. Even if an improved displacement field via *off:u* or *on:u* is used to provide the macroscopic constraint, the resulting stress distribution is still subject to substantial deflections. Similar to the approach for the displacement field, this noise may be diminished by offline or online averaging. To prove this, the strategies *off:uS*, *on:uSC* and *on:u;off:S* have been applied to two numerical examples. It was shown that depending on the chosen example, these strategies are capable of improving the stress distribution without introducing additional computational cost.

CONCLUSION

Further work on this subject may address a generalization of the model and study of the convergence behavior and stability criteria. Also plastic or rate-dependent material behavior and the modeling of crystal defects may be included.

List of Figures

2.1	General deformable body in its referential (or material) and its current (or spatial) configuration	9
2.2	Resulting force $\Delta \mathbf{p}$ on an area element Δa	13
2.3	General deformable body in its material and spatial configuration with superposed virtual displacements	14
2.4	General deformable in its spatial configuration (0) and a known deformed configuration (m). The next configuration (m+1) is needed.	17
3.1	Subdivision process of a two-dimensional domain in material configuration.	24
3.2	One-dimensional Lagrange elements	25
3.3	Two-dimensional rectangular Lagrange elements	26
3.4	Two-dimensional triangular Lagrange elements	27
3.5	Indices I, J, K for the cubic triangular Lagrange element.	28
4.1	Mappings between referential (initial) and current (deformed) MD cell with coordinates \mathbf{s}_i and \mathbf{r}_i , respectively.	36
4.2	Periodic boundary conditions applied to a 2-dimensional simulation.	38
5.1	Information exchange between macro- and microscale.	45
5.2	An MD cell is located at each integration point of the macroscopic body.	46
5.3	Macroscopic and microscopic time lines of the described two-scale model. Every Newton-Raphson iteration uses the same amount of microscopic timesteps.	47
5.4	Macroscopic and microscopic time lines of the described two-scale model. The number of microscopic timesteps is chosen to be small in the first iterations and is increased to \mathcal{M} in the final iteration i_{max}	47
7.1	Macroscopic and microscopic time lines of the described two-scale model. The amount of microscopic timesteps per NR iteration is increased gradually.	51
7.2	Two different scenarios of search paths in a two-dimensional SA problem.	53
8.1	Plate with circular notch under uniaxial tension.	57

LIST OF FIGURES

8.2	Modeled system, boundary conditions and FEM mesh.	58
8.3	Displacement of point P over the iterates.	59
8.4	Position of point Q over the iterates.	59
8.5	Position of point Q over the last 20 iterates.	60
8.6	Normal stress σ_{xx} at point P over the iterates.	60
8.7	Normal stress σ_{xx} at point P over the last 10 iterates.	61
8.8	Normalized normal stress σ_{xx} along the y-axis.	62
8.9	Normalized normal stress σ_{yy} along the y-axis.	63
8.10	Normalized normal stress σ_{xx} along the x-axis.	64
8.11	Normalized normal stress σ_{yy} along the x-axis.	65
8.12	Elastic infinite half-plane under line load. Figure and stress definition taken from Lekhnitskii (1968).	66
8.13	Modeled system, boundary conditions and FEM mesh.	66
8.14	Distribution of the normal stress σ_{rr} for the elastic half-plane under line-load.	67
8.15	Displacement of point P over the iterates.	68
8.16	Position of point Q over the iterates.	69
8.17	Position of point Q over the last 20 iterates.	69
8.18	Normal stress σ_{rr} at point P over the iterates.	70
8.19	Normal stress σ_{rr} at point P over the last 10 iterates.	70
8.20	Normal stress σ_{rr} along the negative y-axis.	71
C.1	Sketch of the convergence behavior of the two different functions.	82

List of Tables

4.1	Possible ensembles.	40
4.2	Gear's magic numbers of the 6th-order scheme for integrating second order differential equations.	42
8.1	Compared methods.	56
A.1	EAM coefficients Wadley et al. (2001)	78

Appendix A

EAM functions

The following lines show one possible choice for the functions used in the EAM potential as proposed in [Wadley et al. \(2001\)](#).

$$\rho_i = \sum_{\substack{j=1 \\ j \neq i}}^N \pi_j(r_{ij}) \quad (\text{A.1})$$

$$\pi_j(r_{ij}) = \frac{f_e e^{-\beta\left(\frac{r_{ij}}{r_e}-1\right)}}{1 + \left(\frac{r_{ij}}{r_e} - \lambda\right)^{20}} \quad (\text{A.2})$$

$$\phi_{ij}(r_{ij}) = \frac{A e^{-\alpha\left(\frac{r_{ij}}{r_e}-1\right)}}{1 + \left(\frac{r_{ij}}{r_e} - \kappa\right)^{20}} - \frac{B e^{-\beta\left(\frac{r_{ij}}{r_e}-1\right)}}{1 + \left(\frac{r_{ij}}{r_e} - \lambda\right)^{20}} \quad (\text{A.3})$$

$$F_i(\rho_i) = \sum_{k=0}^3 F_{nk} \left(\frac{\rho_i}{\rho_n} - 1\right)^k, \quad \rho_i < \rho_n, \rho_n = 0.85\rho_e \quad (\text{A.4})$$

$$F_i(\rho_i) = \sum_{k=0}^3 F_k \left(\frac{\rho_i}{\rho_e} - 1\right)^k, \quad \rho_n \leq \rho_i < \rho_0, \rho_0 = 1.15\rho_e \quad (\text{A.5})$$

$$F_i(\rho_i) = F_e \left[1 - \ln\left(\frac{\rho_i}{\rho_e}\right)\right] \left(\frac{\rho_i}{\rho_e}\right)^\eta, \quad \rho_0 \leq \rho_i \quad (\text{A.6})$$

The coefficients contained in these equations are shown in table [A.1](#) for copper and tungsten.

	Cu	W
$r_e(\text{\AA})$	2.556162	2.740840
$f_e(\text{eV}/\text{\AA})$	1.554485	3.487340
$\rho_e(\text{eV}/\text{\AA})$	22.150141	37.234847
α	7.669911	8.900114
β	4.090619	4.746728
$A(\text{eV})$	0.327584	0.882435
$B(\text{eV})$	0.468735	1.394592
κ	0.431307	0.139209
λ	0.86214	0.278417
$F_{n0}(\text{eV})$	-2.176490	-4.946281
$F_{n1}(\text{eV})$	-0.140035	-0.148818
$F_{n2}(\text{eV})$	0.285621	0.365057
$F_{n3}(\text{eV})$	-1.750834	-4.432406
$F_0(\text{eV})$	-2.19	-4.96
$F_1(\text{eV})$	0	0
$F_2(\text{eV})$	0.702991	0.661935
$F_3(\text{eV})$	0.683705	0.348147
η	0.921150	-0.582714
$F_e(\text{eV})$	-2.191675	-4.961306

Table A.1: EAM coefficients [Wadley et al. \(2001\)](#)

Appendix B

Calculation of forces

In the following derivation, indices using latin characters declare specific atoms and are not to be confused with the indicial notation previously used in this thesis. As an example, \mathbf{r}_k is the position vector of atom k . Furthermore, we use $\mathbf{r}_{ij} = \mathbf{r}_i - \mathbf{r}_j$ and $r_{ij} = |\mathbf{r}_{ij}|$.

The force on an atom i can in general be calculated as

$$\mathbf{f}_k = -\frac{\mathcal{V}_{\text{atoms}}}{\partial \mathbf{r}_k}. \quad (\text{B.1})$$

In case of the EAM potential, this yields

$$\begin{aligned} \mathbf{f}_k &= -\frac{\partial}{\partial \mathbf{r}_k} \sum_{i=1}^N \left[F_i(\rho_i) \rho_i + \frac{1}{2} \sum_{\substack{j=1 \\ j \neq i}}^N \phi_{ij}(r_{ij}) \right] \\ &= -\sum_{i=1}^N \left[\frac{\partial F_i(\rho_i)}{\partial \rho_i} \frac{\partial \rho_i}{\partial \mathbf{r}_k} + \frac{1}{2} \sum_{\substack{j=1 \\ j \neq i}}^N \frac{\partial \phi_{ij}(r_{ij})}{\partial \mathbf{r}_k} \right] \\ &= -\sum_{i=1}^N \left[\frac{\partial F_i(\rho_i)}{\partial \rho_i} \sum_{\substack{j=1 \\ j \neq i}}^N \frac{\partial \pi_j(r_{ij})}{\partial \mathbf{r}_k} + \frac{1}{2} \sum_{\substack{j=1 \\ j \neq i}}^N \frac{\partial \phi_{ij}(r_{ij})}{\partial \mathbf{r}_k} \right] \end{aligned} \quad (\text{B.2})$$

Remark. To calculate the derivatives in equation B.2 we can make use of the chain rule in the form

$$\frac{\partial A(r_{ij})}{\partial \mathbf{r}_k} = \frac{\partial A(r_{ij})}{\partial r_{ij}} \frac{\partial r_{ij}}{\partial \mathbf{r}_k}. \quad (\text{B.3})$$

Calculation of the first term is straightforward.

The second term gives

$$r_{kj} = |\mathbf{r}_{kj}| = \sqrt{\mathbf{r}_{kj}^T \mathbf{r}_{kj}} = (\mathbf{r}_{kj}^T \mathbf{r}_{kj})^{\frac{1}{2}} \quad (\text{B.4})$$

$$\frac{\partial r_{ij}}{\partial \mathbf{r}_{ij}} = \frac{\partial (\mathbf{r}_{ij}^T \mathbf{r}_{ij})^{\frac{1}{2}}}{\partial \mathbf{r}_{ij}} \quad (\text{B.5})$$

Using indicial notation, this is

$$\begin{aligned} \frac{\partial r_{ij}}{\partial r_{\beta}^{ij}} &= \frac{\partial (r_{\alpha}^{ij} r_{\alpha}^{ij})^{\frac{1}{2}}}{\partial r_{\beta}^{ij}} \\ &= \frac{1}{2} (r_{\alpha}^{ij} r_{\alpha}^{ij})^{-\frac{1}{2}} \underbrace{[\delta_{\alpha\beta} r_{\alpha}^{ij}]}_{r_{\beta}^{ij}} + \underbrace{r_{\alpha}^{ij} \delta_{\alpha\beta}}_{r_{\beta}^{ij}} \\ &= \frac{1}{2} \frac{1}{(r_{\alpha}^{ij} r_{\alpha}^{ij})^{\frac{1}{2}}} 2r_{\beta}^{ij}. \end{aligned} \quad (\text{B.6})$$

Returning to conventional notation yields

$$\frac{\partial r_{ij}}{\partial \mathbf{r}_{ij}} = \frac{\mathbf{r}_{ij}}{r_{ij}}. \quad (\text{B.7})$$

Using the results given in the remark above, equation B.2 can be written as

$$\begin{aligned} \mathbf{f}_k &= \sum_{\substack{i=1 \\ i \neq k}}^N \left[\frac{\partial F_i(\rho_i)}{\partial \rho_i} \frac{\partial \pi_k(r_{ik})}{\partial r_{ik}} + \frac{1}{2} \frac{\partial \phi_{ik}(r_{ik})}{\partial r_{ik}} \right] \frac{\mathbf{r}_{ik}}{r_{ik}} \\ &\quad - \sum_{\substack{j=1 \\ j \neq k}}^N \left[\frac{\partial F_k(\rho_k)}{\partial \rho_k} \frac{\partial \pi_j(r_{kj})}{\partial r_{kj}} + \frac{1}{2} \frac{\partial \phi_{kj}(r_{kj})}{\partial r_{kj}} \right] \frac{\mathbf{r}_{kj}}{r_{kj}} \end{aligned}$$

where $\frac{\partial \mathbf{r}_{ik}}{\partial \mathbf{r}_k} = -\mathbf{1}$ and $\frac{\partial \mathbf{r}_{kj}}{\partial \mathbf{r}_k} = \mathbf{1}$ was used. Also $\frac{\partial \mathbf{r}_{ij}}{\partial \mathbf{r}_k} = \mathbf{0}$ for $i \neq k$, $j \neq k$.¹

Using $\mathbf{r}_{ik} = -\mathbf{r}_{kj}$ and $\phi_{ik}(r_{ik}) = \phi_{kj}(r_{kj})$ for $j = i$ finally gives

$$\mathbf{f}_k = - \sum_{\substack{j=1 \\ j \neq k}}^N \left[\frac{\partial F_j(\rho_j)}{\partial \rho_j} \frac{\partial \pi_k(r_{jk})}{\partial r_{jk}} + \frac{\partial F_k(\rho_k)}{\partial \rho_k} \frac{\partial \pi_j(r_{kj})}{\partial r_{kj}} + \frac{\partial \phi_{kj}(r_{kj})}{\partial r_{kj}} \right] \frac{\mathbf{r}_{kj}}{r_{kj}} \quad (\text{B.8})$$

If we substitute k with i , this result can be rewritten in a more common notation as

$$\mathbf{f}_i = - \sum_{\substack{j=1 \\ j \neq i}}^N \left[\frac{\partial F_j(\rho_j)}{\partial \rho_j} \frac{\partial \pi_i(r_{ji})}{\partial r_{ji}} + \frac{\partial F_i(\rho_i)}{\partial \rho_i} \frac{\partial \pi_j(r_{ij})}{\partial r_{ij}} + \frac{\partial \phi_{ij}(r_{ij})}{\partial r_{ij}} \right] \frac{\mathbf{r}_{ij}}{r_{ij}}. \quad (\text{B.9})$$

¹ $\mathbf{1}$ is the $[3 \times 3]$ identity matrix and $\mathbf{0}$ is a $[3 \times 3]$ null matrix.

APPENDIX B. CALCULATION OF FORCES

We can also write this as

$$\mathbf{f}_i = - \sum_{\substack{j=1 \\ j \neq i}}^N \chi_{ij}(r_{ij}) \frac{\mathbf{r}_{ij}}{r_{ij}}, \quad (\text{B.10})$$

where the abbreviation

$$\chi_{ij}(r_{ij}) = \frac{\partial F_j(\rho_j)}{\partial \rho_j} \frac{\partial \pi_i(r_{ji})}{\partial r_{ji}} + \frac{\partial F_i(\rho_i)}{\partial \rho_i} \frac{\partial \pi_j(r_{ij})}{\partial r_{ij}} + \frac{\partial \phi_{ij}(r_{ij})}{\partial r_{ij}} \quad (\text{B.11})$$

is used in section 4.3 to write the equations of motion in a more compact way.

The required derivatives of the functions given in appendix A are

$$\begin{aligned} \frac{\partial \phi_{ij}(r_{ij})}{\partial r_{ij}} &= A e^{-\alpha(\frac{r_{ij}}{r_e}-1)} \left(-\frac{\alpha}{r_e} \right) \left[1 + \left(\frac{r_{ij}}{r_e} - \kappa \right)^{20} \right]^{-1} \\ &\quad - A e^{-\alpha(\frac{r_{ij}}{r_e}-1)} \left[1 + \left(\frac{r_{ij}}{r_e} - \kappa \right)^{20} \right]^{-2} 20 \left(\frac{r_{ij}}{r_e} - \kappa \right)^{19} \frac{1}{r_e} \\ &\quad - B e^{-\beta(\frac{r_{ij}}{r_e}-1)} \left(-\frac{\beta}{r_e} \right) \left[1 + \left(\frac{r_{ij}}{r_e} - \lambda \right)^{20} \right]^{-1} \\ &\quad - B e^{-\beta(\frac{r_{ij}}{r_e}-1)} \left[1 + \left(\frac{r_{ij}}{r_e} - \lambda \right)^{20} \right]^{-2} 20 \left(\frac{r_{ij}}{r_e} - \lambda \right)^{19} \frac{1}{r_e} \end{aligned}$$

$\rho < \rho_n, \rho_n = 0.85\rho_e$:

$$\frac{\partial F_i(\rho_i)}{\partial \rho_i} = \sum_{k=0}^3 F_{nk} k \left(\frac{\rho_i}{\rho_n} - 1 \right)^{k-1} \frac{1}{\rho_n} \quad (\text{B.12})$$

$\rho_n \leq \rho < \rho_0, \rho_0 = 1.15\rho_e$:

$$\frac{\partial F_i(\rho_i)}{\partial \rho_i} = \sum_{k=0}^3 F_k k \left(\frac{\rho_i}{\rho_e} - 1 \right)^{k-1} \frac{1}{\rho_e} \quad (\text{B.13})$$

$\rho_0 \leq \rho$:

$$\frac{\partial F_i(\rho_i)}{\partial \rho_i} = -F_e \frac{\eta}{\rho_i} \left(\frac{\rho_i}{\rho_e} \right)^\eta + F_e \left[1 - \ln \left(\frac{\rho_i}{\rho_e} \right)^\eta \right] \eta \left(\frac{\rho_i}{\rho_e} \right)^{\eta-1} \frac{1}{\rho_e} \quad (\text{B.14})$$

$$\begin{aligned} \frac{\partial \pi_j}{\partial r_{ij}} &= f_e e^{-\beta(\frac{r_{ij}}{r_e}-1)} \left(-\frac{\beta}{r_e} \right) \left[1 + \left(\frac{r_{ij}}{r_e} - \lambda \right)^{20} \right]^{-1} \\ &\quad - f_e e^{-\beta(\frac{r_{ij}}{r_e}-1)} \left[1 + \left(\frac{r_{ij}}{r_e} - \lambda \right)^{20} \right]^{-2} 20 \left(\frac{r_{ij}}{r_e} - \lambda \right)^{19} \frac{1}{r_e}. \end{aligned} \quad (\text{B.15})$$

Appendix C

Comparison of the convergence behavior towards zero

In chapter 7, we introduced a factor A in the form

$$\mathcal{M}_i = \frac{a+i}{a}A. \quad (\text{C.1})$$

that allows us to adjust the amount of microsteps \mathcal{M}_i per Newton-Raphson iteration. In section 6.1, we stated that offline averaging only yields proper results if the chosen sequence $f(n) = \varepsilon_n = \frac{1}{\mathcal{M}_n}$ shows slower convergence towards zero than $g(n) = \frac{1}{n}$. Now, we want to prove that this is indeed the case for the chosen sequence. Both functions are sketched in figure C.1.

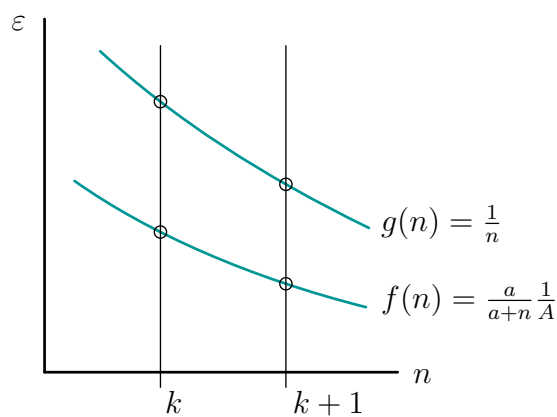


Figure C.1: Sketch of the convergence behavior of the two different functions.

The function $f(n)$ goes definitely slower to zero than $g(n)$ if the following statement is true for any value of k

$$\frac{f(k+1)}{f(k)} > \frac{g(k+1)}{g(k)}. \quad (\text{C.2})$$

APPENDIX C. COMPARISON OF THE CONVERGENCE BEHAVIOR
TOWARDS ZERO

Inserting the function values gives

$$\begin{aligned} \frac{\frac{a}{a+k+1} \frac{1}{A}}{\frac{a}{a+k} \frac{1}{A}} &> \frac{\frac{1}{k+1}}{\frac{1}{k}} \\ \frac{a+k}{a+k+1} &> \frac{k}{k+1} \\ ak + a + k^2 + k &> ak + k^2 + k \\ a &> 1. \end{aligned} \tag{C.3}$$

Bibliography

- Allen, M.P., Tildesley, T.J., 2009. Computer simulation of liquids. (Oxford: Clarendon Press).
- Andersen, H.C., 1980. Molecular dynamics simulations at constant pressure and/or temperature. *J. Chem. Phys.* 72, 2384–2393.
- Bathe, K.J., 1996. Finite Element Procedures. (New Jersey: Prentice-Hall, Inc.).
- Benaïm, M., 1993. The “off line learning approximation” in continuous time neural networks: An adiabatic theorem. *Neural Networks* , 655–665.
- Bonet, J., Wood, R.D., 1997. Nonlinear continuum mechanics for finite element analysis. Cambridge: Cambridge University Press.
- Çağın, T., Pettitt, B.M., 1989. Elastic constants of nickel: Variations with respect to temperature and pressure. *Phys. Rev. B* 39, 12484–12491.
- Cheng, B., Titterton, D.M., 1994. Neural networks: A review from a statistical perspective. *Statist. Sci.* 9, 2–30.
- Daw, M.S., Baskes, M.I., 1984. Embedded-atom method: Derivation and application to impurities, surfaces, and other defects in metals. *Phys. Rev. B* 29, 6443–6453.
- Daxner, T., Rammerstorfer, F.G., 2011. Nichtlineare Finite Elemente Methoden; Vorlesungsskript.
- E, W., Engquist, B., Li, X., Ren, W., Vanden-Eijnden, E., 2007. Heterogeneous multiscale methods: A review. *Commun. Comput. Phys.* 2, 367–450.
- El Alem, W., El Hami, A., Ellaia, R., 2011. A new methodology for an optimal shape design. *Applied Mechanics and Materials* 61, 43–54.
- Featherston, F.H., Neighbours, J.R., 1963. Elastic constants of tantalum, tungsten, and molybdenum. *Phys. Rev.* 130, 1324–1333.
- Gear, C.W., 1966. The Numerical Integration of Ordinary Differential Equations of Various Orders. (Argonne National Laboratory).

BIBLIOGRAPHY

- Gear, C.W., 1971. Numerical initial value problems in ordinary differential equations. (Prentice-Hall).
- Goldstein, H., Poole, C., Safko, J., 2002. Classical Mechanics. Addison Wesley.
- Hoover, W.G., 1985. Canonical dynamics: Equilibrium phase-space distributions. *Phys. Rev. A* 31, 1695–1697.
- Hünenberger, P.H., 2005. Thermostat algorithms for molecular dynamics simulations. *Adv. Polym. Sci.* 173, 105–149.
- Kiefer, J., Wolfowitz, J., 1952. Stochastic estimation of the maximum of a regression function. *Ann. Math. Statist.* 23, 462–466.
- Kushner, H.J., Yang, J., 1993. Stochastic approximation with averaging of the iterates: Optimal asymptotic rate of convergence for general processes. *SIAM J. Control Optim.* , 1045–1062.
- Kushner, H.J., Yin, G.G., 2003. Stochastic Approximation and Recursive Algorithms and Applications. (Springer).
- Lazarus, D., 1949. The variation of the adiabatic elastic constants of KCl, NaCl, CuZn, Cu, and Al with pressure to 10,000 bars. *Phys. Rev.* 76, 545–53.
- Lekhnitskii, S., 1968. Anisotropic Plates. (Gordon & Breach).
- López-Rubio, E., Luque-Baena, R.M., 2011. Stochastic approximation for background modelling. *Computer Vision and Image Understanding* 115, 735–749.
- Marsden, J.E., Hughes, T.J.R., 1983. Mathematical foundations of elasticity. (Prentice-Hall).
- Nosé, S., 1984. A unified formulation of the constant temperature molecular-dynamics methods. *J. Chem. Phys.* 81, 511–519.
- Parrinello, M., Rahman, A., 1981. Polymorphic transitions in single crystals: A new molecular dynamics method. *J. Appl. Phys.* 52, 7182–7190.
- Podio-Guidugli, P., 2010. On (Andersen-)Parrinello-Rahman molecular dynamics, the related metadynamics, and the use of the Cauchy-Born rule. *J. Elasticity* 100, 145–153.
- Polyak, B.T., Juditsky, A.B., 1992. Acceleration of stochastic approximation by averaging. *SIAM J. Control Optim.* , 838–855.
- Ray, J.R., Rahman, A., 1985. Statistical ensembles and molecular dynamics studies of anisotropic solids. II. *J. Chem. Phys.* 82, 4243–4247.
- Robbins, H., Monro, S., 1951. A stochastic approximation method. *Ann. Math. Statist.* 22, 400–407.

- Seyedpoor, S.M., Salajegheh, J., Salajegheh, E., Gholizadeh, S., 2011. Optimal design of arch dams subjected to earthquake loading by a combination of simultaneous perturbation stochastic approximation and particle swarm algorithms. *Applied Soft Computing* 11, 39–48.
- Sokolnikoff, I.S., 1964. *Tensor Analysis: Theory and Applications to Geometry and Mechanics of Continua*. (John Wiley & Sons, Inc).
- Spall, J.C., 2003. *Introduction to Stochastic Search and Optimization: Estimation, Simulation, and Control*. (Wiley).
- Sultan, C., 2010. Proportional damping approximation using the energy gain and simultaneous perturbation stochastic approximation. *Mechanical Systems and Signal Processing* 24, 2210–2224.
- Tadmor, E.B., Miller, R.E., 2011. *Modeling Materials: Continuum, atomistic and multiscale techniques*. Cambridge: Cambridge University Press.
- Ulz, M.H., 2013. Comments on a continuum-related Parrinello-Rahman molecular dynamics formulation. *J. Elasticity* 113, 93–112.
- Ulz, M.H., 2015. Coupling the finite element method and molecular dynamics in the framework of the heterogeneous multiscale method for quasi-static isothermal problems. *Journal of the Mechanics and Physics of Solids* 74, 1 – 18.
- Wadley, H.N.G., Zhou, X., Johnson, R.A., Neurock, M., 2001. Mechanisms, models and methods of vapor deposition. *Progress in Materials Science* 46, 329–377.
- Weiner, J.H., 2002. *Statistical mechanics of elasticity*. 2nd ed., New York: Dover Publications, Inc.
- Wen-Long, C., Yong-Hua, H., Liu, N., Ma, R., 2012. Estimation of geological formation thermal conductivity by using stochastic approximation method based on well-log temperature data. *Energy* 38, 21–30.
- Wriggers, P., 2008. *Nonlinear Finite Element Methods*. (Springer).
- Wurm, P., 2013. Determining the elasticity components of a metal single crystal using molecular dynamics. Bachelor Thesis.
- Zienkiewicz, O.C., Taylor, R.L., 2000. *The Finite Element Method*. (Butterworth Heimemann).